NSF/CEE-81085

Research Report R81-6 Order No. 693

MIT

A GEOPHYSICAL MODEL OF STRONG MOTION FOR LARGE ENSEMBLE GENERATION

by

Jean B. Savy

DEPARTMENT
OF
CIVIL
ENGINEERING

SCHOOL OF ENGINEERING
MASSACHUSETTS INSTITUTE OF TECHNOLOGY
Cambridge, Massachusetts 02139

July 1981

Sponsored by
The National Science Foundation
Grant No. PFR-7827068

Additional Copies May be Obtained From:

National Technical Information Service
U.S. Department of Commerce
5285 Port Royal Road
Springfield, Virginia 22161

50272-101

REPORT DOCUMENTATION PAGE	1. REPORT NO. NSF/CEE-81085	2.	3. Recipient's Accession No. PB82 172628
4. Title and Subtitle: Geophysical Model of Strong Motion for Large Ensemble Generation			5. Report Date: July 1981 6. 063212
7. Author(s): J.B. Savy			8. Performing Organization Rept. No. R81-6
9. Performing Organization Name and Address: Massachusetts Institute of Technology Department of Civil Engineering Cambridge, MA 02139			10. Project/Task/Work Unit No. 11. Contract(C) or Grant(G) No. (C) (G) PFR7827068
12. Sponsoring Organization Name and Address: Directorate for Engineering (ENG) National Science Foundation 1800 G Street, N.W. Washington, DC 20550			13. Type of Report & Period Covered 14.

15. Supplementary Notes
Submitted by: Communications Program (OPRM)
National Science Foundation
Washington, DC 20550

16. Abstract (Limit: 200 words)

A model of fault rupture is developed for use in qualitative studies of seismic hazard analyses. The total rupture area is modeled by an assemblage of rectangular patches with random size and aspect ratio. The propagation of the rupture front is simulated by a random process similar to a directed random walk process. The solution for the motion generated by a single patch is obtained by using the Haskell method of dislocation extended to a dislocation both in the length and width of the patch. To obtain a better approximation of the motion in the near to intermediate field, second order terms are added to the solution. Some examples dramatize the effects of fault orientation, focus location, stress drop, and overall geometry on the final peak acceleration and RMS acceleration at the observation point. A sensitivity analysis, and an enumeration of ongoing research and projected studies using the model are presented.

17. Document Analysis a. Descriptors

Earthquakes
Mathematical models
Monte Carlo method
Hazards
Simulation
Fourier transformation

b. Identifiers/Open-Ended Terms

Ground motion
Earthquake simulation
C.A. Cornell, /PI

c. COSATI Field/Group

18. Availability Statement	19. Security Class (This Report)	21. No. of Pages
NTIS	20. Security Class (This Page)	22. Price

(See ANSI-Z39.18) See Instructions on Reverse OPTIONAL FORM 272 (4-77)
(Formerly NTIS-35)
Department of Commerce

A

Research Report R81-6 Order No. 693

Department of Civil Engineering

Massachusetts Institute of Technology

A GEOPHYSICAL MODEL OF STRONG MOTION FOR LARGE ENSEMBLE GENERATION

by

Jean B. Savy

Sponsored by

The National Science Foundation

Grant No. PFR-7827068

July 1981

ACKNOWLEDGEMENTS

The research leading to this report was sponsored by the National Science Foundation under Grant No. PFR-7827068, entitled, "Engineering Ground Motion Prediction Procedures," and was performed under the supervision of Professor C. Allin Cornell. The author thanks Professors Keiiti Aki, Michel Bouchon and Bernard Chouet of the Department of Geophysics at M.I.T., and David Boore of USGS for their help in useful discussions. A special thanks also to Apostolos Papageorgiou for checking parts of the equations developed here.

TABLE OF CONTENTS

I. INTRODUCTION

Recognizing the necessity of being able to reproduce earthquake ground motion with accuracy, a number of seismologists have developed mathematical models, some rather simple and some more complex (see Brune, 1970 and Bouchon, 1977, for example).

Although some engineering needs could be adequately satisfied by such models, it gradually became evident that a large number of engineering problems could not.

Because the effect of earthquakes on engineering realizations (structures) is predominant at short to intermediate distances from a seismic source (0 to approximately 100km) it became necessary to study the effect of the following parameters on the motion recorded at a given site:

- distance from the fault, (distance from the epicenter, hypocenter, shortest distance, etc.)
- location of the site relative to the fault,
- spatial orientation of the fault,
- dimension and shape of the fault,
- size of the event (amount of energy released),
- dynamic characteristics of the source, such as:
  - location of focus,
  - type of rupture (dislocation, slip vs. dip, and unilateral vs. bilateral)
  - rupture propagation process,
  - velocity of propagation,
  - property of the dislocation (dislocation function)

— other properties, such as the attenuation of the waves with distance, or the mechanical characteristics of the medium through which the waves propagate.

In 1978, we presented a model which was devised to handle such a study by introducing a model of the source compatible with our understanding of the physical process. This model was based on the fact that an earthquake is made of a superposition of effects due to the progressive rupture of small portions of the total rupture area, irregular in shape and size. This physical phenomenon is evidenced in a study of the rupture process of the Parkfield, 1966, earthquake (Aki, 1979).

An analytical solution based on the work of Boatwright & Boore (1975) was developed for the S-H far-field component of the motion. Although this solution was adequate for the type of problems analyzed (seismic risk analysis) it appeared necessary to modify and improve it for the purpose of performing the above mentioned studies.

This paper, therefore, presents in detail a model of generation of the strong motion part of earthquake ground motions, valid in the close to intermediate field and for any body wave component (P and S, horizontal and vertical). Although its algebraic formulation is slightly more complex than the previous model, its basic structure remains simple. The cost of computing acceleration records is still low and permits the creation of ensembles of records for statistical studies.

In the last chapter of this paper, a brief sensitivity analysis and an enumeration of ongoing research and projected studies using the model are presented. A detailed presentation of these results will be the object of a follow-up paper.

II. FAULT RUPTURE MODEL

2.1 Introduction

For a long time it has been known that shallow earthquake energy is not released by a sudden instantaneous rupture of a part of the earth's crust. Rather, is is a crack-like phenomenon, the tip of which propagates from an initial localized region, called the focus at a finite velocity in one and sometimes several directions. Haskell (1966) showed that some of the complexity in the rupture process could be accounted for by modeling it with a stochastic process with a spatio-temporal autocorrelation, thus introducing the idea of coherence in the rupture lenth. Later, Boore and Joyner (1978) using a simplified Haskell model showed the importance of incoherence, or irregularities, in the rupture process on the frequency content of the motion and its influence on directivity.

In actuality it is only necessary to observe fault traces to be convinced of the erratic manner in which a rupture propagates. The big 1857 Fort Tejon earthquake, for instance, is believed to have been the result of the progressive rupture of many strands of fault where the relative displacement went from zero to as much as 11m at some points (Seih, 1978). Aki (1979) showed how the map of the aftershocks of the Parkfield earthquake could be interpreted as a map of the main shock rupture area putting in evidence the erratic spatial characteristics of the rupture. Also, using data from deep mines, McGarr & Al (1979) showed how micro earthquakes presented the same characteristics of irregularities in the rupture process.

Some authors have tried to account for those irregularities in a purely statistical manner, such as Haskell, or Boore & Joyner, as mentioned above,

or such as Andrews (1980), who considers a random field of strength, stresses and stress build-up across the rupture fault. Others, such as Das & Aki, had a more physical approach by assuming the rupture surface to be made of regions of low strengths separated by regions of high strengths called barriers. Depending on the strength of the earthquake, the rupture can propagate through one of the low strength regions and stop or break one or several barriers.

2.2 Geometry of the Model Source

We assume here that the spatial irregularities can be represented by considering the fault rupture to be made of an assemblage of smaller areas which we call patches (see Fig. 2.1). These patches are random in shape and size, so that it is necessary to define them by their statistical characteristics. The shape is represented here by rectangles whose ratio of width to length is assumed to have a constant average value, generally close to 1/2 as shown by Geller (1976).

The case of the size is a somewhat more difficult problem since it is believed that irregularities exist at all scales, Andrews (1980). It is therefore necessary to chose a typical length (the coherence length) for the patches, consistent with actual earthquakes and with the analytical model, (derived in the next chapter). The scale chosen here is a macro scale, that is, of the order of length of the fault. It is consistent with the scale chosen by others such as Aki (1980), Baecher (1980), and others, and also Papageorgiou (1980) who backfigured the coherence length from actual recordings for the frequency range of engineering interest (1 to 10 Hz).

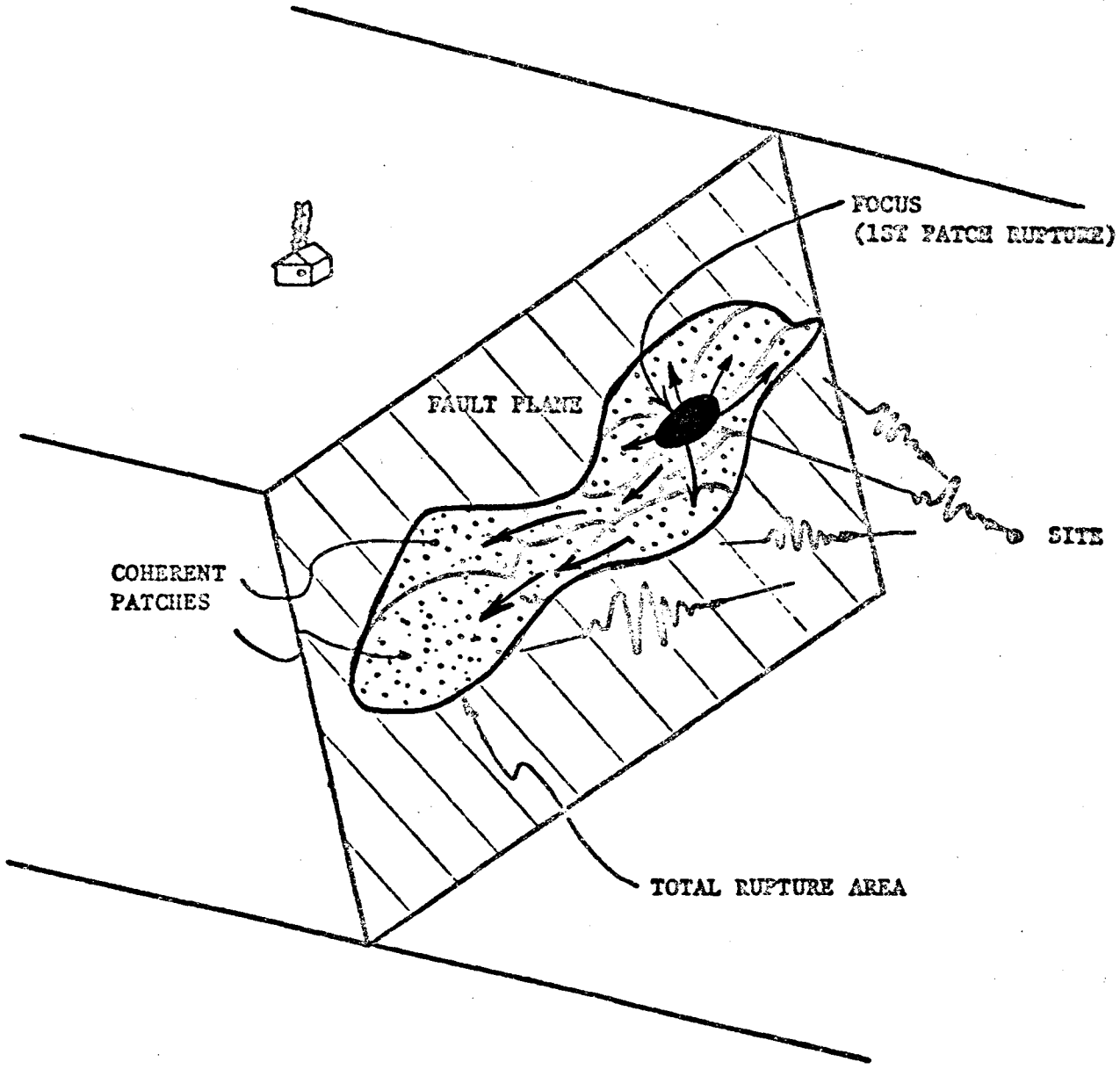

Figure 2.1 THE TOTAL RUPTURE AREA IS REPRESENTED BY AN ASSEMBLAGE OF COHERENT PATCHES. THE TRIGGERING TIME OF EACH COHERENT PATCH IS DETERMINED BY PROPAGATING THE RUPTURE FROM THE INITIAL RUPTURE PATCH (FOCUS). THE EARTHQUAKE IS GENERATED AS THE DISLOCATION OF ALL THE COHERENT PATCHES IS COMPLETED.

2.3 Modeling of the Fault Rupture Using Simulation

In the model described above, the earthquake source is entirely known when the dimensions and orientation in space of the total rupture area, as well as its actual discretization in smaller patches, and their times of rupture initiation are defined.

The orientation of the fault plane is defined by the angle of strike and angle of dip, and the direction of rupture within this plane is defined by what is often called the angle of rake. Once the rupture area has been defined, we use a Monte Carlo simulation technique to generate the assemblage of patches.

In a first step, the fault is cut in strips of length whose probability density function $f_{L'}(\ell)$ is set in advance (see Fig. 2.2a). Any probability distribution consistent with the physics of the process could be chosen here. Boore & Joyner (1978) in their linear model of fault rupture opted for a negative exponential distribution of the patches length (L'), so did Savy (1978) in a two-dimensional extension of the former model. We now use a somewhat different probability density function which converges towards the negative exponential function for ruptures with large number of patches. This point which is developed in detail in Chapter V of this report leads to the following marginal distribution:

$$f_{L'}(\ell) = \frac{(n_L - 1)}{L} \left(1 - \frac{\ell}{L}\right)^{n_L - 2} \quad , \; 0 \leq \ell \leq L \qquad (2.1)$$

where L is the total length of the fault and n_L is the number of strips.

Each strip i of length ℓ_i and width W is then discretized in n_W patches of length ℓ_i and width w_j also using a Monte Carlo simulation (see Fig. 2.2(b)). The marginal probability density function for the patches' width is of the

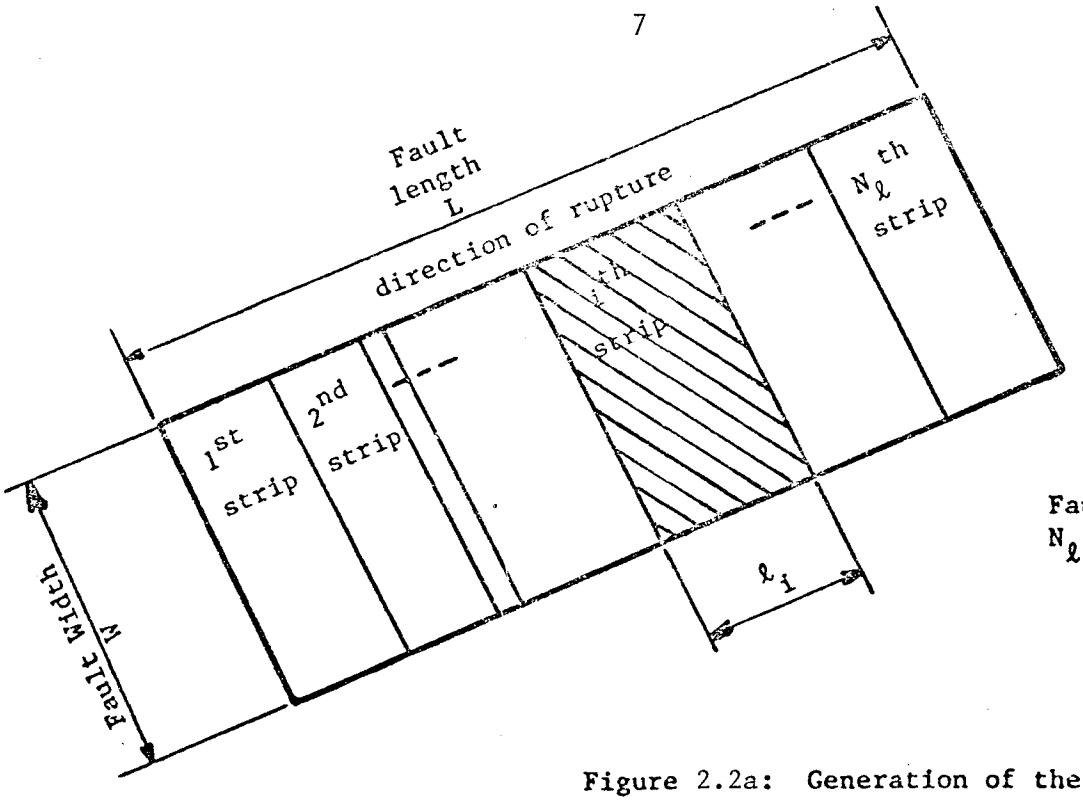

Figure 2.2a: Generation of the fault's strips.

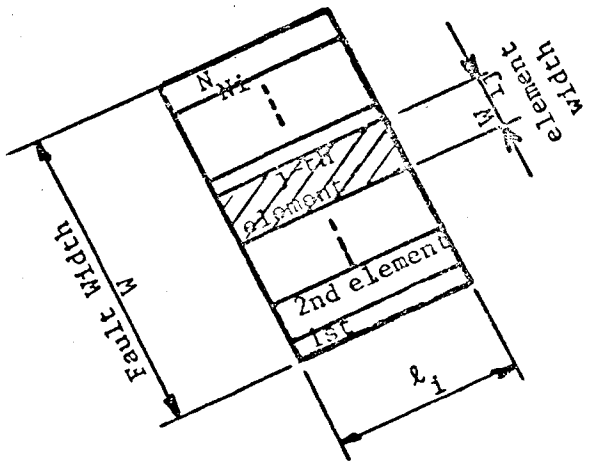

Figure 2.2b: Generation of the coherent patch elements in the i-th strip.

Figure 2.2. Generation of the coherent patches by simulation.

same form as for the strips, i.e.:

$$f_{W'}(w) = \frac{(n_W-1)}{W}\left(1 - \frac{w}{W}\right)^{n_W-2}, \quad 0 \leq w \leq W \tag{2.2}$$

Given the nature of the distribution function, it is interesting to note that the segments lengths are obtained by generating (in the case of the strips for instance) a set of (n_L-1) segments S_j uniformly distributed on [0-L]. Those segments are then ranked in ascending order say $S_1 \leq S_2 \leq S_3 \ldots < S_{n_L-1}$, and the strips length is obtained by taking the difference between two consecutive S's.

$$\begin{cases} \ell_1 = S_1 \\ \ell_i = S_i - S_{i-1} \quad \text{for } i = 2 \text{ to } n_L-1 \\ \ell_{n_L} = L - S_{n_L-1} \end{cases} \tag{2.3}$$

In order to determine the triggering time of each patch, it is assumed that the rupture front, initiated from the focus, travels at an irregular speed from patch to patch. A patch is said to be triggered when the rupture front reaches it. The irregularity of the rupture velocity is accounted for by considering it as a random variable, and a Monte-Carlo technique is used to assign one value of velocity to each patch. A uniform probability density is arbitrarily chosen here, but the mean of the rupture velocity is constrained to be .72 times the shear wave velocity β, and the maximum value is 1.1β (Geller, 1976).

The triggering time, T_g, for any given patch is then computed using a minimum path technique. That is, of all possible paths for the rupture

front to arrive from the focus to the given patch, the one which takes the shortest time is the minimum path. This shortest time is then the triggering time, T_g, for this given patch. The Fig. 2.3 shows how the rupture propagates, and Fig. 2.4 shows an actual simulation where isochron curves are plotted showing the progression of the rupture front in time.

Each patch can be triggered by any one of the surrounding patches, thus the analytical solution developed in Chapter III has to accomodate this fact. In Chapter III, the motion created at a site by the rupture of a single patch is derived assuming a ramp function for the relative displacement of both sides of the fault thus completing the description of the source mechanism.

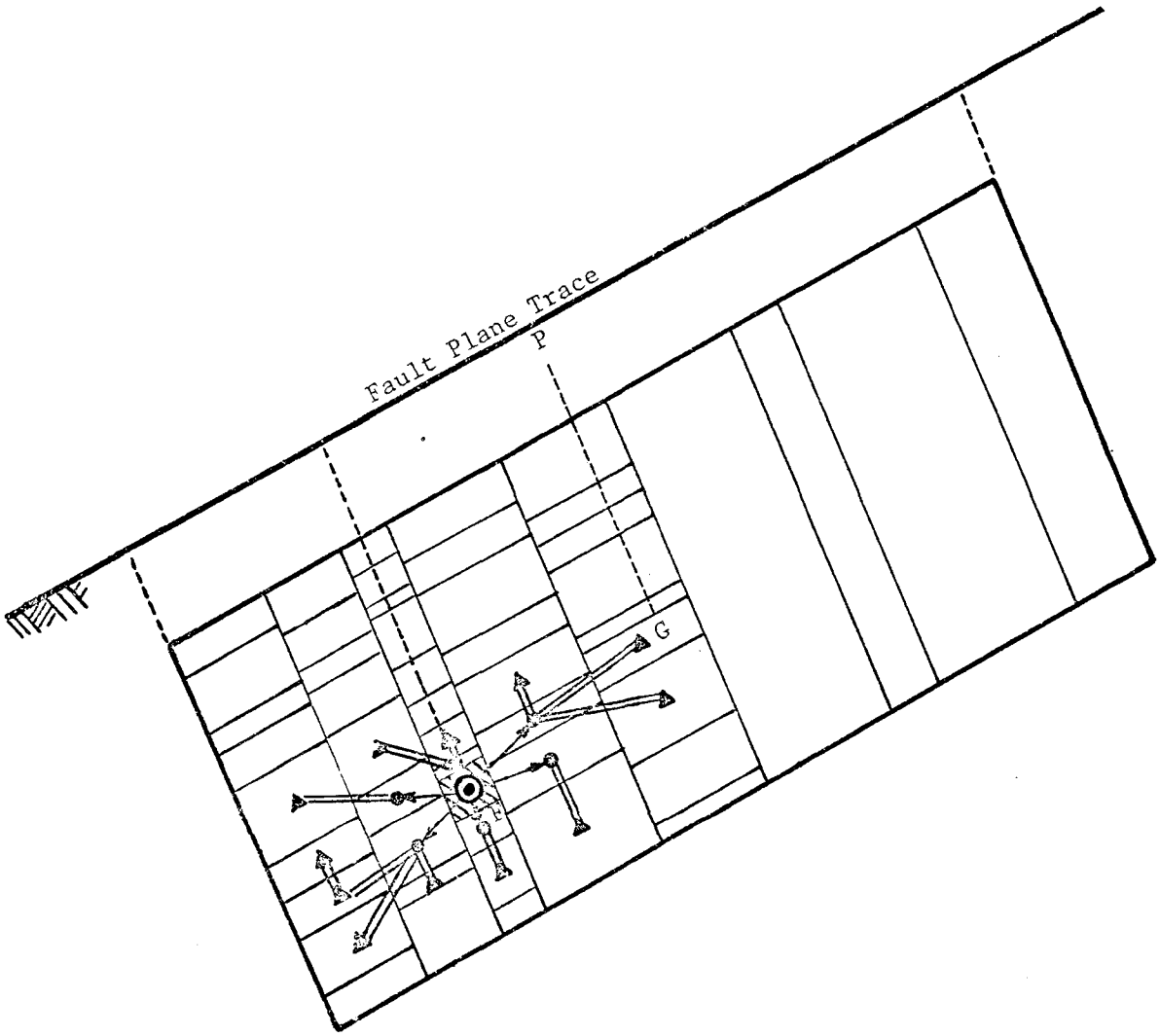

Figure 2.3 Simulation of the progressive rupture of the fault. The rupture initiates at F and is propagated to neighboring patches, which in turn propagate it to their adjacent patches.

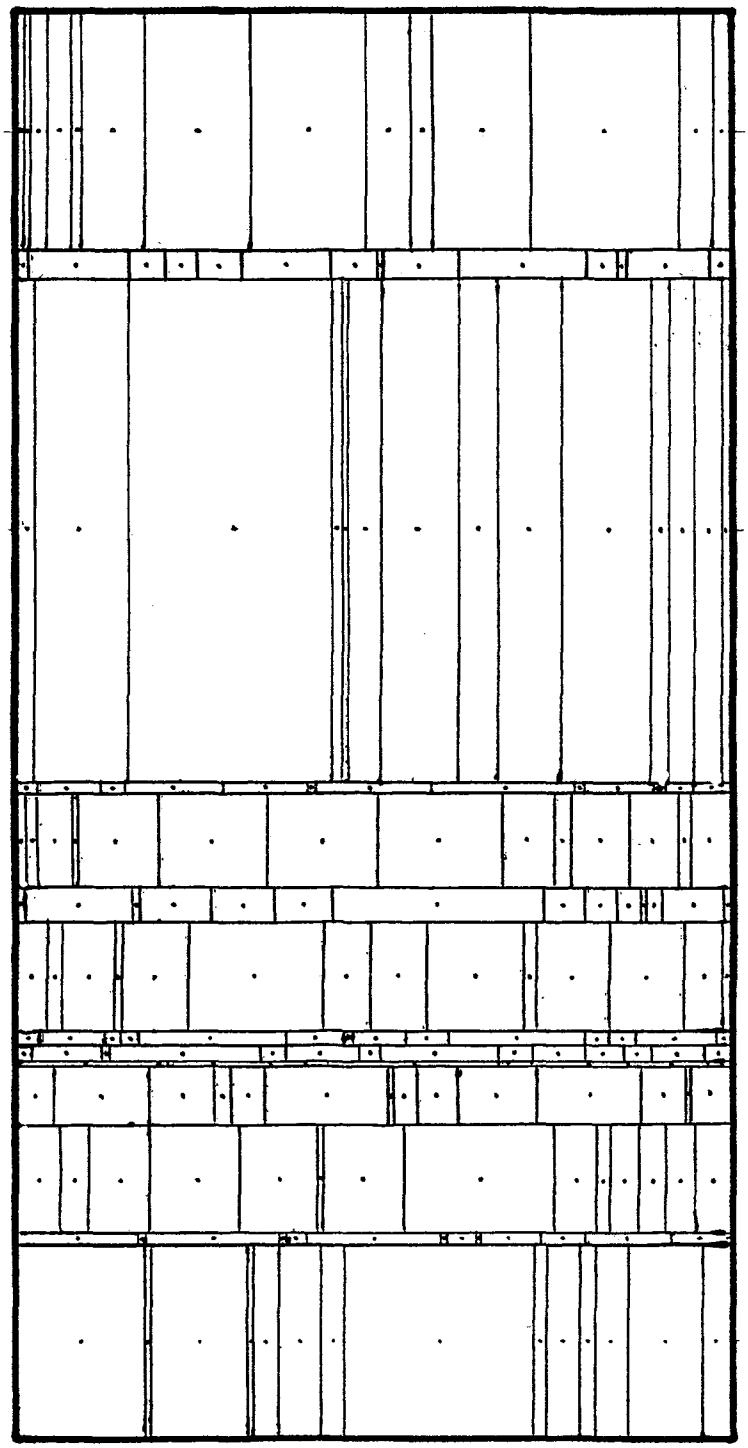

Figure 2.4(a) Example of an actual simulation of the rupture plane into patches.

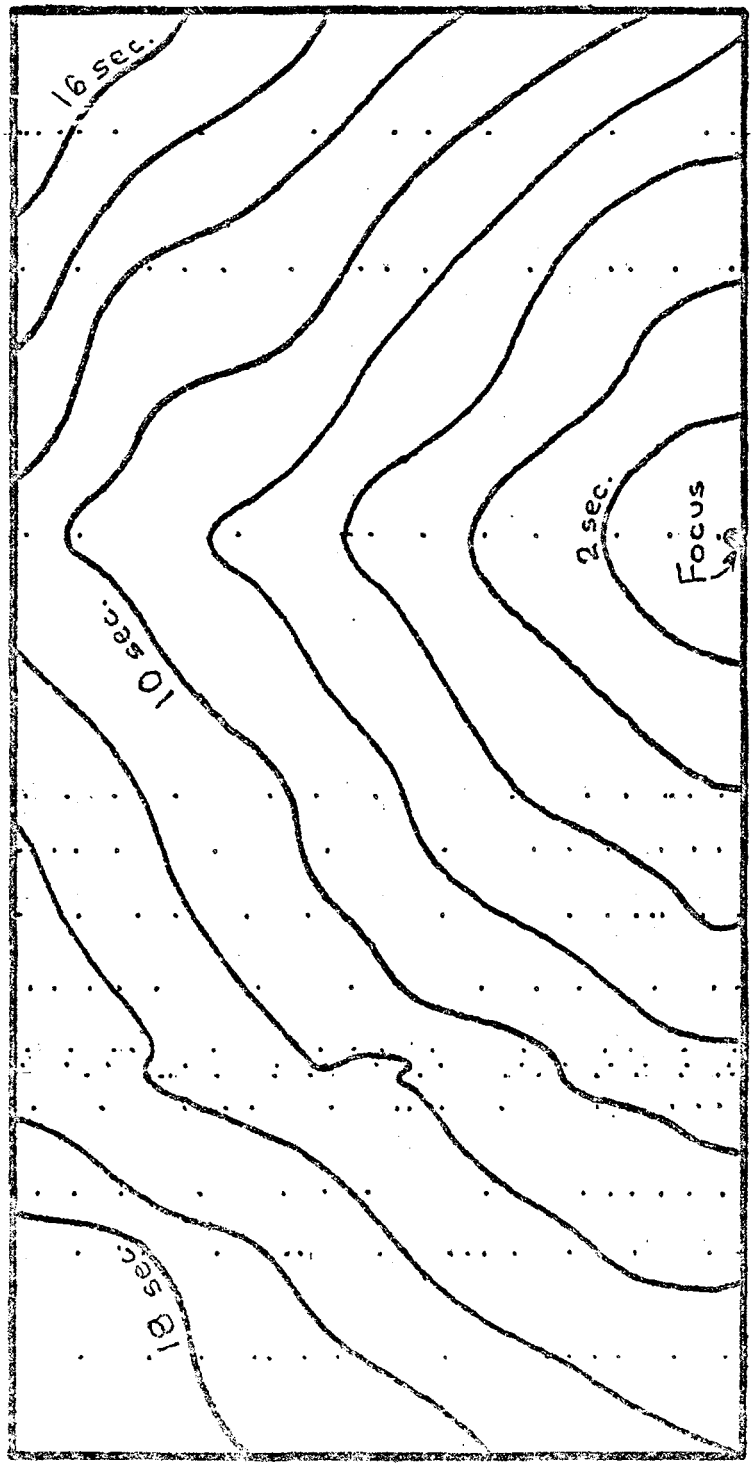

Figure 2.4(b) Example of isochrones of the rupture front for the fault discretization of Figure 2.4(a).

III. MOTION GENERATED BY A FINITE DISLOCATION

3.1 General Model

The model presented here is intended to be used in the generation of future earthquakes; not in the reproduction of any specific already recorded event. The emphasis is on its ability to generate a large number of records for the purpose of predicting the Power Spectral Density one may associate with a given potential rupture plane and observation site. Because it is to be used in engineering analysis of structures, the most important part of the motion to be considered is the strong motion. What appears on actual records as reflections or refractions at depth in the earth in the form of complex waves of significantly lower amplitude than the strong motion part is not considered in this analysis. Furthermore, as more and more site of critical facilities (such as Nuclear Power Plants) are found, or envisioned, at short distances of potentially active faults, the solution developed here includes the intermediate to near field effects of the earthquake motion.

Assume an isotropic homogeneous unbounded medium, and after Haskell (1964) assume that the elastic body waves are created by a moving finite dislocation which is a displacement discontinuity across the rupture plane. Maruyama (1969) has demonstrated that this dynamic dislocation is equivalent to a double couple of dynamic forces perpendicular and with opposite moments applied at the discontinuity. Later, Mikumo (1969), using Maruyama's work computed the P-wave form in the far-field for intermediate earthquakes. Using the same analytical model for S-waves and the stochastic model of progressive rupture in patches described in Section II, Savy (1978) developed a model of random earthquake generation. That model, however, was

limited to the far field approximation (Fraunhofer approximation, Aki & Richards, 1980) of S waves in the ϕ direction (see Fig. 3.1). The far field approximation is now considered too restrictive, and the solution is made here to include the intermediate to near field terms. In this effort, we start from the results of Maruyama (1969), with a slightly different notation. From Eq. 34 of Maruyama (1963), the Fourier transform of the displacement $u(Q, t)$ at any point Q in an infinite homogenous elastic medium due to the displacement discontinuity $\Delta\underset{\sim}{U}(\underset{\sim}{\xi}, t)$ over a plane Σ can be written in the following form:

$$U_m(Q, \omega) = \int_{\Sigma} \overline{\Delta u}_k (\underset{\sim}{\xi}, \omega)\, T_{k\ell}^{m}(\omega)\, \nu_\ell \, d\Sigma \qquad (3.1)$$

where: $\overline{\Delta u}_k(\underset{\sim}{\xi}, \omega)$ is the k-component of the Fourier transform of $\Delta\underset{\sim}{u}(\underset{\sim}{\xi}, t)$, $T_{k\ell}^{m}(\omega)$ is the m-component of the displacement field from equivalent dynamic double forces acting along the k- and ℓ axes. ν_ℓ are the direction cosines of the outward normal to the surface element, and repetition of indexes stands for summation.

3.2 Displacement Field Approximation

For the case of a discontinuity in the y-z plane as shown in Fig. 3.1, the displacement field T is given explicitly in Appendix 3.1. By making a transformation from the (x, y, z) system of coordinates the (ϕ, θ, r) spherical system and by separating the effect of P and S waves, T can be

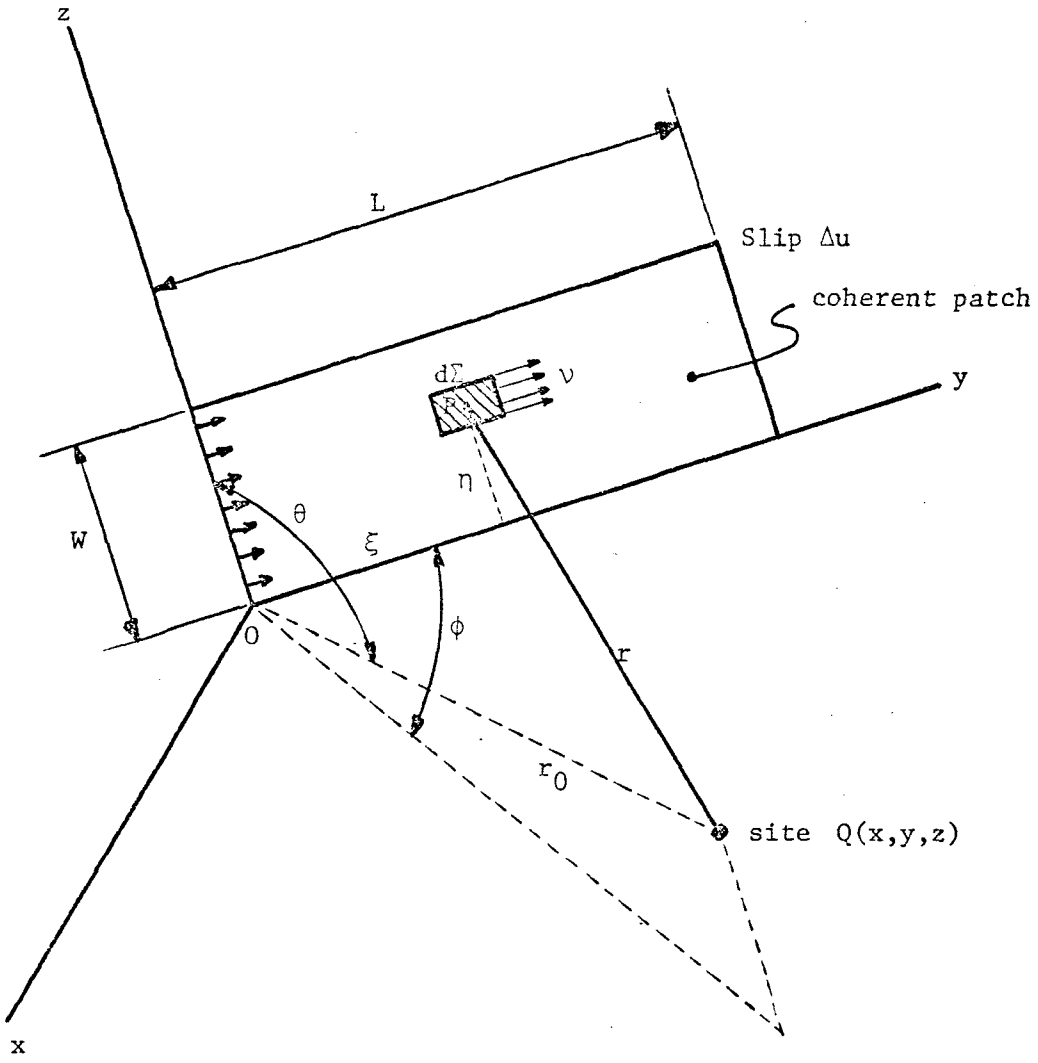

Figure 3.1 System's geometry for calculation of the motion at the Site Q created by the dislocation of a single coherent patch of length L and width W.

written as

$$T_{yx}^{sph} = \begin{bmatrix} T_r \\ T_\theta \\ T_\phi \end{bmatrix} = \mathcal{P}_{xy}^{sph} + \mathcal{S}_{xy}^{sph} \tag{3.2}$$

and by neglecting the terms of order greater than 2 in $(\frac{1}{r})$, where r is the distance from $d\Sigma$ to the observer, $\mathcal{P}$ and $\mathcal{S}$ become: (See Appendix 3.1)

$$\begin{aligned} \mathcal{P}_{yx}^{sph} &= \frac{i\omega}{4\pi\alpha r}\, e^{-i\frac{\omega r}{\alpha}}\, (\frac{\beta}{\alpha})^2 \left\{ R^P + \frac{2i\alpha}{\omega r}\,[R^S - 2R^P] \right\} \\ \mathcal{S}_{yx}^{sph} &= \frac{i\omega}{4\pi\beta r}\, e^{-i\frac{\omega r}{\beta}} \qquad \left\{ R^S - \frac{3i\beta}{\omega r}\,[R^S - R^P] \right\} \end{aligned} \tag{3.3}$$

where the vectors R^P and R^S are: (respectively in the radial direction and in the $(\theta\text{-}\phi)$ plane).

$$R^P = \begin{bmatrix} \sin^2\theta \sin 2\phi \\ 0 \\ 0 \end{bmatrix} \qquad R^S = \begin{bmatrix} 0 \\ \frac{\sin 2\theta \sin 2\phi}{2} \\ \sin\theta \cos 2\phi \end{bmatrix} \tag{3.4}$$

The second order approximation used here adds some correction terms to the first order, or far field, approximation. The P-wave component, then, is no longer only radial $(\vec{r})$ (colinear to R^P), and the S-wave component is no longer only in $(\vec{\theta}\text{-}\vec{\phi})$ (colinear to R^S). It requires that $(\frac{c}{\omega r})^2$ be small, (where c is either α or β, the P and S wave velocities) compared to 1 and $\frac{c}{\omega r}$, (see Appendix 3.1). The limiting value which defines the domain of validity of this approximation is derived in Appendix 3.2. It is found that

$$\frac{c}{\omega r} \leq \frac{1}{2} \tag{3.5}$$

meaning that the approximation is good for either high frequencies (ω large) or when the observation point is far from the source (r large), or both. Since this model is derived for engineering use of acceleration values rather than velocity, or displacement, the high frequency (10-15Hz) part of the spectrum is the most important. If we choose a lower bound of about 10Hz, the spatial domain of validity becomes:

$$r \geq \frac{2c}{\omega} \simeq .03c$$

which actually places the observation point in a region as close as a few hundred meters from the fault rupture. (i.e.: approximately 150 meters for the P-wave and probably around 90m for the S-wave, accounting for the fact that the wave velocity near the surface would be slower than at depth). In the lower frequency range, the solution would be approximately correct for observation points as close as ~1.5km and ~1km at 1Hz and 8km and 5km at .2Hz for P and S waves respectively.

It is shown in the appendix A3.1 that the correction terms to the far-field terms may be as high as to multiply the spectral values by 3 for the P wave and 2 for the S-wave for the limiting case where $\frac{c}{\omega r} = \frac{1}{2}$ at 10Hz; thereby showing the need for including them in near to intermediate field engineering calculations.

It is also interesting to note that the dimension of the correction terms is equal to the dimension of the far-field terms multiplied by $\frac{i}{\omega}$, or $\frac{-1}{i\omega}$. Therefore in the time domain they have the dimension of the integral of the far field terms (i.e.: velocity, if we are considering acceleration). This means that these terms adds a smoother component to the far field terms.

3.3 Model of Dislocation

Examining the several possibilities of dislocation directions and sense leads to the following cases.

1. Direction of the dislocation parallel to the y-axis with propagation either in the $y > 0$ or $y < 0$ sense. This case may be referred as the Strike slip model for our purpose.
2. Direction of the dislocation parallel to the z-axis with propagation either in the $z > 0$ or $z < 0$ sense. This case will be referred here as the Dip slip model.

As in the previous section, we concentrate on the strike slip model for propagation in the $y > 0$ direction. The other cases are presented at the end with reference to their development in Appendix A3.

After Aki (1967), we assume a dislocation in the form of a ramp function with parameters τ and D_0 as the finite rise time and static final dislocation, respectively. For the dislocation along the y-axis, starting at the origin of time, the Fourier transform of the dislocation function is:

$$\overline{\Delta u}(\omega) = D_0 \frac{\sin\omega \frac{\tau}{2}}{\omega \frac{\tau}{2}} e^{-i\omega \frac{\tau}{2}} \tag{3.6}$$

Since $T_{yx}(\omega)$ is proportional to $(i\omega)$ and $i\omega\ \overline{\Delta u}(\omega)$ is the Fourier transform of the time derivative of $\Delta u(t)$, Eq. 3.1 can be rewritten as:

$$U_m(Q, \omega) = \overline{\Delta \dot{u}}(\omega) \int_0^L \int_0^W \frac{T_{yx}^m}{i\omega} e^{-\frac{i\omega\xi}{v}} d\xi\, d\eta \tag{3.7}$$

where the term $e^{-\frac{i\omega\xi}{v}}$ accounts for the fact that the dislocation is moving along Oy with velocity v, L and W are the length and width of the finite

rupture, and it is assumed that the dislocation function is the same at all points of this finite rupture.

3.4 Second Order Finiteness Condition

In order to linearize the integrand of Eq. (3.7) due to the $\frac{1}{r}$ factor which comes in T_{yx}^{m} one is lead to make an approximation.

When only the far field terms are desired, it is common to make what is commonly called the Fraunhofer approximation (Aki & Richards, 1980) which is an approximation to the first order in $\frac{1}{r}$. It leads to a condition on the maximum size of the finite fault (L or W) associated with a given frequency. If r_0 is the distance from the origin of rupture 0 to the observer and f_{max} (in Hz) is the desired maximum frequency, the maximum size is given by:

$$L_{max} = \frac{1}{\sin\phi} \sqrt{\frac{r_0 \beta}{2 f_{max}}} \tag{3.8}$$

The necessity of considering a second order approximation, however, leads to a different condition. This second order finiteness condition gives the maximum size of the finite rupture as a function of the distance r_0 and the maximum desired frequency f_{max}. It is derived in Appendix A.3 as:

$$L_{max} = \left[\frac{\beta}{2 f_{max}} \cdot \frac{r_0^2}{\sin^2\phi \cos\phi} \right]^{1/3} \tag{3.9}$$

This L_{max} given here refers to the case of the S-wave. For the p-wave, β would be replaced by α and L_{max} would be multiplied by $(\frac{\alpha}{\beta})^{1/3}$. Solving for r we may find the minimum distance r_{min} for which the finiteness condition is satisfied, for a given source length L and azimuthal direction ϕ.

$$r_{min} = \left\{\frac{2f_{max}}{\beta} \sin^2\phi \cos\phi\right\}^{1/2} L^{3/2} \qquad (3.10)$$

A comparison between the first and second order approximation's domain of validity is presented in the Appendix A.33. Figure A3.3 shows the general shape of these domains. The numerical values given in Table A3.1 are associated with a maximum frequency of 20Hz and a largest dimension L = .5km to 15km. The second order approximation appears to be much better for ϕ close to 90° and overall it will be better than the first order approximation, except perhaps at very small angles ϕ for which the domain of non validity of the solution is smaller for the first than for the second order, that is for distances of the order of L (See Figure A3.3). The second order solution takes over for angles increasing with decreasing L. In the numerical case of Appendix A, this angle ϕ_S is given by the solutions of the following equation:

$$\sin^2\phi_S - \frac{c}{2f_{max}L} \cos\phi_S = 0$$

For L in the range of 0.5 to 3km, f_{max} = 20Hz and c = β = 3.5km. ϕ_S varies from 24 degrees to 10 degrees, with corresponding r values of .5 to 3km, that is of the order of magnitude of L. This case where the first order solution is better than the second order does not have to be considered however, because it corresponds to very short distances from the source to the receiver and was excluded in the condition expressed by Eq. 3.5.

The two conditions, expressed by Eq. 3.5 and 3.9-3.10 are different in nature. The first one says that our solution does not apply for receiver distances r smaller than a certain value. The second one says that

for a given patch of largest dimension L, the distance r also has to be greater than a certain value r_{min}. While the first one is imperative, the second condition can be overridden by discretizing the patch in smaller sub-patches in such a way that finally their largest dimension satisfies Eq. 3.9.

Hence, for all practical purposes the first condition is the only limiting one in the capabilities of the model.

3.5 Second Order Approximation of the Acceleration

The distance r from the receiver Q(x, y, z) to the point of rupture $P(0,\xi,\eta)$(Fig. 3.1) approximated to the second order is:

$$r \simeq r_0\left[1 - \frac{\xi}{r_0}\sin\theta\cos\phi - \frac{\eta}{r_0}\cos\theta\right]$$
$$\text{and}\quad \frac{1}{r} \simeq \frac{1}{r_0}\left[1 + \frac{\xi}{r_0}\sin\theta\cos\phi + \frac{\eta}{r_0}\cos\theta\right] \tag{3.11}$$

Defining

$$A_\alpha = \left(\frac{\beta}{\alpha}\right)^2 \frac{1}{\alpha} R^P \quad , \quad B_\alpha = 2\left(\frac{\beta}{\alpha}\right)^2 [R^S - 2R^P],$$
$$A_\beta = \frac{1}{\beta} R^S \quad , \quad B_\beta = \frac{-3}{\beta}[R^S - R^P] \tag{3.12}$$

then, combining Eq. (3.3), (3.4), (3.5) and (3.7) gives:

$$\frac{U(Q,\omega)}{\Delta\bar{u}(\omega)} = \frac{1}{4\pi}\int_0^L\int_0^W \frac{1}{r}\left\{\left[A_\alpha + \frac{i}{\omega r}B_\alpha\right]e^{-\frac{i\omega r}{\alpha}} + \left[A_\beta + \frac{i}{\omega r}B_\beta\right]e^{-\frac{i\omega r}{\beta}}\right\} e^{-\frac{i\omega\xi}{v}} d_\xi d_\eta \tag{3.13}$$

where $U(q, \omega)$ is the 3-component vector displacement.

The above equation can be re-written into a sum of two integrals, one for each wave type, P and S, as:

$$\frac{U(Q,\omega)}{\Delta\bar{u}(\omega)} = I_\alpha + I_\beta \tag{3.14}$$

and, using (3.11) and (3.12):

$$I_\alpha = \frac{1}{4\pi r_0}\int_0^L\int_0^W [A_\alpha+\frac{i}{\omega r_0}(1+\xi\frac{\sin\theta\cos\phi}{r_0}+\frac{\eta\cos\theta}{r_0})B_\alpha][1+\frac{1}{r_0}(\xi\sin\theta\cos\phi+\frac{\eta}{r_0}\cos\theta]$$
$$\exp[-\frac{i\omega r_0}{\alpha}(1-\frac{\xi}{r_0}\sin\theta\cos\phi-\frac{\eta}{r_0}\cos\theta)]\, e^{-\frac{i\omega\xi}{v}}\, d\xi d\eta \tag{3.15}$$

Similarly for I_β, all the α's are replaced by β's.

Expanding I_α into a sum of integrals and neglecting the term of order $\frac{1}{r_0^3}$ and higher gives:

$$I_\alpha = \frac{LW}{4\pi r_0} e^{-\frac{i\omega r_0}{\alpha}}\left\{A_\alpha[J_1^\alpha J_2^\alpha + \frac{1}{r_0}(J_2^\alpha J_3^\alpha + J_4^\alpha J_1^\alpha)]\right.$$
$$\left. + \frac{i}{\omega r_0}B_\alpha[J_1^\alpha J_2^\alpha + \frac{2}{r_0}(J_2^\alpha J_3^\alpha + J_4^\alpha J_1^\alpha)]\right\} \tag{3.16}$$

where:

$$J_1^c = \frac{1}{W}\int_0^W e^{\frac{i\omega\cos\theta}{c}\eta}\, d\eta$$

$$J_2^c = \frac{1}{L}\int_0^L e^{-i\omega\xi(\frac{1}{v}-\frac{\sin\theta\cos\phi}{c})}\, d\xi$$

$$J_3^c = \frac{1}{W} \int_0^W \eta \cos\theta \; e^{\frac{i\omega\cos\theta}{c}\eta} \, d\eta$$

$$J_4^c = \frac{1}{L} \int_0^W \xi \sin\theta\cos\phi \; e^{i\omega(-\frac{1}{v} + \frac{\sin\theta\cos\phi}{c})\xi} \, d\xi \qquad (3.17)$$

and c may take the value α or β when associated with P or S waves.

Performing the integrations and simplifying gives I_α:

$$I_\alpha = \frac{L\,W}{4\pi r_0} e^{-\frac{i\omega r_0}{\alpha}} \left\{ A_\alpha J_1 J_2 \left[1 + \frac{i}{\omega r_0} \left(\alpha \left(1 - \frac{e^{2i\omega T_W^\alpha}}{J_1^\alpha} \right) - \frac{L\sin\theta\cos\phi}{2T_L^\alpha} \left(1 - \frac{e^{-2i\omega T_L^\alpha}}{J_2^\alpha} \right) \right) \right] \right.$$

$$\left. + \frac{i}{\omega r_0} B_\alpha J_1^\alpha J_2^\alpha \left[1 + \frac{2i}{\omega r_0} \left(\alpha \left(1 - \frac{e^{2i\omega T_W^\alpha}}{J_1^\alpha} \right) - \frac{L\sin\theta\cos\phi}{2T_L^\alpha} \left(1 - \frac{e^{-2i\omega T_L^\alpha}}{J_2^\alpha} \right) \right) \right] \right\} \qquad (3.18)$$

where:

$$J_1^c = e^{i\omega T_W^c} \frac{\sin\omega T_W^c}{\omega T_W^c}$$

$$J_2^c = e^{-i\omega T_L} \frac{\sin\omega T_L}{\omega T_L}$$

$$T_W^c = \frac{W}{2} \frac{\cos\theta}{c} \qquad (3.19)$$

$$T_L^c = \frac{L}{2} \left(\frac{\Lambda}{V} - \frac{\sin\theta\cos\phi}{c} \right)$$

For the case of a dislocation propagating in the z direction and for the dip slip case with propagation along Oy or Oz the integrals involved in the solution have the same form as in Eq. 3.17. The development of these cases appears in Appendix A4.

Finally for the basic case of strike slip with propagation along Oy, using the following definition of seismic moment M_0:

$$\begin{aligned} M_0 &= \mu \; D_0 LW \\ &= \rho\beta^2 \; D_0 LW \end{aligned} \tag{3.20}$$

where ρ is the medium mass density and μ is the earth's rigidity ($\mu \simeq 3\ 10^{10}$ Pascals). The displacement then becomes:

$$U(Q,\omega) = \frac{M_0\, e^{-i\omega\frac{\tau}{2}}}{4\pi\rho r_0} \; \frac{\sin\omega\frac{\tau}{2}}{\omega\frac{\tau}{2}} \left\{ J_1^{\alpha} J_2^{\alpha} e^{-\frac{i\omega r_0}{\alpha}} \left[A_{\alpha}\left(1+\frac{i\alpha}{\omega r_0}K^{\alpha}\right) + \frac{i}{\omega r_0} B_{\alpha}\left(1+\frac{2i\alpha K^{\alpha}}{\omega r_0}\right) \right] \right.$$

$$\left. + J_1^{\beta} J_2^{\beta}\, e^{-\frac{i\omega r_0}{\beta}} \left[A_{\beta}\left(1+\frac{i\beta}{\omega r_0}\, K^{\beta}\right) + \frac{iB_{\beta}}{\omega r_0}\left(1+\frac{2i\beta}{\omega r_0}K^{\beta}\right) \right] \right\} \tag{3.21}$$

where:

$$K^c = \left(1 - \frac{e^{2i\omega T_W^c}}{J_1^c} \right) - \frac{L\sin\theta\cos\phi}{2cT_L^c} \left(1 - \frac{e^{-2i\omega T^c}}{J_2^c} \right)$$

$$(c = \alpha \text{ or } \beta) \tag{3.22}$$

Recalling Eq. (3.2) for collection of the terms, and using the identity between displacement and acceleration:

$$\Gamma(Q,\omega) = -\omega^2\, U(Q,\omega)$$

gives the vector acceleration in the spherical system $(\Gamma_r, \Gamma_\theta, \Gamma_\phi)$,

$$\Gamma(Q,\omega) = -\frac{M_0\, e^{-i\omega\frac{\tau}{2}}}{4\pi\rho r_0}\,\frac{\sin\omega\frac{\tau}{2}}{\omega\frac{\tau}{2}}\,\omega^2 g(Q,\omega) \tag{3.23}$$

where:

$$g(Q,\omega) = \begin{bmatrix} \gamma_1 \left[\frac{G^\alpha}{\alpha^3}\left[1+\frac{i\alpha}{\omega r_0}(K^\alpha-4)\right] + \frac{G^\beta}{\beta^3}\left(\frac{3i\beta}{\omega r_0}\right)\right] \\ \gamma_2 \left[\frac{G^\alpha}{\alpha^3}\left(\frac{2i\alpha}{\omega r_0}\right) + \frac{G^\beta}{\beta^3}\left[1+\frac{i\beta}{\omega r_0}(K^\beta-3)\right]\right] \\ \gamma_3 \left[\ " \qquad\qquad " \qquad\qquad "\ \right] \end{bmatrix}$$

$$\begin{cases} \gamma_1 = \sin^2\theta\, \sin 2\phi \\ \gamma_2 = \frac{1}{2}\sin 2\theta\, \sin 2\phi \\ \gamma_3 = \sin\theta\, \cos 2\phi \end{cases}$$

and

$$G^c = J_1^c\, J_2^c\, e^{-\frac{i\omega r_0}{c}}\,, \quad (c = \alpha \text{ or } \beta).$$

3.6 Triggering Time Shift, Attenuation and Free Surface Effect

In order to apply Eq. (3.23) to the model of rupture described in Chapter II and to account for the attenuation of different frequency waves with distance, the solution of Eq. (3.23) is multiplied by:

$$(1)\quad e^{-i\omega T_g}$$

$$(2)\quad \exp\left(-\frac{r_0\omega}{2Qc}\right)\exp\left[-\frac{i\omega r_0}{c}\left(1-\frac{1}{\pi Q}\,\mathrm{Log}_e\left|\frac{\omega}{\omega_0}\right|\right)\right] = e^{-\frac{r_0\omega}{2Qc}}\,C(\omega) \qquad (3.24)$$

where:

(1) is an application of the shift theorem, it acocunts for the fact that the rupture of this patch initiated at time T_g, (the triggering time) at the origin 0 of the patch.

(2) accounts for the material damping of the medium through which the waves propagate. (c is either equal to α or β for P or S wave). This attenuation effect is taken care of by the first part,

$$e^{-\frac{r_0\omega}{2Qc}}$$

but the use of this filter violates the causality principle so that a phase correction factor $C(\omega)$ is applied. This correction factor is taken from Kjartansson (1979). Q is the quality factor of the medium, it is related to the material damping ξ commonly used in engineering by $Q = \frac{1}{2\xi}$, and ω_0 is a constant value used to center the filter. In this model the value of ω_0 is chosen equal to 10π rad/sec (corresponding to 5Hz).

The final expression for the vector acceleration is then

$$\Gamma(Q,\omega) = -\frac{M_0\,\omega^2}{4\pi\rho r_0}\, e^{-i\omega\left(\frac{\tau}{2}+T_g\right)}\, \frac{\sin\omega\frac{\tau}{2}}{\omega\frac{\tau}{2}}\, g(Q,\omega) \qquad (3.25)$$

where $g(Q,\omega)$ is modified to include the attenuation by changing the definition of G^c to the following:

$$G^c = J_1^c J_2^c \exp\left[-\frac{\omega r_0}{2cQ}\left(1 + 2i\left[Q-\frac{1}{\pi}\,\mathrm{Log}_e\left|\frac{\omega}{\omega_0}\right|\right]\right)\right] \qquad (3.26)$$

The above solution applies to an infinite medium. The effect of the free surface is approximately accounted for by multiplying the amplitude of the acceleration by 2. Anderson (1976) showed that is is a good approximation for a strike slip case. For other cases however, it could constitute a rather poor approximation, especially for S waves when the angle of incidence becomes larger than 30° with the normal to the free surface. But since this approximation is an overestimation of the amplitude of the motion, it is used for all cases in this analytical model in order to preserve its simplicity.

IV. MOTION GENERATED BY AN ASSEMBLAGE OF PATCHES

4.1 Motion Generated by the Entire Fault Rupture

4.1.1 Frequency Domain Superposition

The Fourier transform of the acceleration at a site Q, created by the rupture of a single patch i, is given by Eq. 3.25. This solution assumed that the propagating medium is linear elastic. Therefore the motion at the site Q due to the rupture of the N patches comprising the entire fault is the sum of the motion created by the rupture of each individual patch. This is expressed by the following equation:

$$\Gamma(Q, \omega) = \sum_{i=1}^{N} \Gamma_i(Q, \omega, T_{g_i}) \tag{4.1}$$

where: $\Gamma_i(Q, \omega, T_{g_i})$ is given by Eq. 3.25 and T_{g_i} is the triggering time of patch i (i.e.: $T_g = T_{g_i}$ in Eq. 3.25).

For each simulation of an earthquake the triggering time T_{g_i} of a patch i is computed according to the scheme of rupture presented in Chapter II. The rise time τ_i for the i^{th} patch is computed by an empirical relationship proposed by Geller (1976). The effect is to make τ_i proportional to the square root of the area of the patch (i.e., roughly proportional to its length) which is in agreement with what was proposed by Aki (1980).

4.1.2 Time Domain Superposition

It is clear that the superposition could also be done in the time domain, but it implies that the time history for each patch be computed by inverse Fourier transform and superimposed to obtain the final motion. This technique is much more time consuming than first computing the

frequency domain function and taking its inverse Fourier transform at the end, so that the final time history of the acceleration at the site is given by the inverse Fourier transform of the expression in 4.1.

$$\gamma(Q, t) = FT^{-1}[\Gamma(Q, \omega)] \tag{4.2}$$

4.2 Simulation of an Ensemble of Synthetic Earthquakes

4.2.1 General

In some cases, such as in the study of the response of structures to seismic loading, it is necessary to perform a number of analyses with an ensemble of input time histories. The ensemble to be considered may be representative of a certain type of earthquakes for which some of the parameters are known with enough confidence to be considered as deterministic (i.e.: constant) and others are only known with uncertainty so that they are considered as random variables.

A Monte Carlo simulation technique may be used to generate the uncertain parameters of each sample event and an ensemble of events can be created in that fashion.

In theory, any of the parameters, source, geometry or attenuations can be considered as random variables. However, in most simple cases one is interested in a type of earthquake with fixed strength (seismic moment, fixed geometry, and constant material properties (P and S wave velocity, earth density, attenuation properties-quality factor). For instance, in some of the research now performed using this model, the statistical characteristics of the motion created by a well defined type of earthquakes is examined. In that case only the rupture process is assumed to be random,

that is the patch pattern is simulated and the focus is given a random location at each new simulation and the attenuation and directivity effects are studied. The Fig. 4.1 is an example of calculation of 4 synthetic earthquakes for a series of earthquakes with constant seismic moment, material properties and fixed patches pattern (Fig. 4.1(a)), but with random focus location. The Fig. 4.1(b), (c), (d), (e) show how drastically different the time histories of the acceleration at a same site can be, emphasizing possibilities of constructive and destructive interferences.

4.2.2 Frequency Domain Statistics of the Ensemble of Synthetic Earthquakes

The creation of large ensembles of time histories remains expensive, due to the amount of calculations required. One alternative, chosen here, is to define the statistics of the ensemble in terms of the Power Spectral Density (PSD) of the ensemble of time histories. This is much less time consuming, because each simulation $\Gamma(Q, \omega)$ (Eq. 3.25) needs only be computed for a few frequency points (say 20 to 30) instead of large numbers (say 512 or 1024) for time domain analyses.

Changing our previous notations, let $\Gamma_k(\omega)$ be the Fourier transform of the motion obtained in the k^{th} simulation of an ensemble of N samples. An estimate of the PSD for that ensemble can be computed by an averaging process (Bendat and Piersol, 1971) as follows:

$$P(\omega) = \left\langle \frac{\Gamma(\omega) \cdot \Gamma^{*}(\omega)}{T} \right\rangle \qquad (4.3)$$

where: $P(\omega)$ is the estimate of the Power Spectral Density (PSD)

$\Gamma(\omega)$ is the motion function in the frequency domain

T is the time duration of the motion.

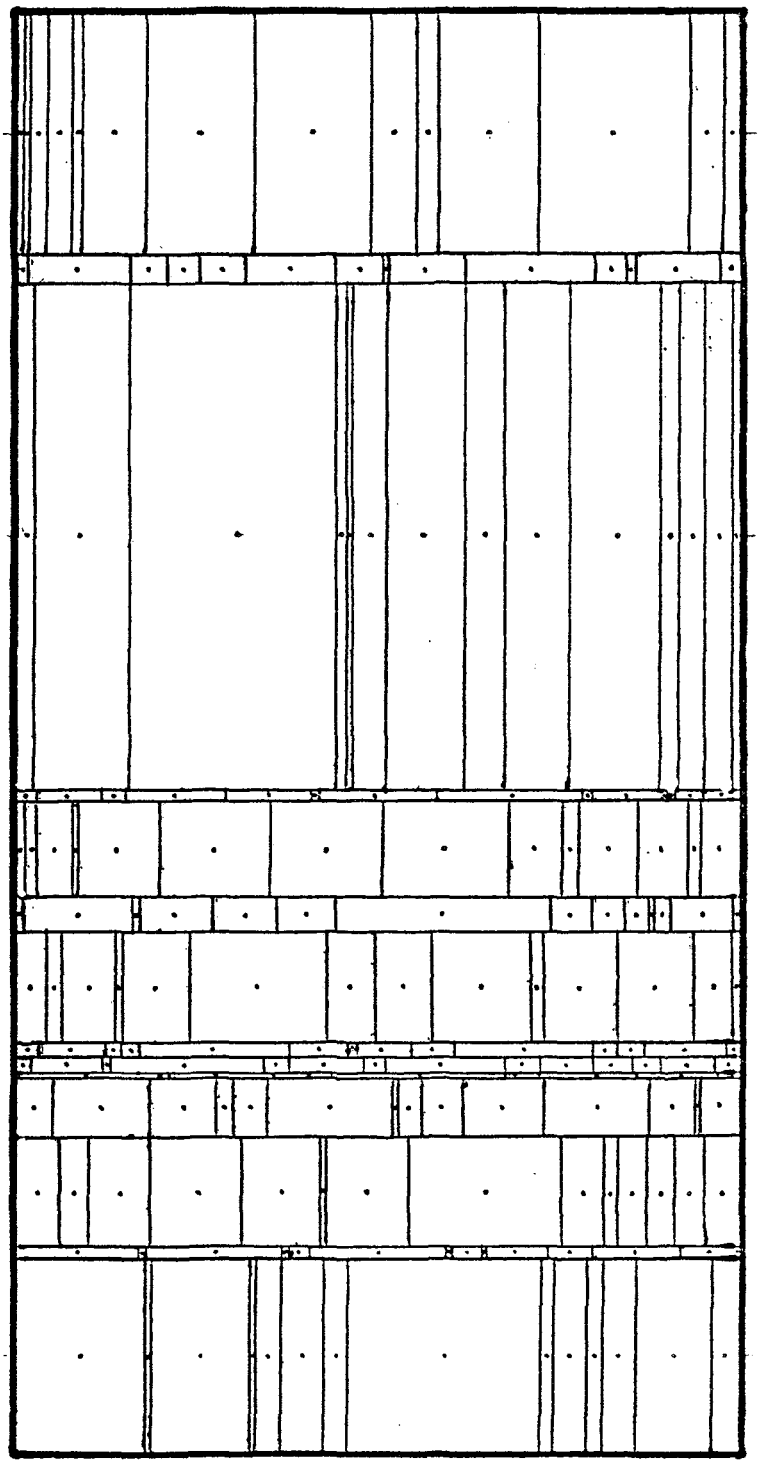

Figure 4.1(a) Example of an actual simulation of the rupture plane into patches. (Figure 2.4(a) repeated.)

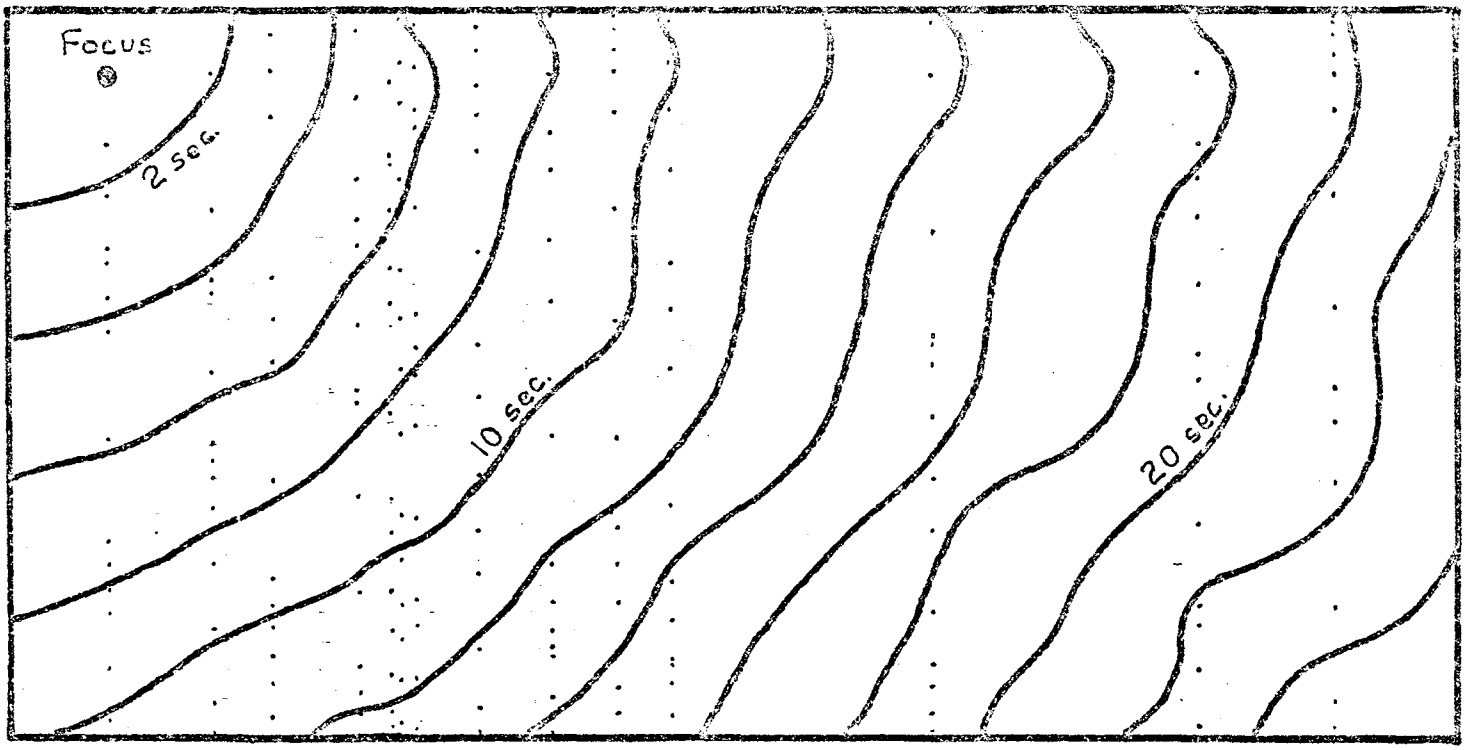

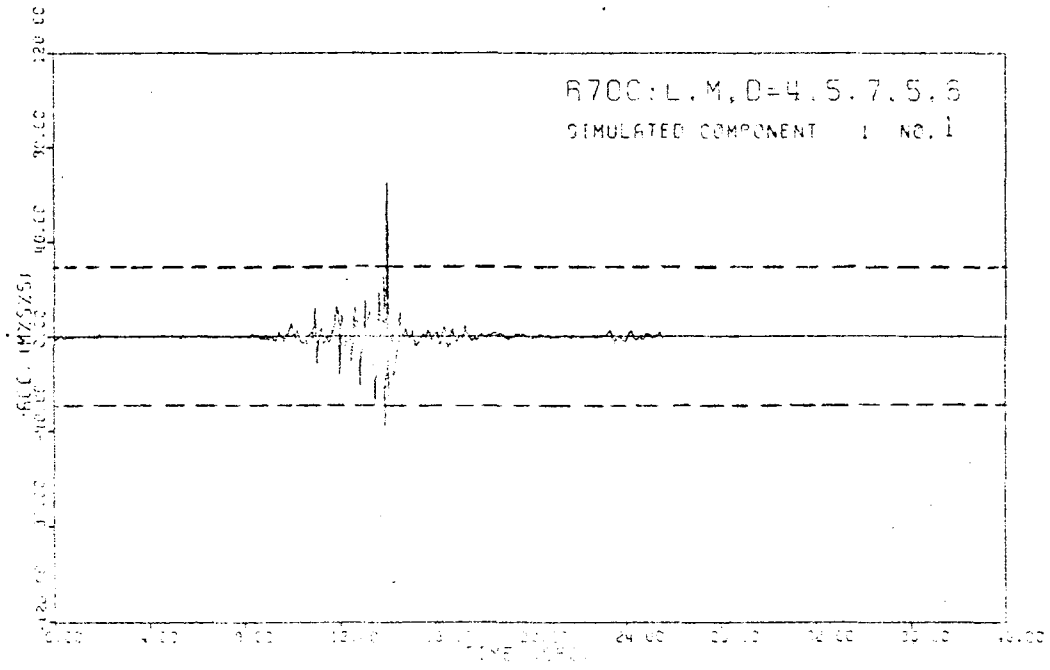

Figure 4.1(b) Isochrones of the rupture front and synthetic accelerogram for focus in a upper corner.

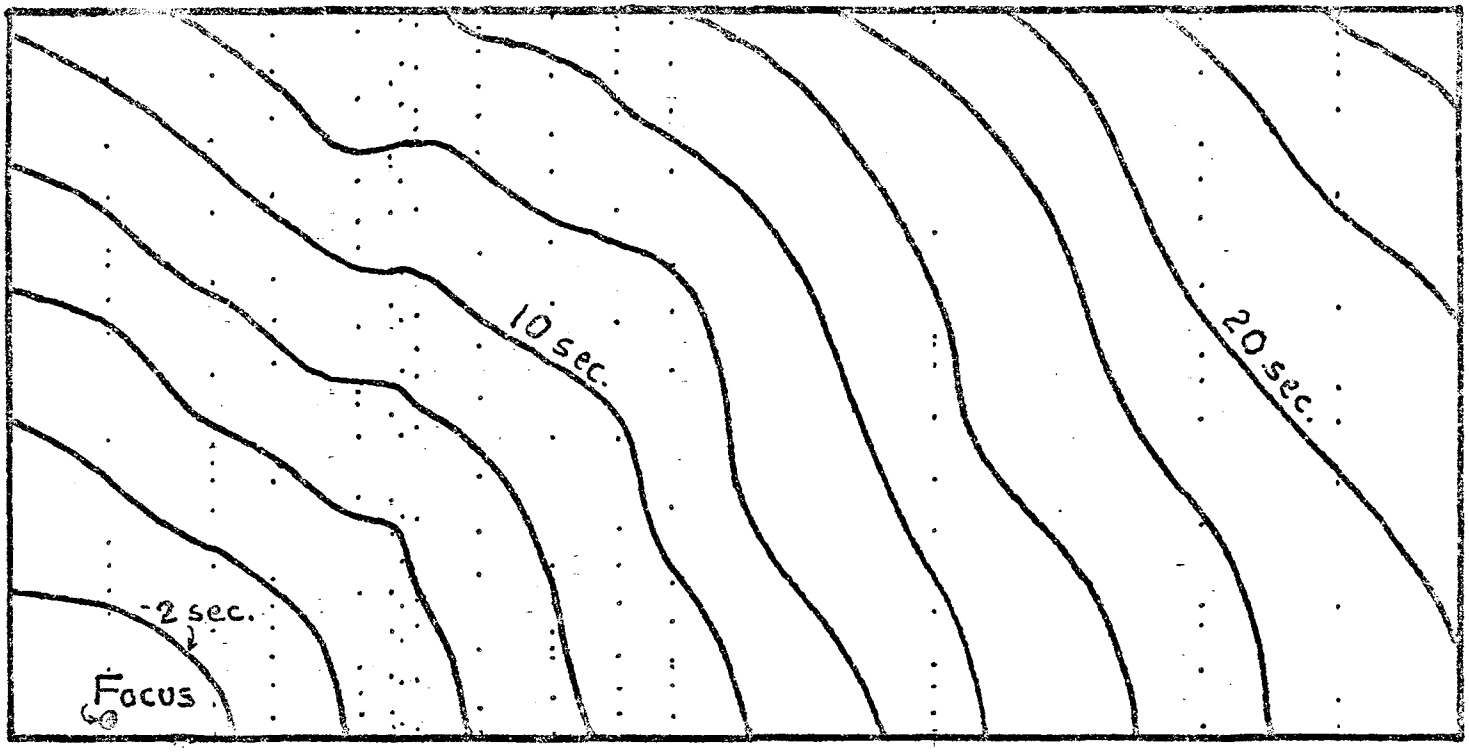

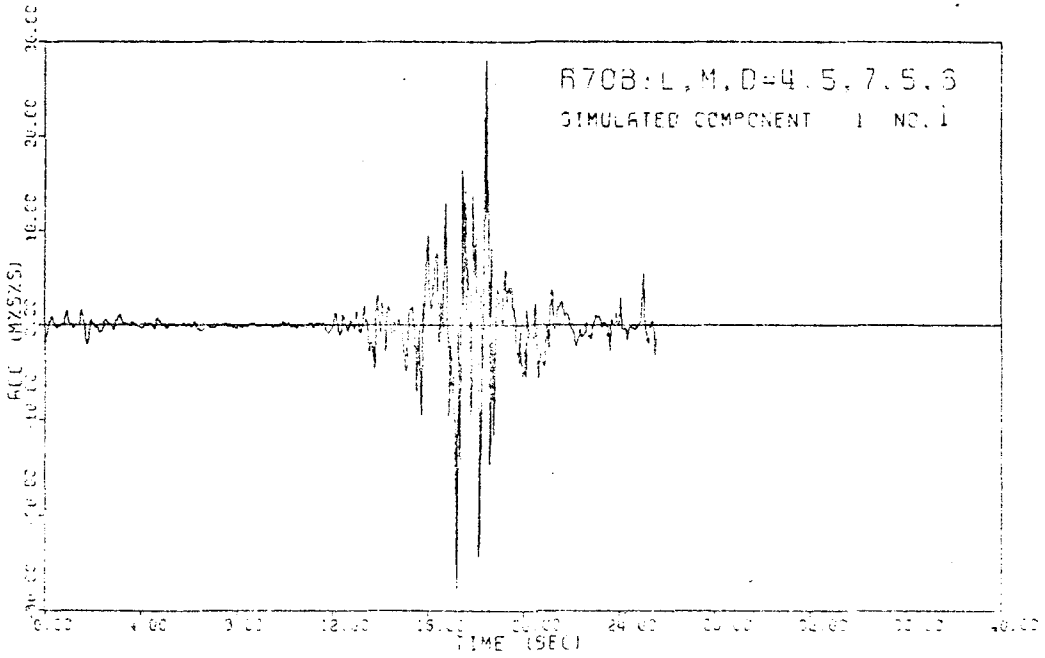

Figure 4.1(c) Isochrones of the rupture front and synthetic accelerogram for focus in a lower corner.

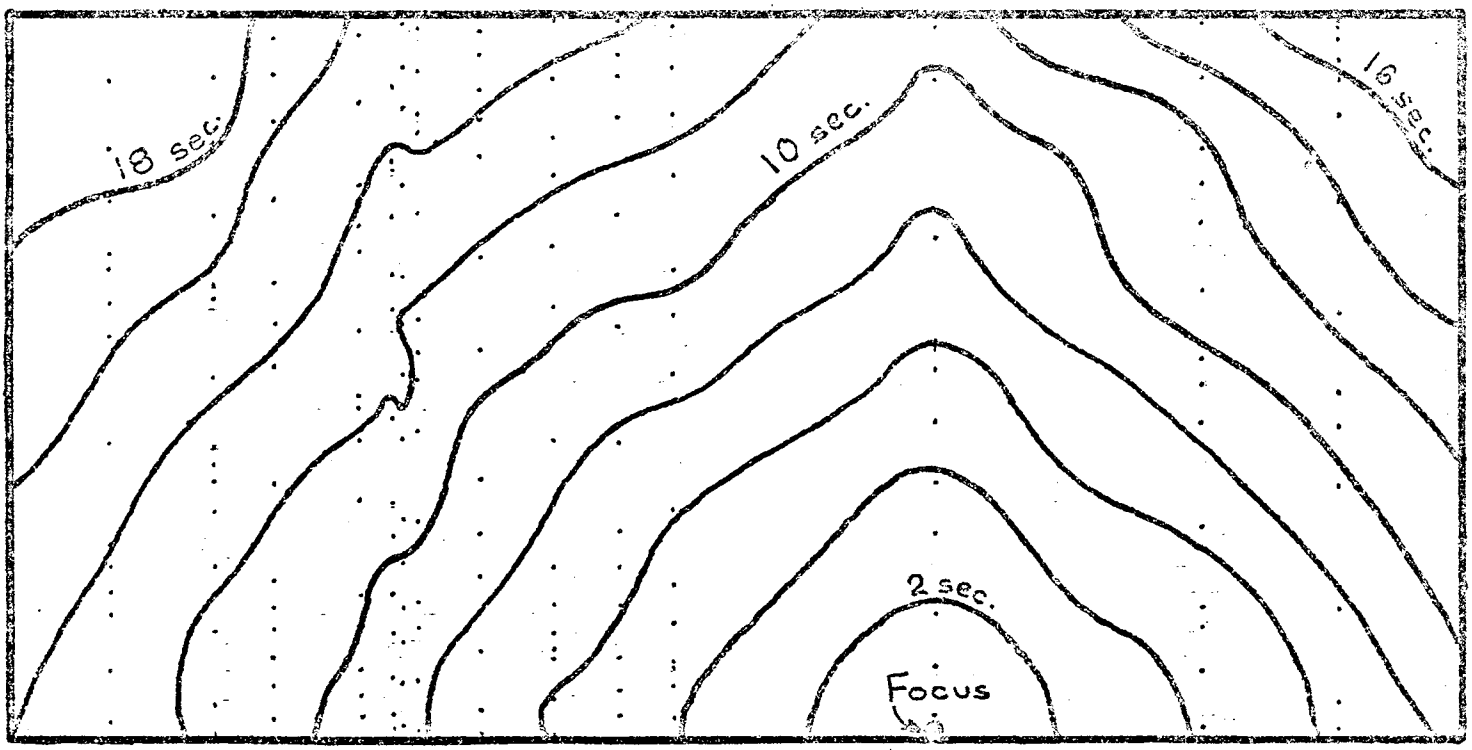

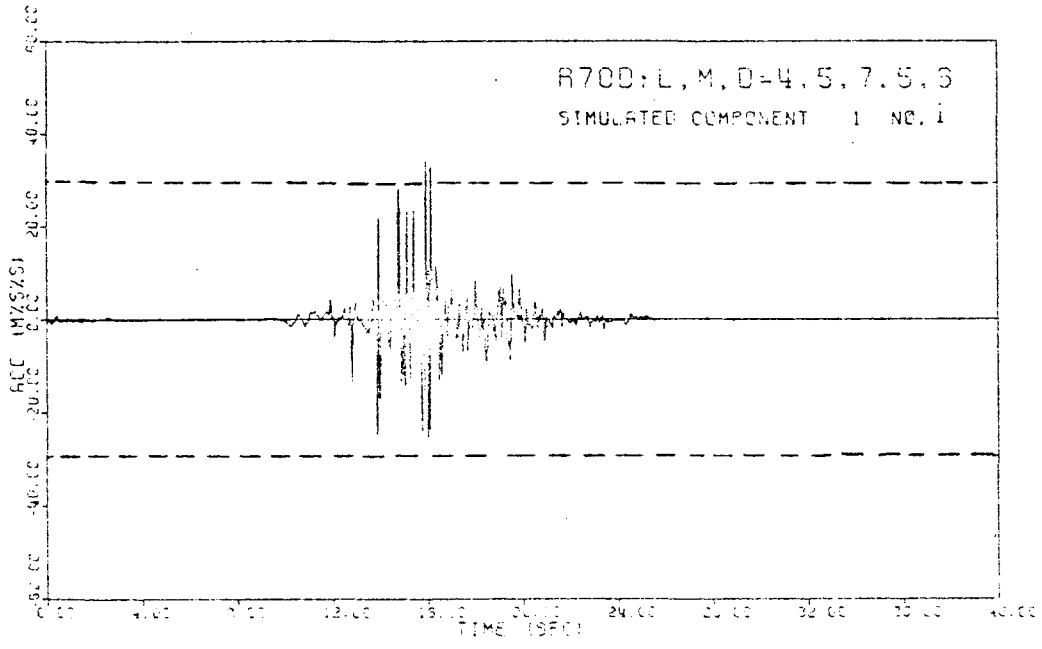

Figure 4.1(d) Isochrones of the rupture front and synthetic accelerogram for focus placed at random at the bottom of the fault.

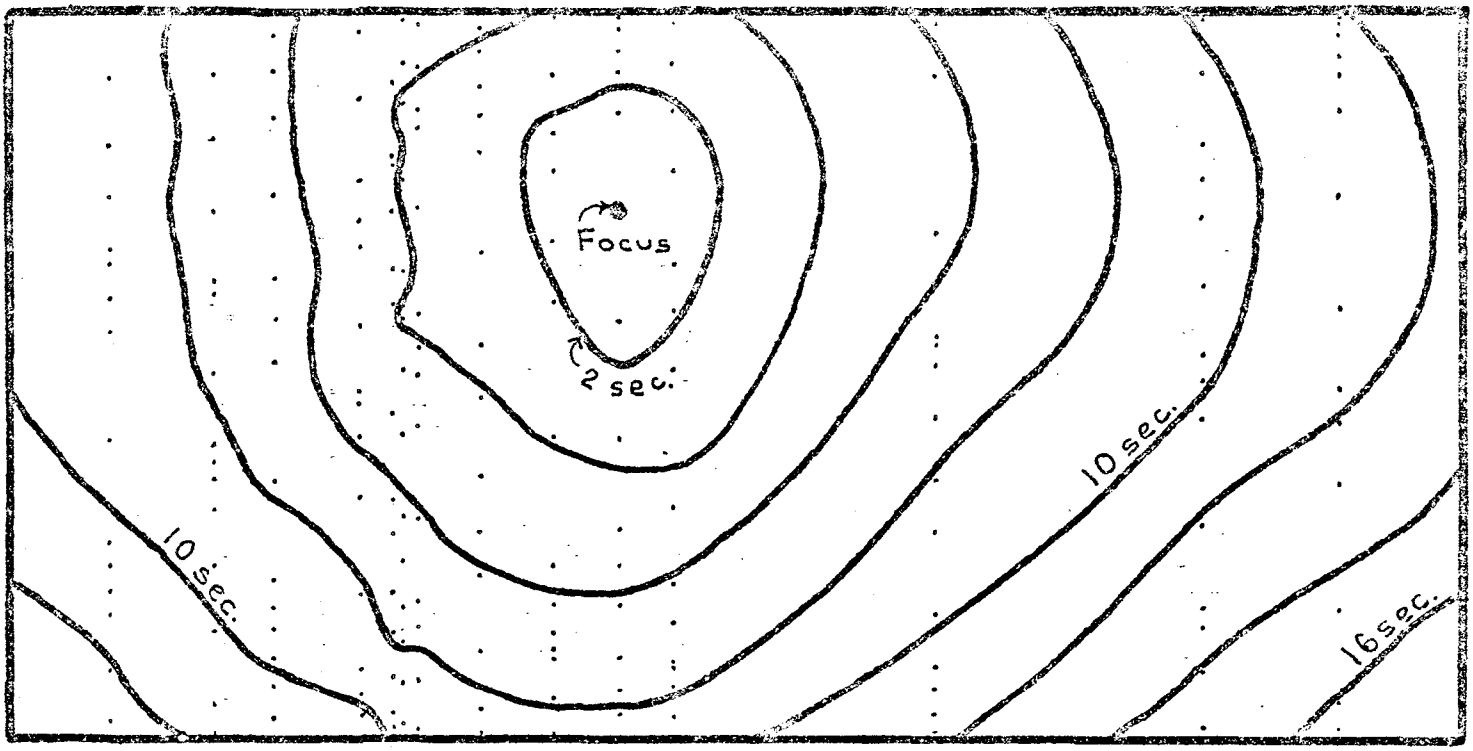

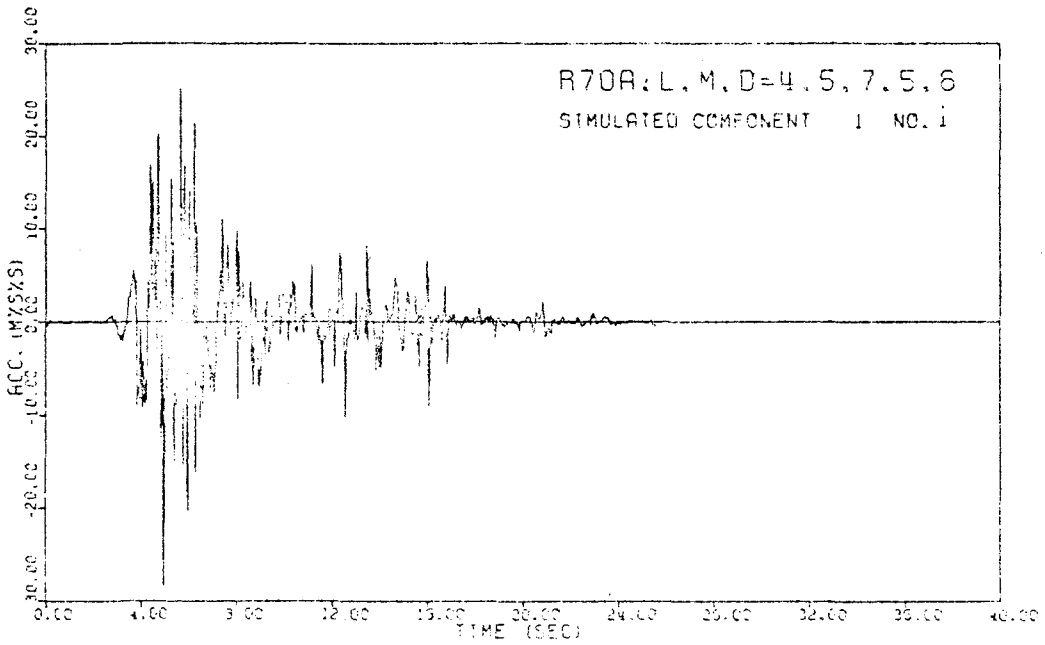

Figure 4.1(e) Isochrones of the rupture front and synthetic accelerogram for focus placed at random (the values on the acceleration axis are only indicative of the relative amplitudes between Figure 4.1a, b, c, and d).

More explicitly $P(\omega)$ is computed as follows:

$$P(\omega) = \frac{1}{N} \sum_{k=1}^{N} \frac{\Gamma_k(\omega)\ \Gamma_k^*(\omega)}{T_k} \tag{4.4}$$

Since the actual time equivalent function of $\Gamma_k(\omega)$ is a non-stationary process, it appears that the choice of T_k is a critical one in the computation of the PSD.

Many quantitative definitions of strong motion duration have been proposed (Bolt, 1974; Trifunac and Brady, 1975; Trifunac and Westermo, 1977; Vanmarcke and Lai, 1977; Perez, 1974; McCann and Shah, 1979; Esteva and Rosenblueth, 1964; Housner, 1965, Aptikayev, 1975; Hays, 1975; Kameda and Ang, 1977). All of these definitions are based on the recorded accelerations (or derived velocities or displacements) at a site during an earthquake; none use properties of the source, such as the duration of rupture of the fault. It is not our purpose here to propose another definition of duration, but it appears that none of the existing ones is adequate here.

It is assumed here that the equivalent period of time during which the motion can be considered stationary is the cumulative time duration during which the energy arriving at the site is above an arbitrary set fraction (5%) of the peak energy arrival rate. This is illustrated in the sketch of Fig. 4.2 (see Appendix 4.1). It is, in a sense, similar to looking at the time derivative of a Husid plot, Husid et al., 1967, setting a threshold at a fraction of the peak, and adding the time periods during which the function is above that threshold. Thus T_k is an estimate of the actual total duration of strong motion. If an event is, for instance, made of two separate strong shocks with very little energy arriving at the site in between, say for a few seconds, that period of relative quiescence is discarded in the calculation of T_k.

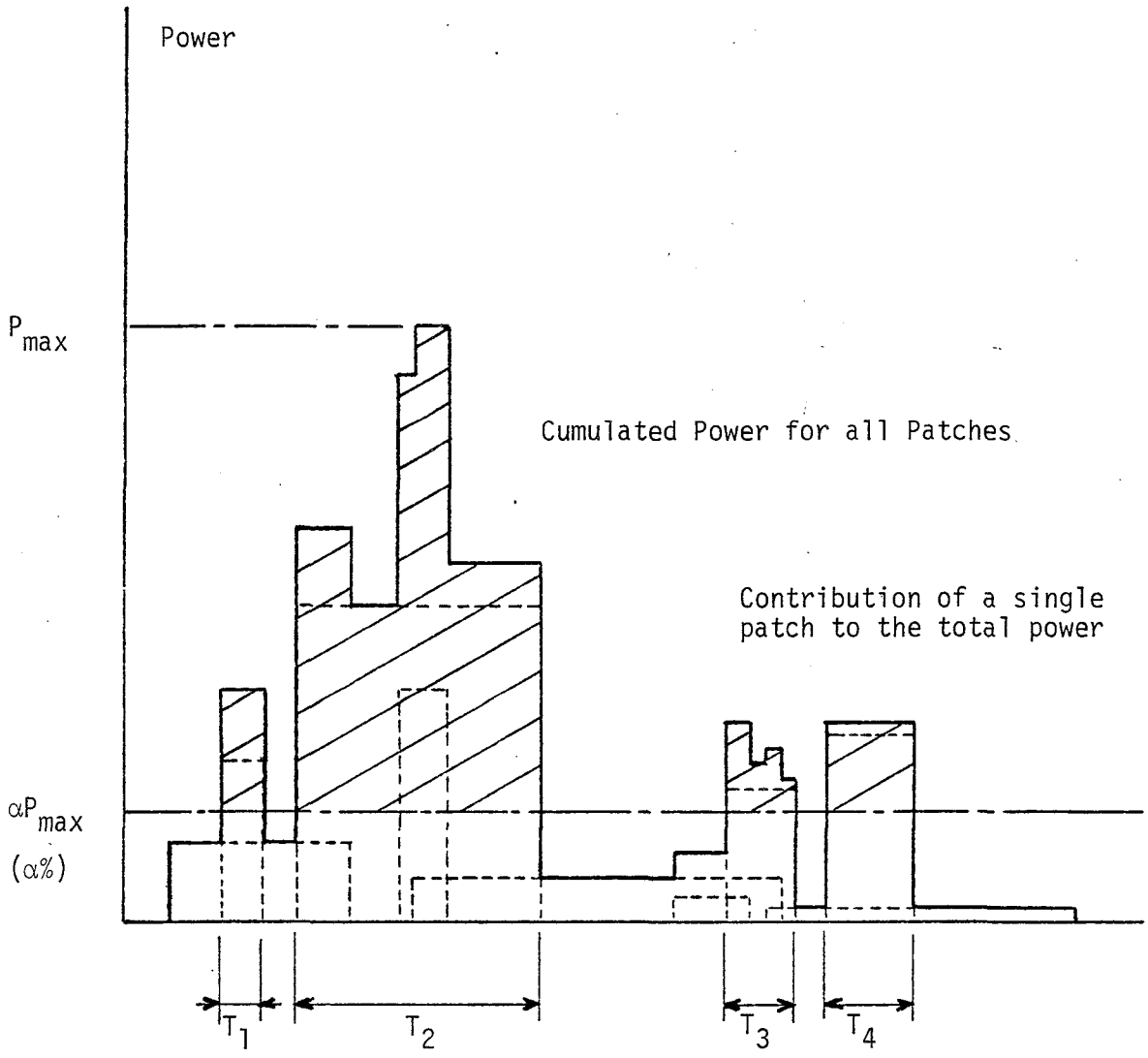

Total Strong Motion Duration = $T_1 + T_2 + T_3 + T_4$

Figure 4.2 Average power proportional function.

As an example, the Figure 4.3, taken from Papageorgiou, 1981, shows a Husid plot and its derivative for a record of the Kern County earthquake. In this case the normalized RMS acceleration time history is the equivalent of the Power proportional function derived in this study (see Appendix 4.1).

A set of 15 Fourier Amplitude spectra for simulation of a given fault rupture is plotted in Fig. 4.4. The average Power Spectral Density computed according to Eq. 4.4 is shown in Fig. 4.5. For each simulation, the total duration of the strong motion is calculated as described above.

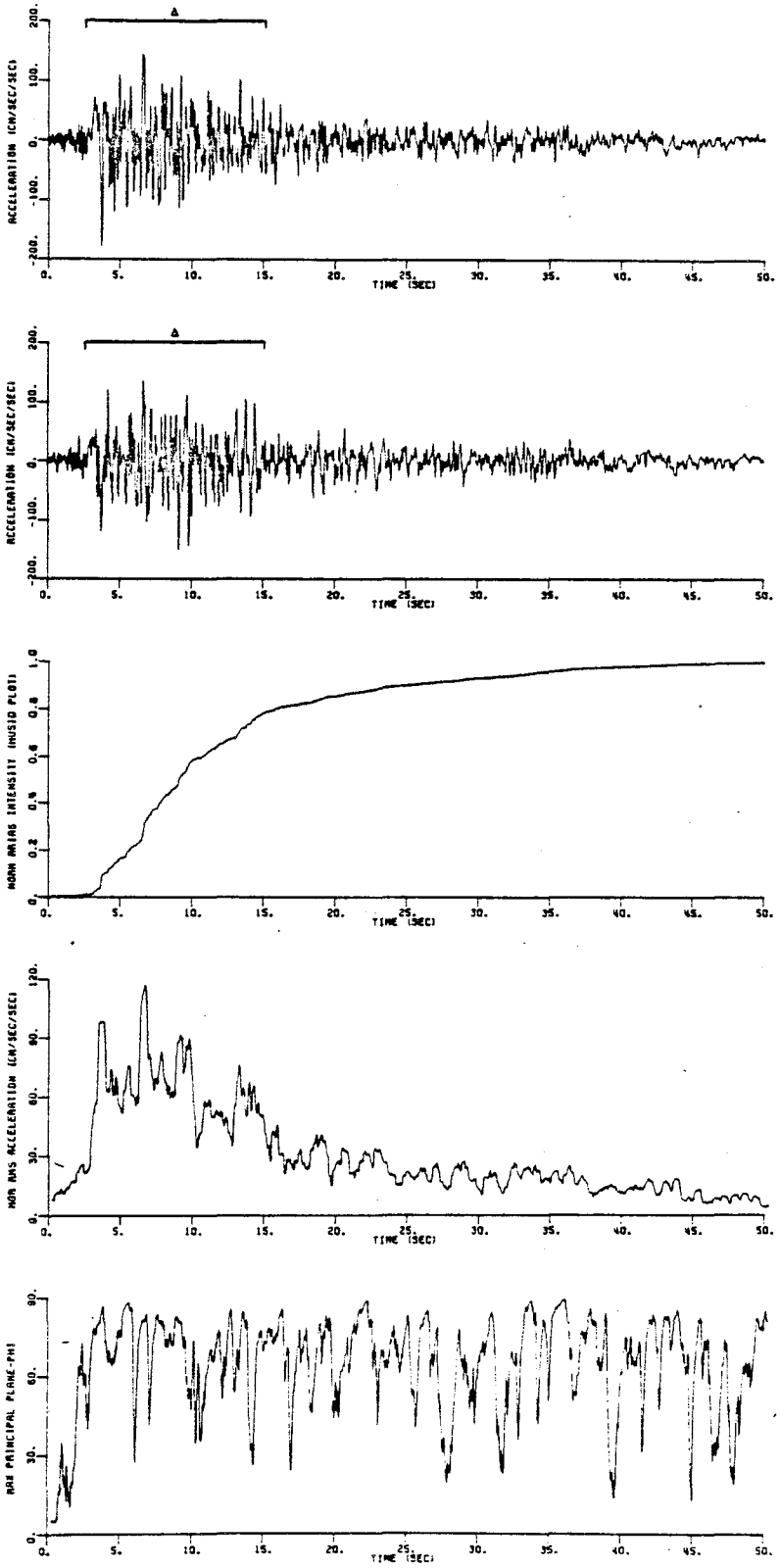

Figure 4.3 Radial and transverse accelerograms (w.r.t. epicenter) of the ground motion recorded at the Taft Lincoln school station during the Kern County earthquake of 1952, and the corresponding Husid plot, moving time window root mean square acceleration, and time variation of principal plane (ϕ-angle). (Taken from Papageorgiou, 1981)

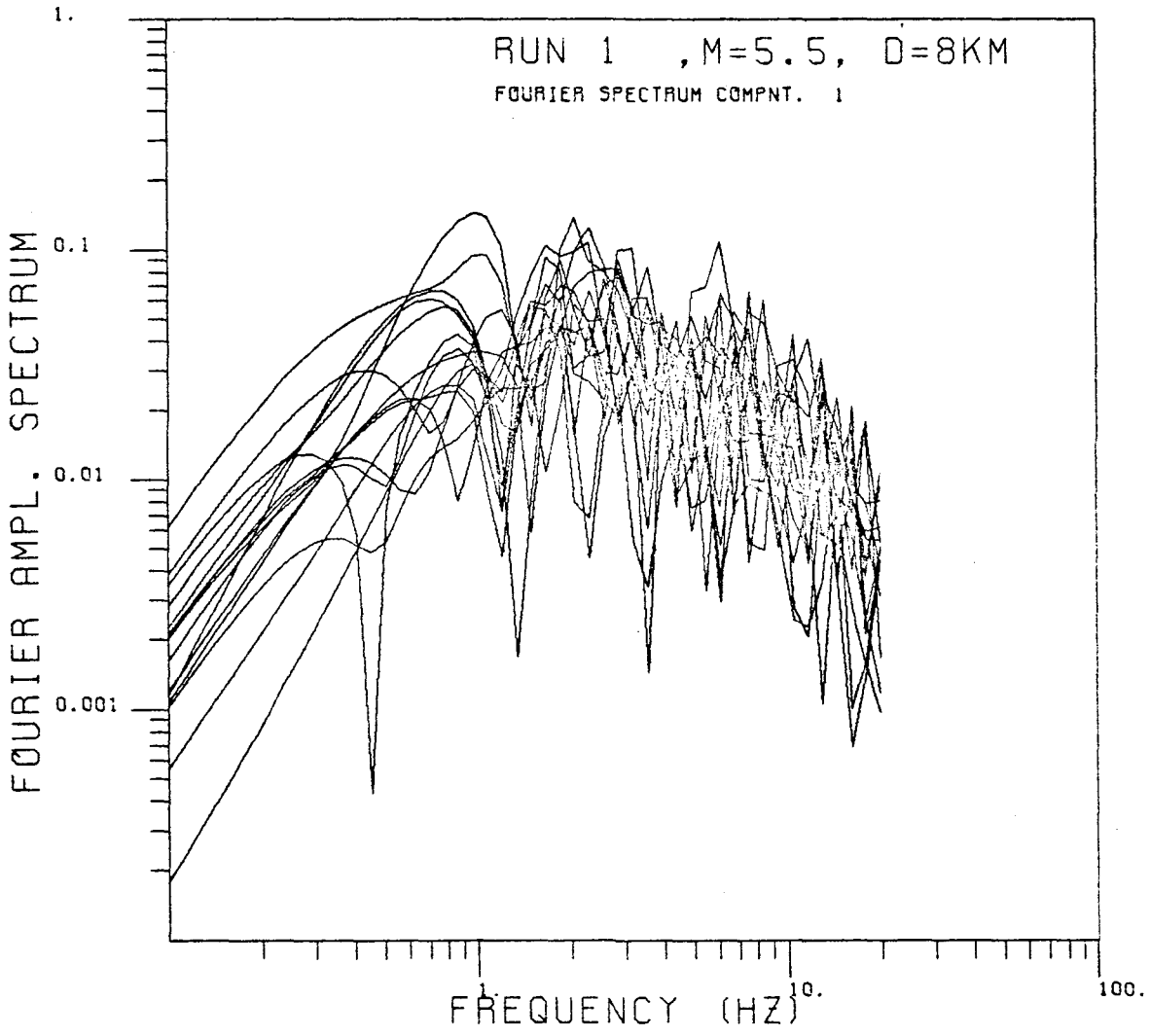

Figure 4.4 Example of 15 simulation of Fourier spectra for computation of the power Spectral density of Figure 4.5.

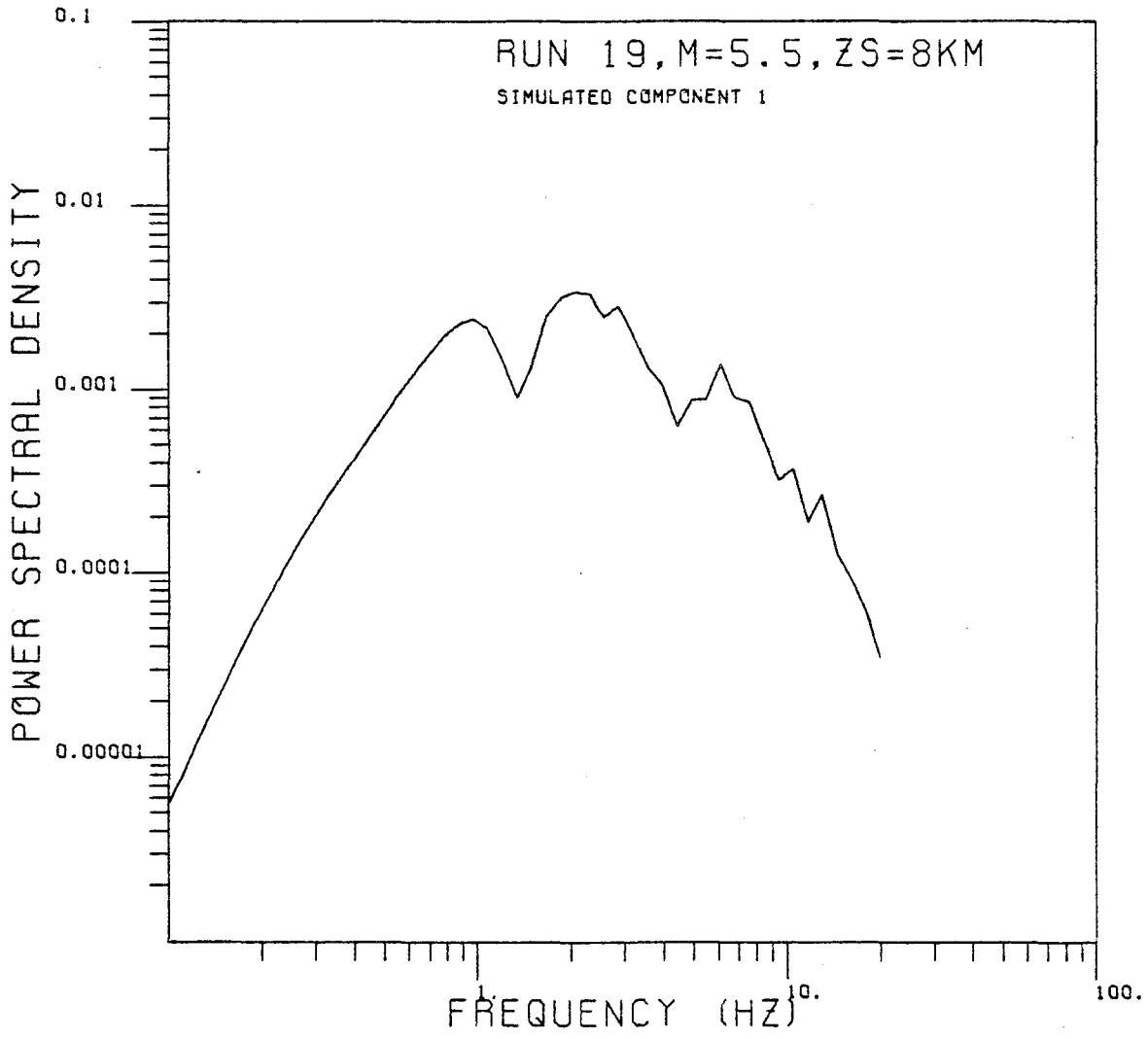

Figure 4.5 Example of a Power Spectral Density. This case was obtained with the 15 Fourier Amplitude spectra of Figure 4.4.

V. ESTIMATION OF THE AVERAGE PATCH SIZE IN AN EARTHQUAKE FAULT RUPTURE

5.1 Introduction

Very little is known regarding the actual rupture process of earthquakes. As a result it is rarely possible to select confidently any particular set of parameters to be used in a strong motion simulation model. The average patch length, $\bar{\ell}$, or coherence length is one such parameter in the strong motion models which include the effect of the random rupture propagation. These models are very sensitive to small variation in the average patch length so that a reliable determination of it is of paramount importance. Until recently the method used in selecting $\bar{\ell}$ was mostly intuitive for generic cases, such as in the generation of ensembles of earthquakes for risk analysis. The average RMS acceleration and peak acceleration were compared with an often arbitrary set of results from actual records, and $\bar{\ell}$ was modified until the results of the simulation agreed with actual data. In geophysics the research in this domain has been mostly concentrated on trying to reproduce records by trial and error, thereby coming up with an actual rupture process where the main patches are individually identified, such as in the case of San Fernando (Shakal, 1979). Other techniques involve looking at the area of aftershocks in the fault rupture plane and identifying the main shock rupture process as the undisturbed aftershock region (Aki, 1979) and (Eaton et al, 1970). In this case it is therefore possible to have an estimate of the average size $\bar{\ell}$ as well as the maximum patch's length. This is the case for the Parkfield earthquake 1966. In some cases, such as in the 1857 Fort Tejon earthquake, it is possible to estimate the spacing between barriers, (Aki, 1979), from a

geologists description of the surface trace. Since the distance between barriers can be regarded as the length of a patch, then it provides some estimate of the average patch length as well as maximum values and other statistics, such as the probability distribution of the length.
The same operation can be performed also for other fault traces. It was found (Wallace, 1973) that the probability distribution function of fault strands was approximately negative exponential, and we show that it may be only an approximation of another simple law.

In this chapter, we propose to use statistical considerations together with basic physical assumptions to come up with an estimate of $\bar{\ell}$, then devise a methodology to select $\bar{\ell}$ in the strong motion simulation models of large ensembles of artificial earthquakes.

5.2 Statistical Relationships Between Average Slip, Average and Maximum Patch Length

5.2.1 Basic assumptions

The technique developed here depends on three major physical assumptions; the subsequent ones, less important for the results, can rather be seen as approximations.

These three major assumptions are:

(1) In a given earthquake, where the actual stress drop may actually be represented by a spatial stochastic process, (Andrews, 1980) we assume that it is a constant over the whole rupture surface. Thus implying that, for a given patch, the ratio of the maximum slip over the length of the patch is a constant:

$$\frac{\Delta U_{max}}{\ell} = a \ ; \ a \text{ constant} \qquad (5.1)$$

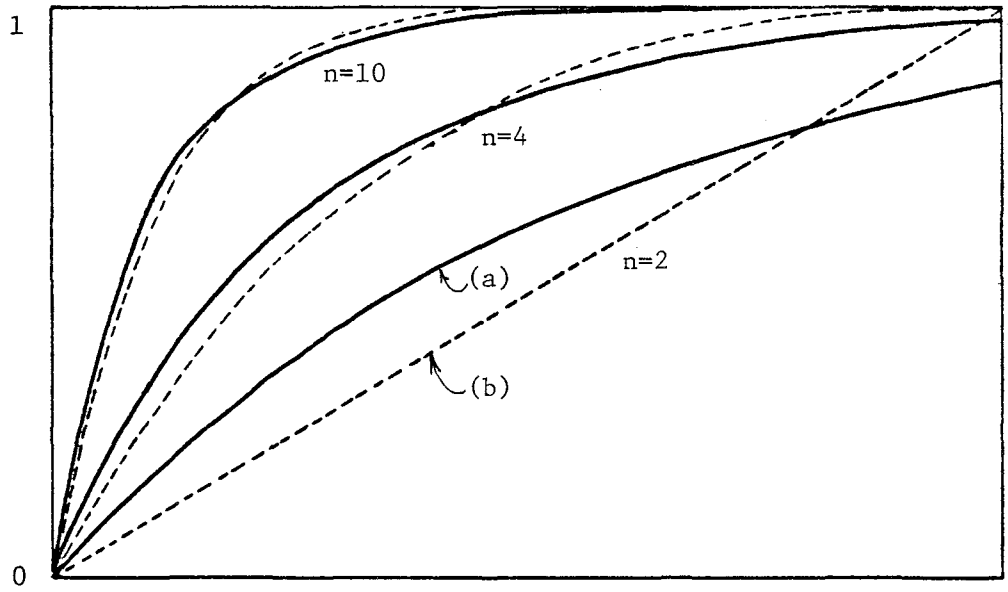

Figure 5.1 Comparison between, (a), the negative exponential distribution function and, (b), the distribution of i.i.d. Segments between two fixed points for several numbers of segments.

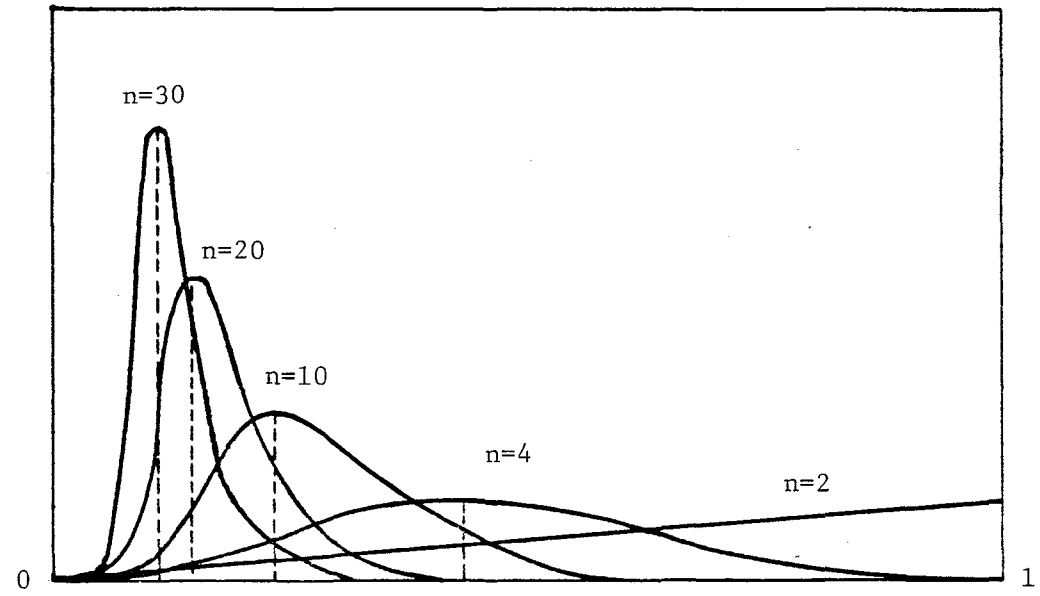

Figure 5.2 $f_{\ell_{max}}(\ell)$; $0 \leq \ell \leq 1$

for number of segments n = 2,4,10,20 and 30

(2) The generation of an earthquake is created by the rupture of the part of a fault located between two strong barriers which physically limit the extent of the propagation and form the extremities of the fault rupture. The region located betweeen the two strong barriers may then be ruptured in smaller segments separated by weaker barriers thus forming the patches. The process of rupture between the two strong barriers is assumed to be homogeneous, so that the distribution of the weaker barriers can be regarded as uniformly distributed between the two stronger ones. The intervals between barriers, L', (i.e., the patches' lengths), are then marginally identically distributed (Kendall & Moran, 1970). The probability distribution is:

$$\left.\begin{aligned} f_{L'}(\ell) &= \frac{(n-1)}{L}\left(1-\frac{\ell}{L}\right)^{n-2} \quad \text{, density} \\ & \qquad\qquad 0 \leq \ell \leq L \\ F_{L'}(\ell) &= 1-\left(1-\frac{\ell}{L}\right)^{n-1} \quad \text{, cumulative} \end{aligned}\right\} \tag{5.2}$$

where (n-1) is the number of weaker barriers, so that n is the number of segments and, L is the total length of the rupture, that is the distance between the two stronger barriers.

The mean value and standard deviation of the patch length are therefore given by:

$$\bar{\ell} = \frac{L}{n} \tag{5.3}$$

$$\sigma_{L'} = \frac{L}{n}\left(\frac{n-1}{n+1}\right)^{1/2} = \bar{\ell}\left(\frac{n-1}{n+1}\right)^{1/2} \tag{5.4}$$

And the covariance between any two segment lengths L'_i, L'_j is (see Appendix 5.3):

$$COV(L'_i, L'_j) = -\frac{L^2}{n^2(n+1)} = \frac{-\bar{\ell}^2}{(n+1)}, \text{ for } i \neq j \qquad (5.5)$$

It is interesting to notice that when the fault rupture becomes large, that is when n becomes large, the distribution of L' converges towards the negative exponential distribution, as found by Aki (1979) for the San Andreas fault.

Keeping $\ell/\bar{\ell}$ constant, and using (5.3) in (5.2) gives:

$$f_{L'}(\ell) = \frac{1}{\bar{\ell}} \left(1+\frac{1}{n-1}\right)^{-1} \left(1-\frac{1}{n}\frac{\ell}{\bar{\ell}}\right)^{n-2}$$

And,

$$\lim_{n\to\infty} f_{L'}(\ell) = \frac{1}{\bar{\ell}} e^{-\frac{\ell}{\bar{\ell}}}$$

For small n these two distributions could be significantly different however, as it is shown in Fig. 5.1 in the comparison of the two cumulative distributions for values of n between 2 to 10.

(3) We thirdly assume that the gross statistical properties of the rupture, such as an average slip for the whole fault rupture derived from the above assumptions is equal to the average slip as estimated from teleseismic data.

5.2.2 Computation of the average slip for the entire fault rupture

Assuming that all the patches have same width $W = \alpha L$

the seismic moment associated with the rupture of the ith patch is:

$$M_i = \mu \alpha \ell_i \overline{\Delta U}_i L$$

where $\overline{\Delta U}_i$ is the average slip on patch i. The total seismic moment associated with the entire rupture is:

$$M = \sum_{i=1}^{n} M_i = \alpha \mu L \sum_{i=1}^{n} \ell_i \overline{\Delta U}_i \qquad (5.6)$$

On the other hand, the total seismic moment can be expressed in terms of the total rupture area ($\sum_{i=1}^{n} \alpha L \ell_i$) and the average slip $\overline{\Delta U}$, as:

$$M = \mu A \overline{\Delta U} = \mu \overline{\Delta U} \sum_{i=1}^{n} \alpha \ell_i L \qquad (5.7)$$

Thus equating (6) and (7) gives $\overline{\Delta U}$:

$$\overline{\Delta U} = \frac{\sum_{i=1}^{n} \overline{\Delta U}_i \ell_i}{\sum_{i=1}^{n} \ell_i} \qquad (5.8)$$

The theoretical shape of the slip function for a given patch can be taken as an ellipse (ref. Das & Aki) so that:

$$\overline{\Delta U}_i = \frac{2}{\pi} (\Delta U_{max})_i \qquad (5.8')$$

where $(\Delta U_{max})_i$ is the maximum slip, reached at the middle of patch i. Then, using Eq. (5.1) together with above gives:

$$\overline{\Delta U} = \frac{2a}{\pi} \frac{\sum_{i=1}^{n} \ell_i^2}{\sum_{i=1}^{n} \ell_i} = \frac{2a}{\pi} g(\underset{\sim}{\ell}) \tag{5.9a}$$

where $\underset{\sim}{\ell}$ is the vector $(\ell_1, \ell_2, \ldots, \ell_n)$.

The value of $\overline{\Delta U}$ can be viewed as one realization of the random variable--average slip on the fault--for a given value $\underset{\sim}{\ell}$ of the random vector $\underset{\sim}{L}'$. This is expressed by

$$r \cdot v\ \overline{\Delta U} = \frac{2\pi}{a} g(\underset{\sim}{L}') \tag{5.9b}$$

The expected value of the random variable $\overline{\Delta U}$ can be approximated by a Taylor series expansion limited to the second moment, as follows:

$$E[\overline{\Delta U}] = g(\underset{\sim}{L}')\Big|_{L'=\overline{\ell}} + \frac{1}{2} \sum_{i=1}^{n} \frac{\partial^2 g}{\partial L_i'^2}\Big|_{L_i'=\ell} \mathrm{Var}(L_i') \tag{5.10}$$

$$+ \frac{1}{2} \sum_{i=1}^{n} \sum_{j=1}^{n} \frac{\partial^2 g}{\partial L_i' \partial L_j'}\Big|_{L_i'=L_j'=} \mathrm{Cov}(L_i', L_j')$$

where $\underset{\sim}{L}'$ is the random vector $(L_1', L_2', \ldots, L_n')$ whose mean is $\overline{\underset{\sim}{\ell}} = (\overline{\ell}, \overline{\ell}, \ldots, \overline{\ell})$ because the L_i''s are i.i.d with mean $\overline{\ell}$.

Using the Eqs. (5.3), (5.4) and (5.5) gives the expected value of the mean slip

$$E[\overline{\Delta U}] = \frac{2a}{\pi} \bar{\ell} \frac{2n}{n+1} = \frac{4aL}{\pi(n+1)} \tag{5.11}$$

When the coefficient a is known we can assume that the expected mean slip $E[\overline{\Delta U}]$ is estimated by the observed value (calculated from teleseismic data). If a is not known we need another observation such as the largest slip observed on the fault, and we can use Eq. (5.11) together with Eq. (5.13') and solve for a and n. If the largest patch length is known, then we can use the method presented in the next section. In any case, the uncertainty is such that we will try to make use of all available data and choose the values of n and possibly "a" which are the most compatible with Eq. (5.11), (5.13) and (5.13').

5.2.3 Estimation of n and $\bar{\ell}$ from the largest patch length

Assuming that the number of patches, n, is large, the correlation between any two patches' lengths becomes small (see Eq. 5.5). Then the patches' lengths can be treated approximately as independent random variables.

Given the total fault length L, and the number of patches n, and approximating the patch's lengths by independent and identically distributed random variables, the cumulative probability function of the largest patch's length, ℓ_{max} is given by the following:

$$P[\ell_{max} \leq \ell] = \prod_{\beta=1}^{n} F_{L_\beta}(\ell) = \left\{1 - \left(1 - \frac{\ell}{L}\right)^{n-1}\right\}^{n} \tag{5.12}$$

where $F_{L'}(\ell)$ is given by Eq. (5.2). (See Fig. 5.2 for $P[\ell_{max} \leq \ell]$ for several n values].

Given that we observed one value of ℓ_{max} on the fault, the problem is to determine what is the most likely value of n which could have generated that value. Three methods are considered.

(i) The observed value is considered to be the most probable realization of ℓ_{max}. Then the observed value can be equated to the mode of the distribution of ℓ_{max}. This is expressed in Eq. (5.13) by setting $\frac{d^2P[\ell_{max} \leq \ell]}{d\ell^2}$ to zero and solving for ℓ_{max},

$$\ell^*_{max} = \text{observed } \ell_{max} = L\left\{1 - \left(\frac{n-2}{n^2-n-1}\right)^{\frac{1}{n-1}}\right\} \tag{5.13}$$

and Eq. (5.13) is solved for n. The corresponding most probable maximum slip is obtained by using Eq. (5.1).

$$\Delta U^*_{max} = a\, \ell^*_{max} \tag{5.13'}$$

(ii) The observed value is equated to the mean of the distribution of ℓ_{max}.

(iii) The parameter n is estimated by a method of maximum likelihood.

The three methods are compared in Appendix A5.1. It is found that the first method (Eq. 5.13) is the most desirable. Furthermore it is possible to get a confidence interval, as is shown in Section 3.2.

5.3 Estimation of the Average Patch Length

5.3.1 Method

The method used to estimate the number of patches (i.e., the average patch length $\bar{\ell}$) depends on the type of data available. For all cases the total length L must be known however.

(1) If the largest patch length along the fault is known, it is assumed that the observed value is a characterization of the most probable value of the largest patch length one could obtain with n patches. Eq. 5.13 (or 5.14) is then solved for n and we obtain an estimate of the most probable average patch length $\bar{\ell} = \frac{L}{n}$.

(2) If the largest value of the patch length is not very well known but the maximum slip ΔU_{max} is known, then we use Equation 5.13'. In that case we need to assume a value for the coefficient a. Concurrently the same value of a is used in Eq. 5.11 together with $\overline{\Delta U}$, obtained from teleseismic data. The values obtained from Eqs. 5.13' and 5.11 are compared and if they don't match, a is changed. By iteration the system Eq. 5.13'-5.11 is solved for $\bar{\ell}$.

This method also gives us a means of estimating the stress drop $\Delta\sigma$ by using a relationship between stress drop and maximum strain as in Aki, 1970, for the case of the San Andreas Fort Tejon Earthquake. In our notation:

$$\Delta\sigma = \frac{7\pi^2}{24} \mu a \qquad (5.14)$$

and by taking $\overline{\Delta U}$ in meters, ℓ in kilometers, $\mu = 3.10^{10}$ Pascals, and $\Delta\sigma$ in bars, the above equation becomes:

$$\Delta\sigma = 550\ a$$

$$a = \frac{\Delta U_{i\,max}}{\ell_i}\ , \text{(Eq. 5.1)} \qquad (5.15)$$

It has been recently found that for certain classes of earthquakes, the value of $\Delta\sigma$ is fairly constant (Papageorgiou, 1981). For the California earthquakes, this value is approximately 300 bars. In those cases when $\Delta\sigma$ can be estimated, we can compute an estimate of a and knowing $\overline{\Delta U}$, we can solve Eq. (5.11) for n. This is exactly what we do when using models of simulation of earthquakes, as explained in Section 5.5 of this paper.

5.3.2 Uncertainty

When using the method 1 described above, it is possible to get a confidence interval for $\bar{\ell}$. The problem that we want to solve here could be stated as follows.

The distribution function of the largest value one could observe on a fault rupturing into n segments can be computed. As an example we plotted several of those functions for n = 2, 4, 10, 20 and 30 on Fig. 5.2. It can be seen on that figure that the knowledge of one value of the largest patch length, i.e., the observed ℓ_{max}, is not sufficient to give a reliable estimate of n. (However as n increases we can show that, see Appendix 5.1, the standard deviation decreases very fast so that the most probable value becomes a better estimate). The question that we can ask then is, given the observed value ℓ_{max} what is the value of n for which there is a certain probability, say P, that ℓ_{max} be smaller (i.e., P = .8, .9, .95, etc.).

In other words, given a value of the largest ℓ, ℓ_{max}, to which corresponds to the most probable n, say n_0, there is a finite likelihood that ℓ_{max} may have been generated by a distribution with lower n or higher n.

Let n_1 be such that $n_1 < n_0$ and such that there is a probability P that the random variable "largest ℓ" produced by the distribution with parameter n_1 be smaller than ℓ_{max}; that is

$$P[N \leq n_1 | \ell_{max}] = P = F_{L|n_1}(\ell|n_1) = \left\{1 - (1-\ell_{max})^{n_1-1}\right\}^{n_1} \qquad (5.17)$$

Similarly define $n_2 > n_0$ such that:

$$P[N \geq n_2 | \ell_{max}] = P = F_{L|n_2}(\ell_{max}|n_2) = 1 - \left[1 - (1-\ell_{max})^{n_2-1}\right]^{n_2} \qquad (5.17')$$

Then we obtain a P probability of the number of patches to be smaller than n_2 and bigger than n_1.

$$n_1 \lesssim n_0 \lesssim n_2 \rightarrow L/n_2 \lesssim \bar{\ell} \lesssim L/n_1 \tag{5.18}$$

5.4 Application

The above methods are applied to a set of seven earthquakes, the results of which are presented in Table 5.1. Some comparisons are made with current available estimates.

(1) San Andreas 1857

On the one hand this earthquake has been very well documented and a recent study by Sieh, 1978, gives us a very detailed knowledge of the slip history associated with it. On the other hand we don't have any instrumental measurement of the characteristics of the earthquake as we would nowadays. Nevertheless it is possible to estimate the maximum slip from historical records, (Aki, 1979) at about 11m and the largest patch's length possibly at 23km (Wallace, 1968, 1973). The total length of the fault rupture may also be estimated from Sieh, 1978, at between 360 to 400km. For our purpose we choose an average value of 380km. The 85% confidence interval on the number of patches and the average patch length then come out to be:

$$55 \lesssim n \lesssim 104 \qquad \text{and} \qquad 3.6 \lesssim \bar{\ell} \lesssim 6.9 \text{ km}$$

the most probable value of n being 69 with the corresponding average patch length $\bar{\ell}$ = 5.5km.

TABLE 5.1

Earthquake	$\overline{\Delta U}$ (m)	L (km)	ℓ_{max} (observed) (km)	ΔU_{max} (observed) (m)	$\overline{\ell}$ (km)	$\overline{\ell}$ observed /or others (km)	$\Delta\sigma$ (bars)
San Andreas, 1857		380	23	11	(3.6)-5.5-(6.9)	5.5	
San Fernando							
Lower	2.1	13		2.4		/3.5-5	105
Upper	2.4	5		5	2.5		550
Parkfield		36	4.5		(.8)-1.4-(2)	1.7	
Dasht-e-bayaz, 1968		39	8		(1.7)-3.1-(5.2)	3.5/7	
Nobi, 1891		80	8		(6.4)-12.7-(26.8)	/14	
Tango, 1927		35	3.5	3	2.1	/3	470
Saitama, 1968	.92	10	1.4		.9-3.5	/3.5	340

A recent study by Aki, et al, 1980, gives an average barrier interval of 8km. Sieh, 1978, gives a detailed slip history of the fault. The scale of his Fig. 5 for the slip unfortunately does not show that the slip may have been very small in between the points of measurements. If one assumes that the slip drops to zero, between each cluster of measurements, one can identify the number of patches, and compute the average patch length for the 1857 earthquake. This assumption is equivalent to saying that the measurements were made where the slip was noticeable, that is, close to the middle of each patch. Based on a subjective count of the clusters we find 47 of them for a length of approximately 260km, the average patch length is therefore 260/47 = 5.5km. This may be a coincidence but it is at least consistent with our result!

(2) San Fernando

This earthquake has been the subject of very detailed studies by many authors. All of them agree on the biplanar shape of the rupture fault. In our study we use the data from Heaton, 1978.

The lower part of the earthquake has different characteristics from the upper part. The former is assumed to have propagated within the lower plane, then started in the upper plane but stopped soon, as shown in Fig. 5.3. The latter part consisted mainly of the rest of the upper plane. The parameters associated with each part are chosen as:

	Lower part	Upper part
M_0	$.8\ 10^{19}$ m.N	$.6\ 10^{19}$ m.N
Area	190 km^2	84 km^2
ΔU_{max}	2.4 m	5 m
Length	13 km	5 km
$\overline{\Delta U}$	2.1 m	2.4 m

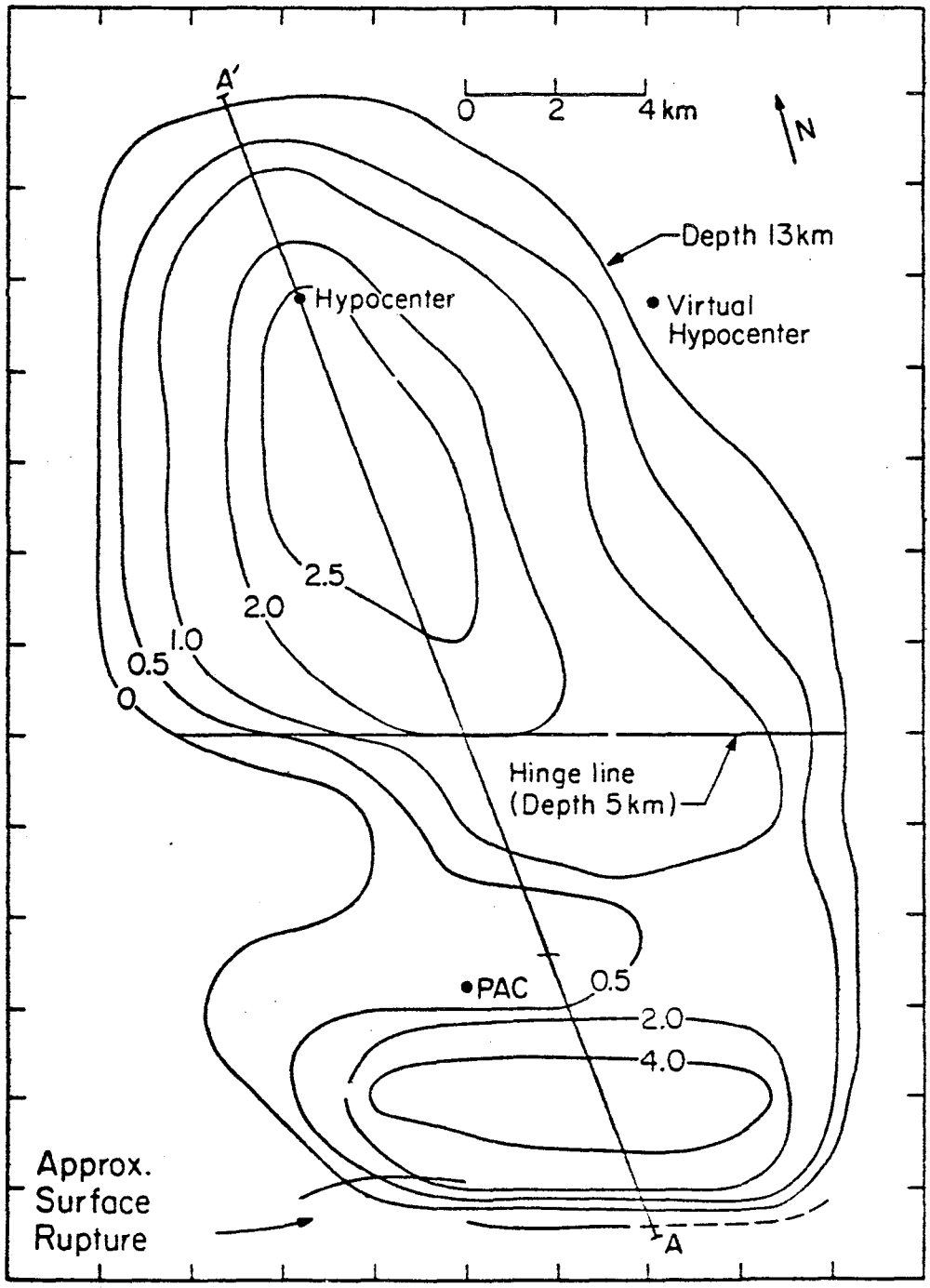

Figure 5.3 Contour map of the assumed fault displacements for the model Norma 163.

where the areas and lengths have been estimated from Fig. 3 of Heaton's paper and $\overline{\Delta U}$ was calculated by $\overline{\Delta U} = M_0/(\mu \cdot \text{Area})$, (where $\mu = 310^{10}$Pa).

For the lower part of the fault our method breaks down, indicating that n has to be less than 2. From this analysis, we have to conclude that the rupture was a massive continuous one. This also means that $\overline{\ell}$ was fairly large. To be consistent with application of the method we would find here $\overline{\ell} = L$, since $n = 1$, and $a = \frac{\Delta \overline{U}_{ma}}{L} = .19$. The stress drop computed with Eq. 5.15 would then be 105 bars.

For the upper part of the rupture, using Eq. 5.11 for the value of n which gives $\Delta U_{max} = 5$m (see Fig. 5.4) leads to $n = 2$ and $\overline{\ell} = 2.5$km. Our evaluation of the stress drop is then $\Delta\sigma \simeq 550$ bars.

After a process of trial and error, Shakal, 1979, derived his best model of source, as shown by his Fig. 5.5, which implied also a high stress drop of 600 bars.

(3) Parkfield

Eaton et al, 1970, gave a mapping of the aftershocks of the Parkfield earthquake, Fig.5.6. Aki, 1979, interpreted the region with no aftershocks as the regions of the major shock ruptures. It appears to us then that the largest single convex shape which can be isolated is of approximately 4 to 5km and we will choose $\ell_{max} = 5.4$km. The total length of this rupture is 36km (Fig. 6), so that from Eq. 5.13 the most probable number of patches is $n = 26$ and the corresponding average patch length is $\overline{\ell} = 1.4$km. The 85% confidence interval on the number of patches, and the corresponding average patch length then are:

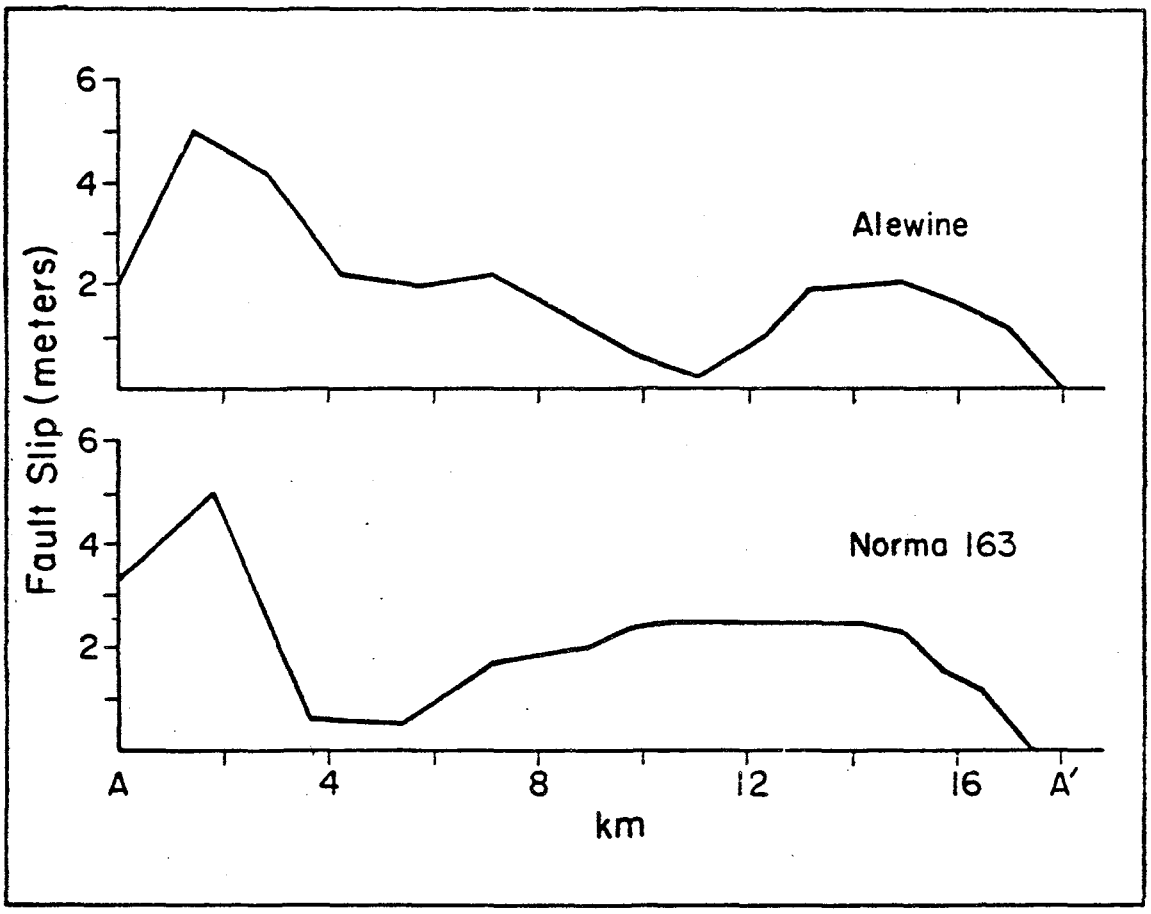

Figure 5.4 Comparison of the fault slip as a function of distance along the line AA' of Figure 4.30. Alewine's (1974) model is from an inversion of static vertical uplift data. Notice that both the static offsets and this study seem to indicate massive faulting very near the free surface (from Heaton, 1978).

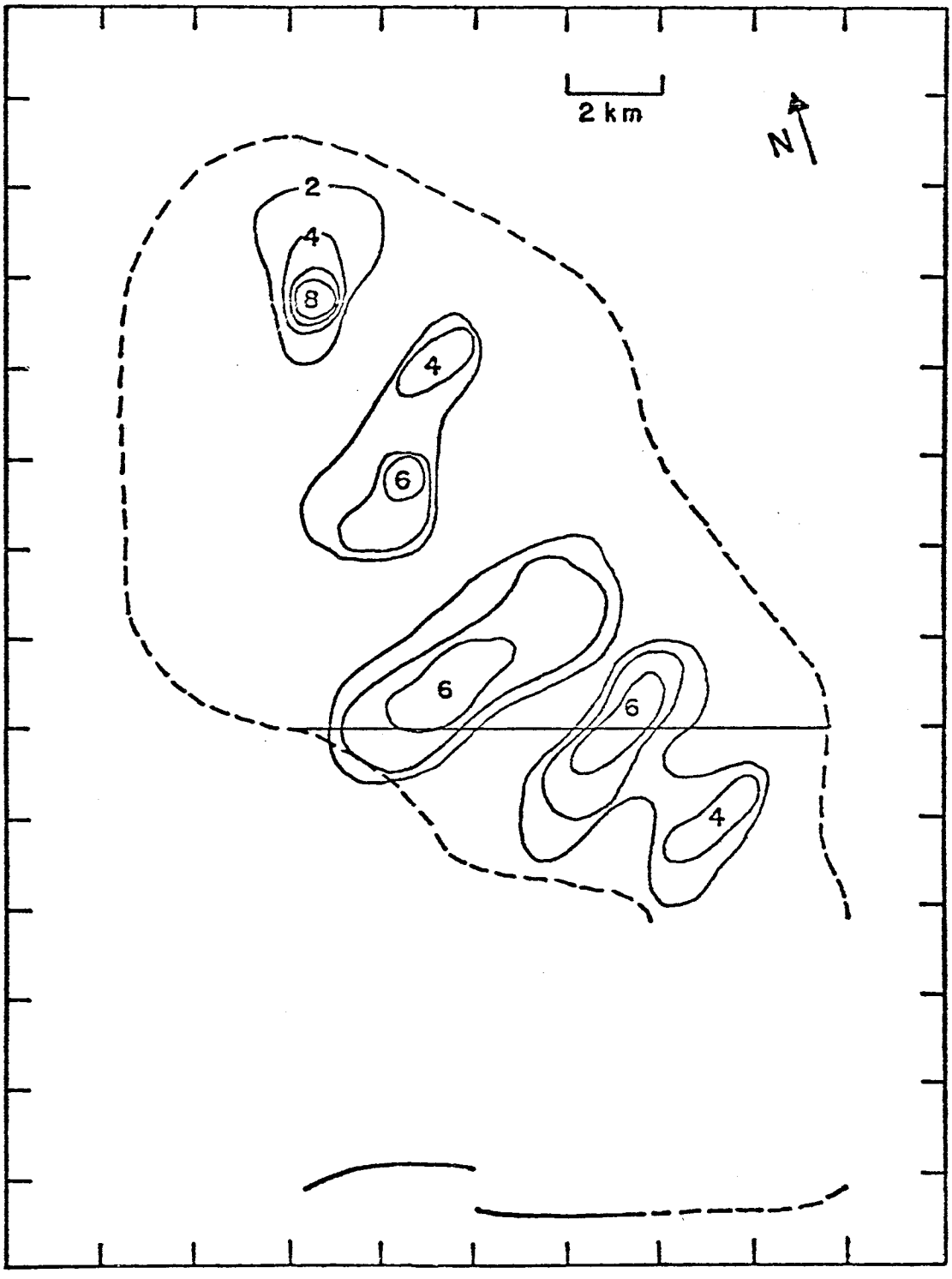

Figure 5.5 (Shakal, 1979) Final model of fault rupture for San Fernando.

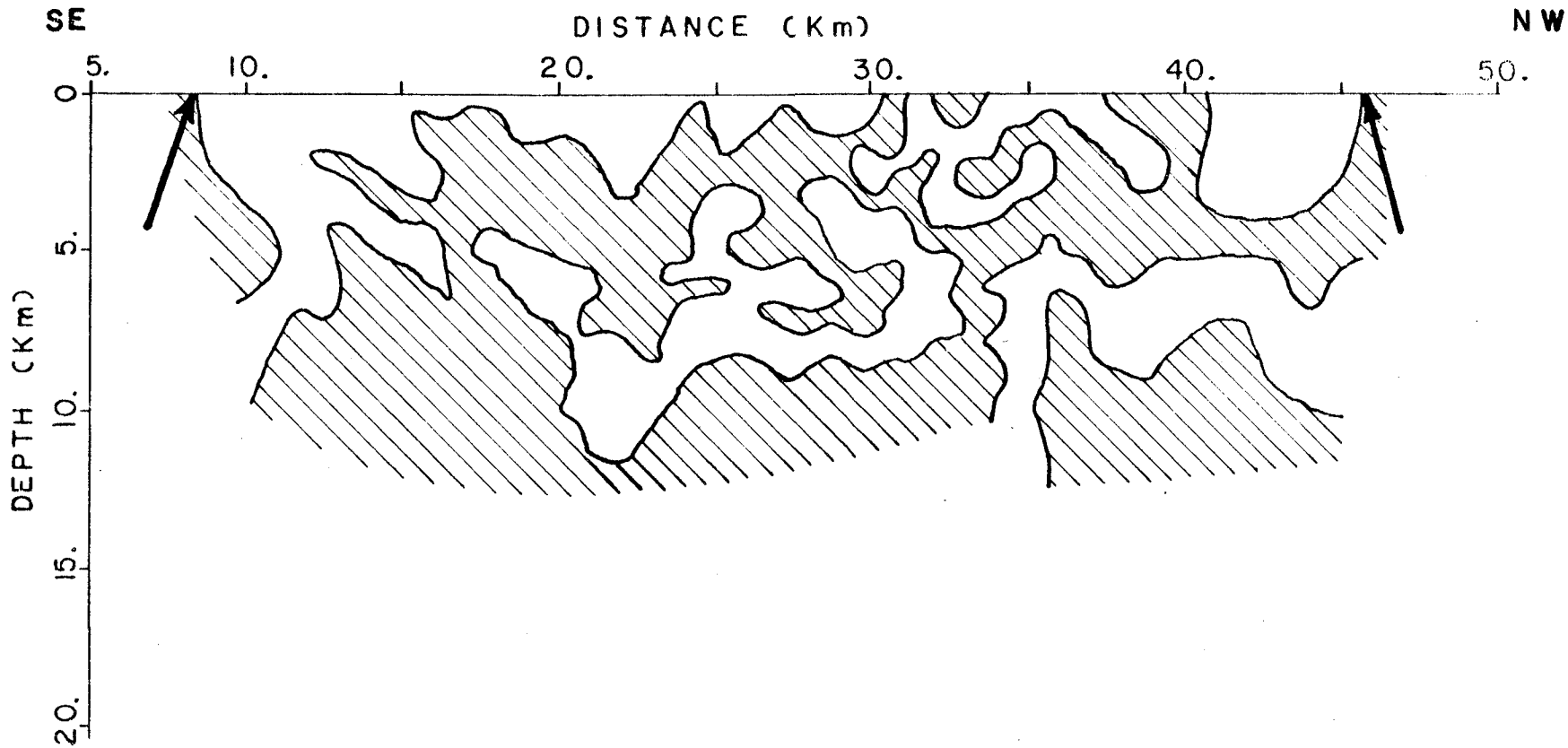

Figure 5.6 The projection of the hypocenters of the Parkfield Aftershocks on the vertical fault plane fall in the shaded area. The hypothetical boundary of this area was sketched by Aki, 1980. The remaining unshaded area is assumed to be the zone of rupture of the main shock which fractured the fault between the two arrows shown in the figure. (The data for this figure was taken from Eaton, et. al., 1970).

$$18 \lesssim n \lesssim 43 \qquad \text{and} \qquad .8 \lesssim \bar{\ell} \lesssim 2 \text{ km}$$

Again, as when we tried to estimate the average patch length from data in the San Andreas case, we are here confronted with a scaling problem. Nevertheless if we try to fit circles of .5km to 5km in the blank parts in Fig. 5.6, we roughly obtain 45 patches for a cumulative length of roughly 80km. The average patch length is therefore approximately 80/45 = 1.7km, which is consistent with our values.

(4) Dasht-e-Bayaz, 1968

Tchalenko & Berberian, 1975, gave the slip distribution along the fault, Fig. 5.7, from which we can infer the maximum patches length ℓ_{max} = 8km, for a total length of 39km. The most probable number of patches is then 12 and the corresponding average patch length is 3.1km.

The 85% confidence interval is $7.5 \lesssim n \lesssim 23$ and the corresponding one on the average length is $1.7 \lesssim \bar{\ell} \lesssim 5.2$km. By comparison we find 10-11 patches, therefore the average patch length is $\bar{\ell}$ = 39/11 = 3.5km, which is in good agreement with our value. Aki, 1980, however, found a quite different value of 7km for his barrier interval.

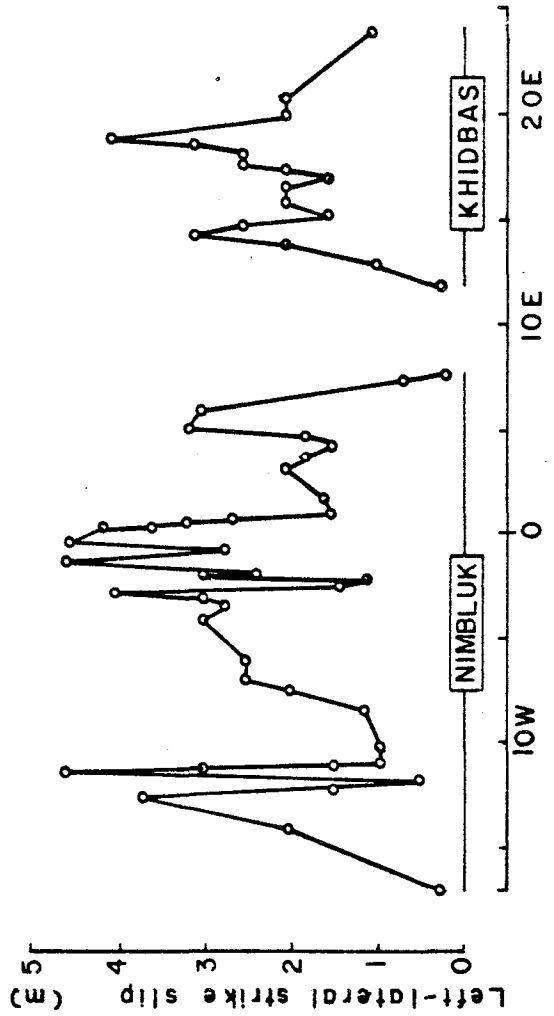

Figure 5.7 Slip distribution along the fault of the Dasht-e-Bayaz earthquake (after Tchalenko and Berberiom, 1975).

(5) Nobi, (Mino-Owari), Japan, 1891

The surface faulting was about 80km long (Fig. 5.8) and the maximum displacement was 8m of left slip, (Bonilla, 1979). The surface ruptures consist of several segments that are locally en echelon to the general trend. We assume here that the patches are limited in size by sudden changes in direction of the fault trace, therefore the largest patch length one can identify here is approximately 25km.

Using Eq. 5.13, we obtain the most probable number of patches n = 6.3 and corresponding average patch's length $\bar{\ell}$ = 12.7km. Then the minimum and maximum n values determined with 85% confidence are 3 and 12.5 giving the corresponding bounds for $\bar{\ell}$.

$$6.4 < \bar{\ell} < 26.8$$

$$\text{most probable } \bar{\ell} = 12.7\text{km}$$

The most probable value is comparable with the 14km average barrier interval found by Aki (1980).

(6) Tango, Japan 1927

The Tango, Japan faulting of 1927 comprised two surface faultings, the Gomura fault trending north-northwest and the Yamada fault trending northeast (Fig. 5.9). We are restricting our attention to the Gomura fault where the maximum observed slip is 3m and the largest observed patch is 3.5km, (Bonilla, 1979).

These values cannot, however, be used in Eq. 5.13 since there could be higher values for the portion of the fault under the sea. The parameter a = 3/3.5 can, however, be used together with the total length L = 35km

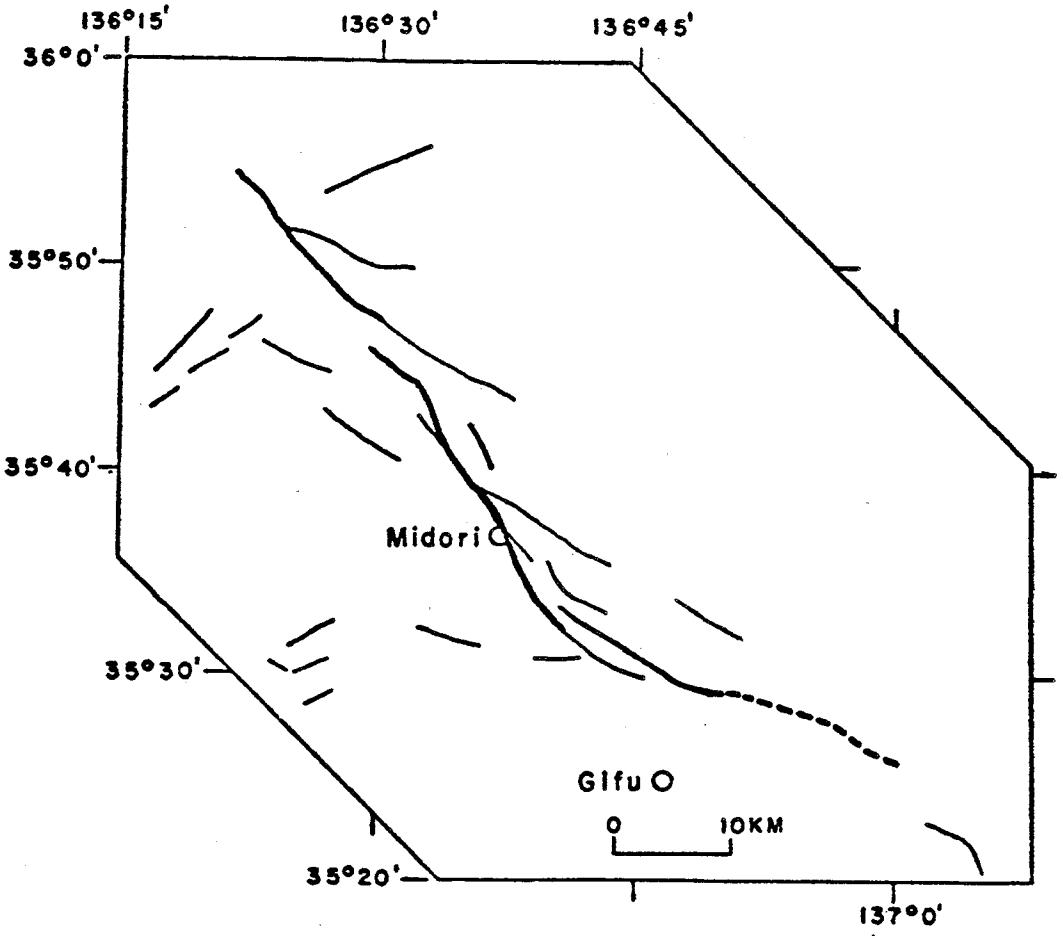

Figure 5.8 Map of Nobi, Japan, fault area. Strike slip surface faulting of 1891 is shown (generalized) by heavy line; other faults with Quaternary displacements shown by light lines (from Matsuda, 1974).

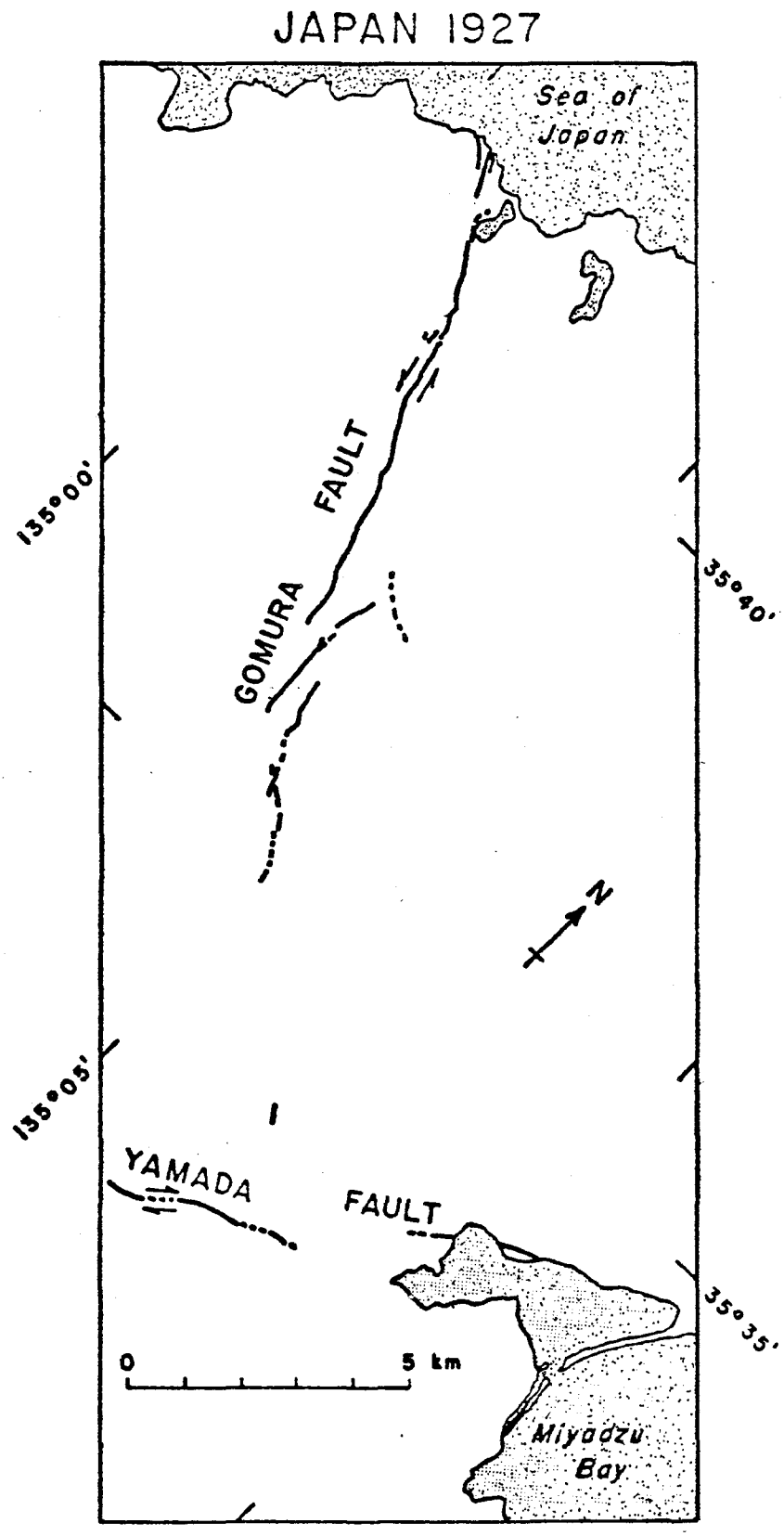

Figure 5.9 Surface faulting associated with the Tango, Japan, earthquake of 1927. From Yamasaki and Tada, 1928.

and the average slip $\overline{\Delta U}$ = 3m determined by Geller, 1976. This value of 35km should be allocated to the entire earthquake, including both portions Gomura & Yamada, but if we assume that the congregate fault (Yamada) contributed much less to the seismic moment, we can neglect it and consider that the length and average slip apply to the principal fault. Then assuming that the value of a = 3/3.5 is representative of the whole fault, including the submerged part, and applying Eq. 5.11 we find $n \cong 12$ segments, and an average patch length of $\overline{\ell} \cong$ 3km (exactly n = 11.7, $\overline{\ell}$ = 3km). The corresponding probable largest length is 7.4km and most probable largest slip is 6.4m. These values are much higher than the observed values, but one could argue that under our assumptions a large part of the fault would be under water and the observed values may not be the absolute maximum for the fault. It is interesting to note that Aki, 1980, found a barrier interval of 3km for this event. The stress drop computed from the above values is $\Delta\sigma$ = 470 bars.

(7) Saitama 1968

Geller, 1976, provides us with the average slip $\overline{\Delta U}$ = .92m and the total length L = 10km. The maximum observed slip is 1.4m (Aki, 1980). The parameters compatible with Eq. 5.11 then are obtained as $\overline{\ell}$ = 3km and a = .31, thus implying a stress drop in the range of 170 bars.

By comparison, Aki, 1980, assumed a 3.5km barrier interval, which is in agreement with our result.

5.5 Choice of $\bar{\ell}$ in the Simulation Model

The choice of the average size of the patches, $\bar{\ell}$, is directly related to the choice of a stress drop. For some isolated cases of particular earthquakes it is possible to obtain directly $\bar{\ell}$ from data. However the type of model considered here is not designed for simulation of specific earthquakes; rather it is used for generation of large samples of hypothetical events which may have only their statistical characteristics in common with actual earthquakes. This model which is intended to be used in risk analysis studies may in some cases be used to predict the risk inherent in a region where few or no earthquake history is known. From geological considerations it may be possible however to assume some value for the stress drop. For instance, one can set the stress drop to some value for all earthquakes occurring intra plate, and another value for inter plate earthquakes when no better information is available.

If we assume a value for the stress drop, the parameter a can then be computed from Eq. 5.15. The seismic moment and dimensions of the rupture is known in the simulation so that the average slip is easily computed by,

$$\overline{\Delta U} = \frac{M_0}{\mu L W} \tag{5.19}$$

and the average patch length, or coherent length, to be used in the model is computed by solving Eq. 5.11.

For example, let us choose three hypothetical events with the following parameters:

event 1: $M_0 = 2\ 10^{17}$ mN

$L = 6$ km , $\overline{\Delta U} = .37$ m

2: $M_0 = 63\ 10^{17}$ mN

$L = 19$ km , $\overline{\Delta U} = 1.17$ m

3: $M_0 = 2\ 10^{20}$ mN

$L = 60$ km , $\overline{\Delta U} = 3.7$ m

If we further assume the stress drop to be in the range 150 to 250 bars, (Papageorgiou, 1981) the corresponding ranges of average coherence length are:

event 1: $\overline{\ell} = .7$ to 1.3 km

2: $\overline{\ell} = 2.2$ to 4.1 km

3: $\overline{\ell} = 7.0$ to 13 km

VI. CHARACTERISTICS OF THE MODEL AND APPLICATIONS

6.1 General

The general characteristics of this model of strong ground motion may be identified as belonging to two classes. Firstly, the ones which are the results of physical and mathematical assumptions and simplifications, and secondly, the ones which depend more strongly on the range of values of the parameters to be used in the simulations. In Chapters II and III the physical and mathematical assumptions were described and their theoretical effect on the results analyzed in detail. In this chapter we describe the second class of characteristics by the means of a parametric study. The different uses of the model in engineering and research applications are only mentioned as an introduction to a forthcoming report on the matter.

6.2 Parametric Study

6.2.1 Shear Wave, Quality Factor, Velocity of Rupture Propagation

The results summarized in this section are taken from a previous study (Savy, 1978). A sensitivity analysis was performed to study the effect of the shear wave velocity (β), the quality factor (Q) and the velocity of propagation (V_r) on the time histories and the frequency content of the acceleration record. In that study the model was a far field model of SH waves only. The motion computed in the new improved model has the same functional dependence, however, regarding the above parameters. As a consequence the above mentioned sensitivity study applies equally to the new model for those parameters (β, Q, V_R). A summary of

the results of that study is presented in Table 6.1, where the various parameters are as follows:

COLUMN (5) f^* is a statistical characteristic of the motion. It is computed as follows:

$$f^* = \left(\frac{\lambda_2}{\lambda_0}\right)^{1/2} \tag{6.1}$$

$$\lambda = \int_0^{f_{max}} f^i \, PSD(f) df$$

and PSD(f) is the power spectral density for an ensemble of events. (See Section V.3.2, p.94-95, Savy 1978). f^* can be interpreted as the most characteristic frequency.

COLUMN (6) γ_{max} is the peak on the 0% damping response spectrum.

COLUMN (7) γ_{peak} is the peak value read on a single sample of an acceleration time history.

COLUMN (8) α_{acc} is the logarithmic decay of the Fourier Amplitude spectrum of the acceleration (see Boore, 1978, for a description) and,

COLUMN (9) α_{disp} is the logarithmic decay of the Fourier Amplitude spectrum of the displacement (see Boore, 1978).

An increasing shear wave velocity (Cases 2, 3, 4) shifts the energy towards higher frequencies (Col. 5, 8 & 9), but at the same time the total energy transmitted decreases, thus the peak acceleration actually decreases. This somewhat curious result will be studied in more detail with the new model in a further study.

1	2	3	4	5	6	7	8	9
CASE #	ρ (km/s)	Q	V_2/V_1 (km/s/km/s)	f* (H_z)	γ_{max} (spectral) (m/s/s)	γ_{peak} (T/H) (m/s/s)	α_{acc}	α_{disp}
NOMINAL 1	3.2	200	3.2/1.8	7.89	14.8	1.53	2.10	3.05
2	1.8	*	*	5.47	32.8	2.11	1.94	2.97
3	2.6	*	*	7.38	19.1	2.73	1.57	2.78
4	4.5	*	*	8.54	7.4	.80	1.27	2.63
5	*	400	*	8.65	16.4	2.53	.92	2.46
6	*	100	*	4.86	11.8	.81	1.90	2.95
7	*	50	*	2.83	6.8	.35	2.65	3.32
8	*	*	4.4/3.0	8.10	20.2	2.05	2.25	3.12
9	*	*	2.2/1.6	7.95	9.5	.80	1.51	2.75
10	*	*	2.0/0.5	7.74	6.1	.72	1.89	2.94

TABLE 6.1

KEY: * The value used in this case is the nominal value of Case #1.

The cases 5, 6 and 7 indicate clearly, as expected, that decreasing Q values eliminates high frequency content. Finally, in columns 8 to 10 it is seen that a velocity of rupture propagation higher than β can create very high accelerations with an overall high frequency content, but decaying also very fast (Col. 8). Increasingly lower propagation velocity creates increasingly lower peak accelerations.

6.2.2 Behavior of the Solutions for a Single Patch.

Before looking at the effect of the parameters on the solution for an assemblage of patches, a study for a single patch was performed to visualize the effect of size and rise time on the elementary solution. This is important to understand the effect of a single large rupture within an assemblage of smaller patches. For instance one can envision a large rupture area with small patches overall, but with a few much larger patches at some distance from one another. This is actually what happens in the example of rupture propagation given in Chapter 2 (see Fig. 2.4). The Fig. 6.1 is a time history calculated with the rupture scheme of Fig. 2.4. The large isolated peaks correspond to the rupture of the larger patches superimposed on the overall smaller contribution of the other patches. For the single patch analysis we chose a nominal case where the rupture area is $(6 \times 3)km^2$ and the site is 8km at the surface (the fault breaking the surface on its 6km length) on a normal to the middle point of the trace.

First the size of the element was changed with density of seismic moment per unit area kept constant and the rise time kept constant at .25sec (see Table 6.2). The peak acceleration decreased in a non-linear fashion, as seen in Fig. 6.2. The non-linear effect is believed to be due to geometric changes related to location of the extremities of the patch relative to the site. This appears in the variables T_L and T_W of Eq. 3.25. Conversely,

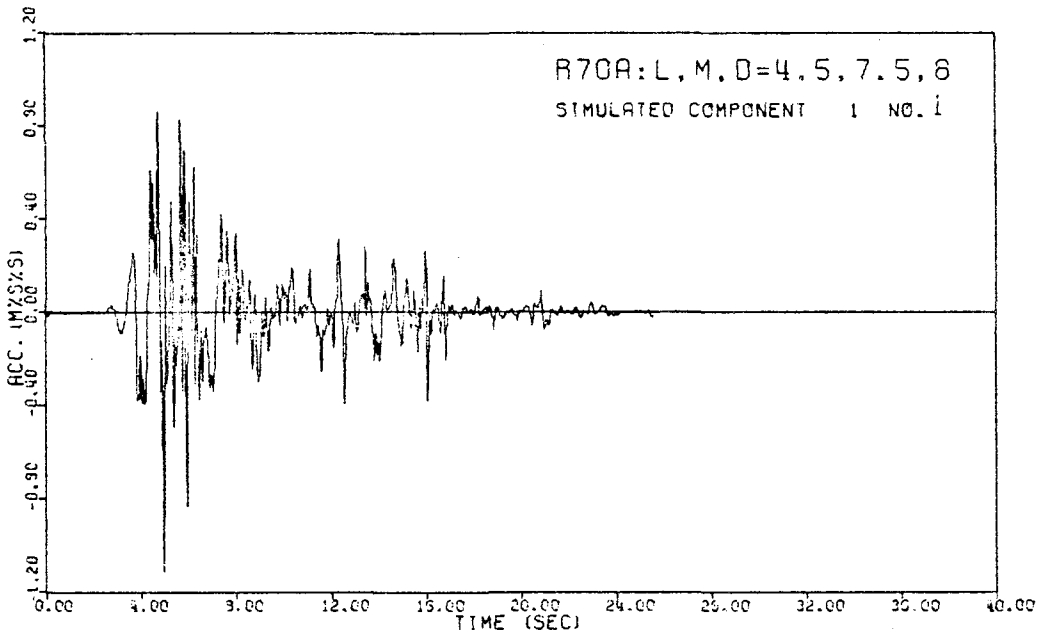

Figure 6.1 Example of acceleration time history obtained from a simulation with large patches ($\bar{\ell}$ = 4.5km).

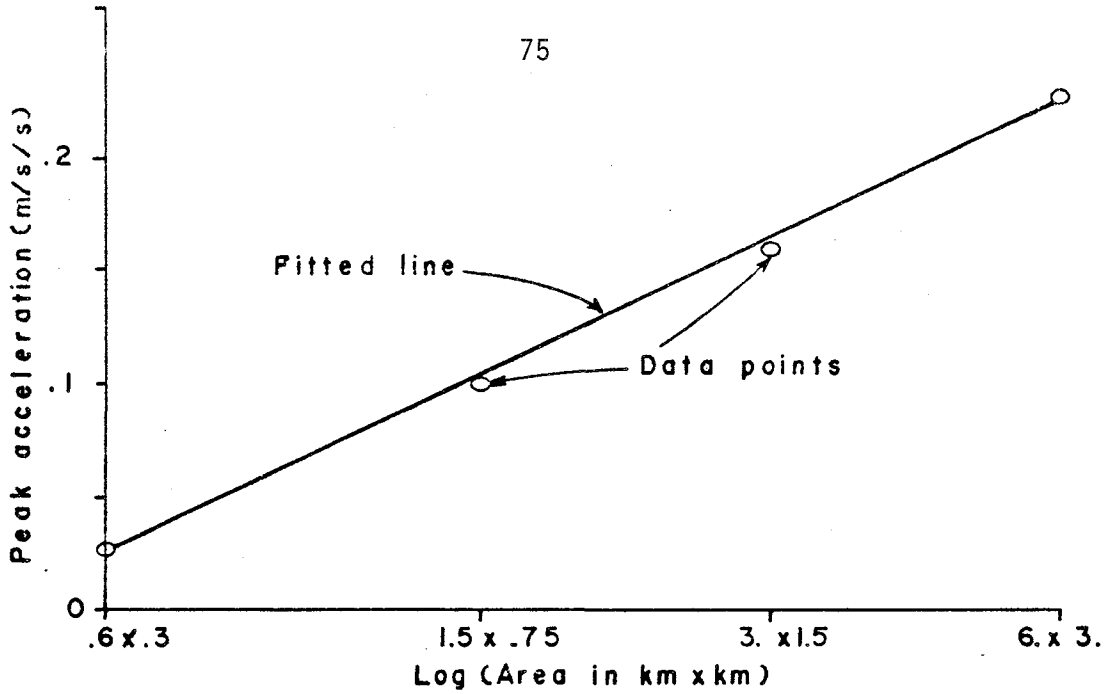

Figure 6.2 Variation of peak acceleration, for a single patch, versus area of the patch.

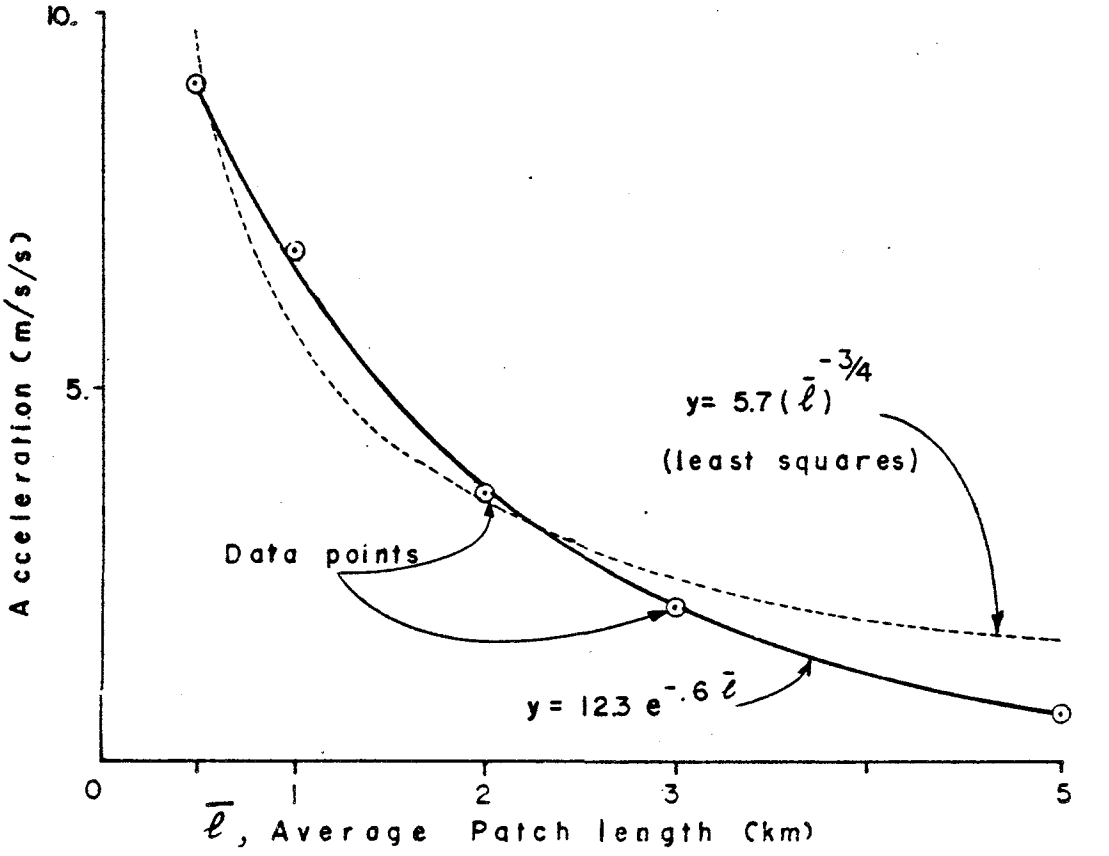

Figure 6.3 Peak acceleration versus average patch's length ($\bar{\ell}$).

if we normalize these results for a constant seismic moment we find that the peak acceleration is roughly inversely proportional to the area of the patch. This can be physically interpreted by saying that areas with higher stress drops will generate higher frequencies and, therefore, higher peak accelerations. In a second set of analyses, the density of seismic moment was kept constant and the rise time was computed by means of an empirical formula (Geller, 1976).

$$\tau = \frac{.4105}{\beta} (L \cdot W)^{1/2} \qquad (6.2)$$

where L and W are the length and width of the patch and β is the shear wave velocity. From Eq. 3.25 it is expected to see a high sensitivity on τ since it directly alters the phasing ($e^{-i\omega \tau/2}$) and the modulus ($\frac{\sin\omega \tau/2}{\omega \tau/2}$), especially in the higher range of frequencies, which set the value of the peak acceleration. This is clearly seen in Table 6.3, especially in the case of constant seismic moment (M_0).

6.2.3 Coherence Length.

This is a governing parameter since it determines the average size of the patches and three of the parameters of Eq. 3.25 which give the phasing and overall modulus of the Fourier Transform (i.e.: T_L, T_W and τ).

The same geometry as previously was selected, that is a total rupture dimensions of 6km by 3km, and the site was at 8km on the normal to the trace. A set of five ensembles of time histories was generated with increasing coherence length ranging from .5km to 5km. Five sample time histories were computed to create each ensemble. For each individual sample a new rupture area discretization and rupture propagation as well as focus location were simulated by Monte Carlo simulation. The place of

TABLE 6.2

AREA KM^2	PEAK ACCELERATION (m/s/s)
6 × 3	.23
3 × 1.5	.16
1.5 × .75	.10
6 × 3	.03

TABLE 6.3

AREA KM^2	RISE TIME τ(sec)	PEAK ACCELERATION (m/s/s)	
		CONSTANT M_0	CONSTANT M_0 DENSITY
6 × 3	.51	.12	.12
3 × 1.5	.26	.60	.15
1.5 × .75	.13	2.56	.16
.6 × .3	.05	19.00	.19

TABLE 6.4

COHERENCE LENGTH ℓ (KM)	PEAK ACCELERATIONS A (m/s/s)					MEAN a (m/s/s)	σ_a (m/s/s)
.5	11.35	11.38	6.05	9.85	6.64	9.05	2.56
1.0	5.59	5.70	13.68	5.76	3.47	6.84	3.94
2.0	3.69	4.13	2.14	5.67	2.34	3.59	1.44
3.0	4.89	1.10	1.51	3.44	.90	2.10	1.69
5.0	.47	.59	.65	.87	.44	.61	.17

focus was set to occur anywhere within the rupture area with equal probability. The mean peak value and its standard deviation were computed. These results are shown in Table 6.4.

In spite of the very small sample size, the mean values seem to vary uniformly. The uncertainty which is attached to them, on the other hand, is very high as shown in Table 6.4. As a first approximation the mean peak acceleration varies in the inverse proportion of $\bar{\ell}$ raised to the power $\frac{3}{4}$, although a negative exponential gives a better fit, as shown on Fig. 6.3. Fig. 6.4 is representative of the changes in the frequency content of the time histories as a function of $\bar{\ell}$, and Fig. 6.5 and 6.6 give the 5 samples for $\bar{\ell}$ = .5 and $\bar{\ell}$ = 1km.

6.2.4 Other Parameters

In addition to the parameters which appear in the Eq. 3.25 some are hidden such as the geometry of the overall system, the orientation of the rupture plane, the direction of the rupture propagation and the location of the rupture initiation (focus). At this point this study has not addressed itself to these parameters, but the influence of the focus location was emphasized in a set of four samples generated from the same discretized fault as in Fig. 2.4, but where only the location of the focus, hence the propagation scheme) vary. As these examples show, in Fig. 6.7, the shape of the envelope of the time history, as well as the peak acceleration values, can be drastically different depending on the location of the focus. In the cases where the focus is in the corner of the rupture surface (Fig. 4.1(d) and (e)) the energy is focused forward in the direction of the site by constructive interferences of the waves. The result is a much higher peak acceleration and a more spiked envelope of acceleration time history than in the other two cases, Fig. 4.1(b) and Fig. 4.1(c).

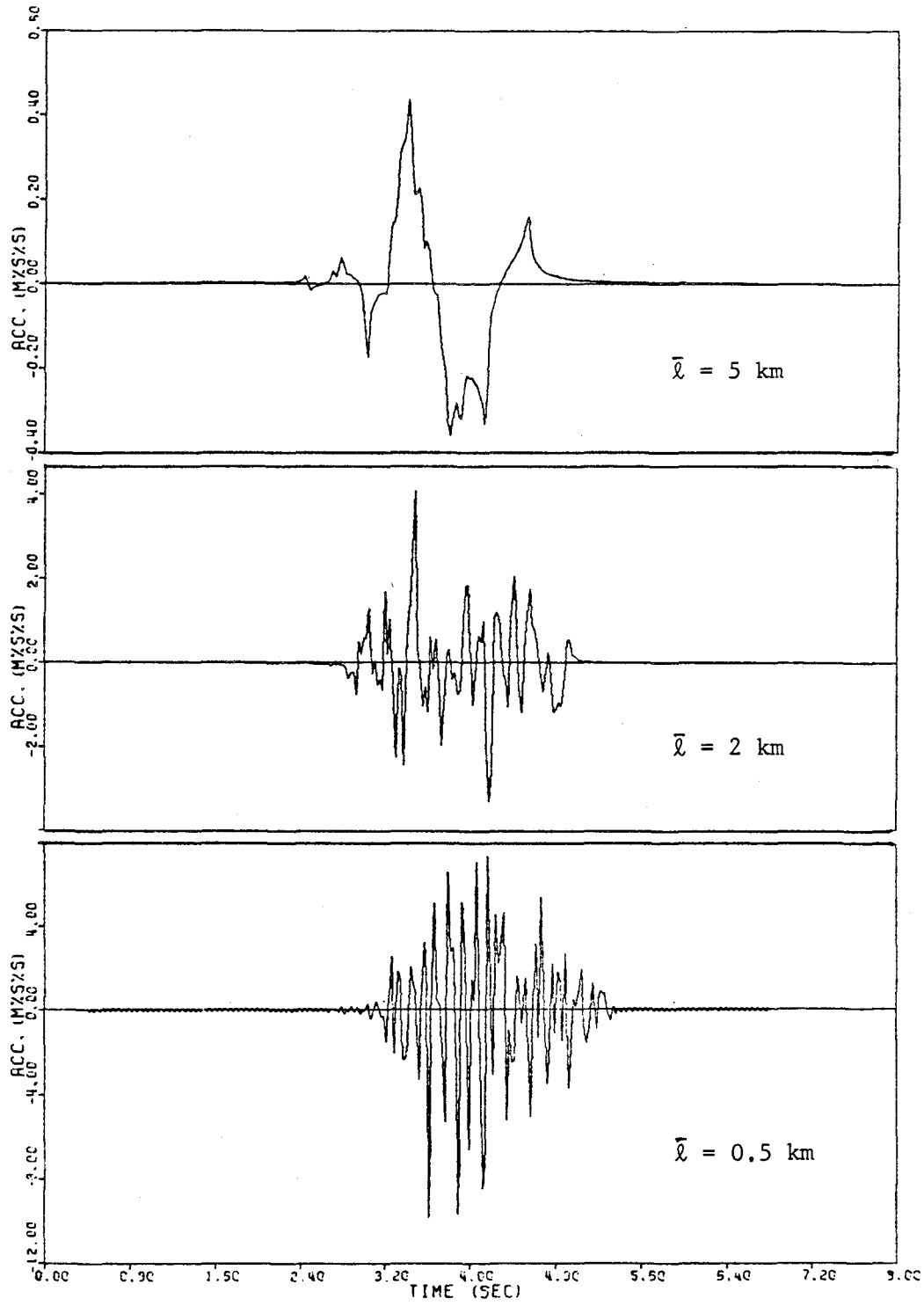

Figure 6.4 Evolution of the record shape with coherence length $\bar{\ell}$.

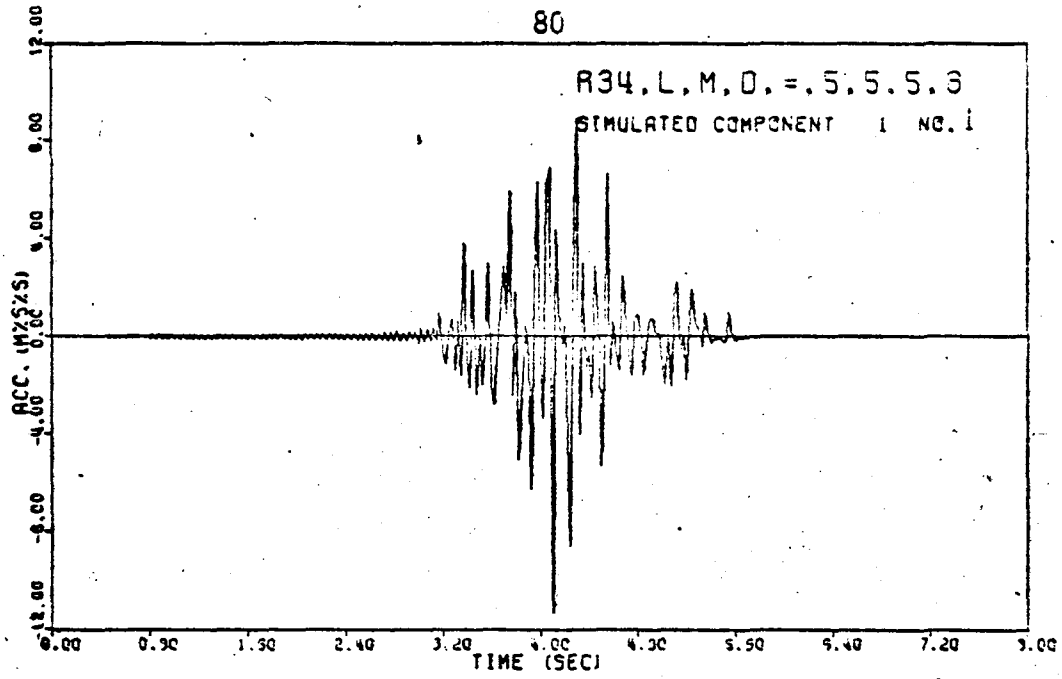
R34,L,M,O,=.5.5.5.3
SIMULATED COMPONENT 1 NO. 1
ACC. (M/S2S)
TIME (SEC)

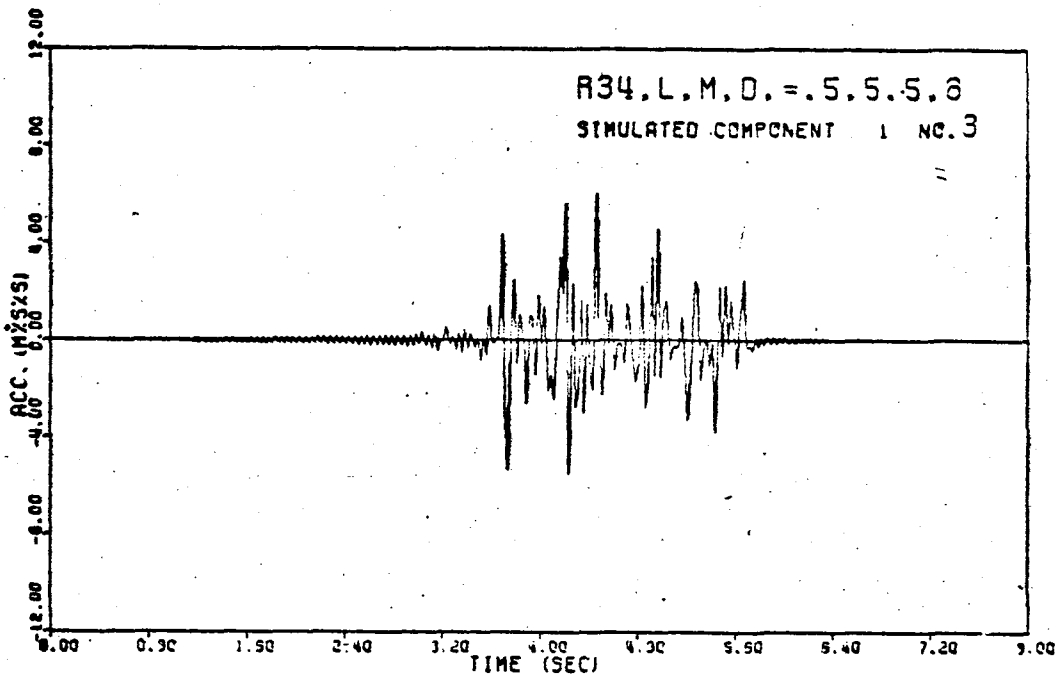
R34,L,M,O,=.5.5.5.8
SIMULATED COMPONENT 1 NO. 3
ACC. (M/S2S)
TIME (SEC)

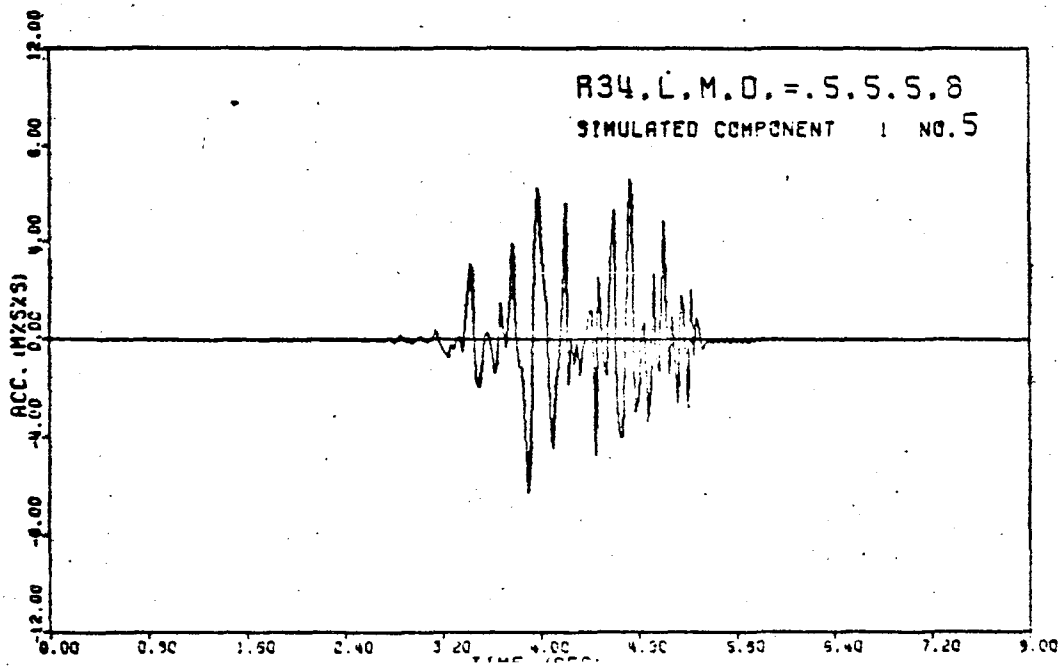
R34,L,M,O,=.5.5.5.8
SIMULATED COMPONENT 1 NO. 5
ACC. (M/S2S)

Figure 6.5

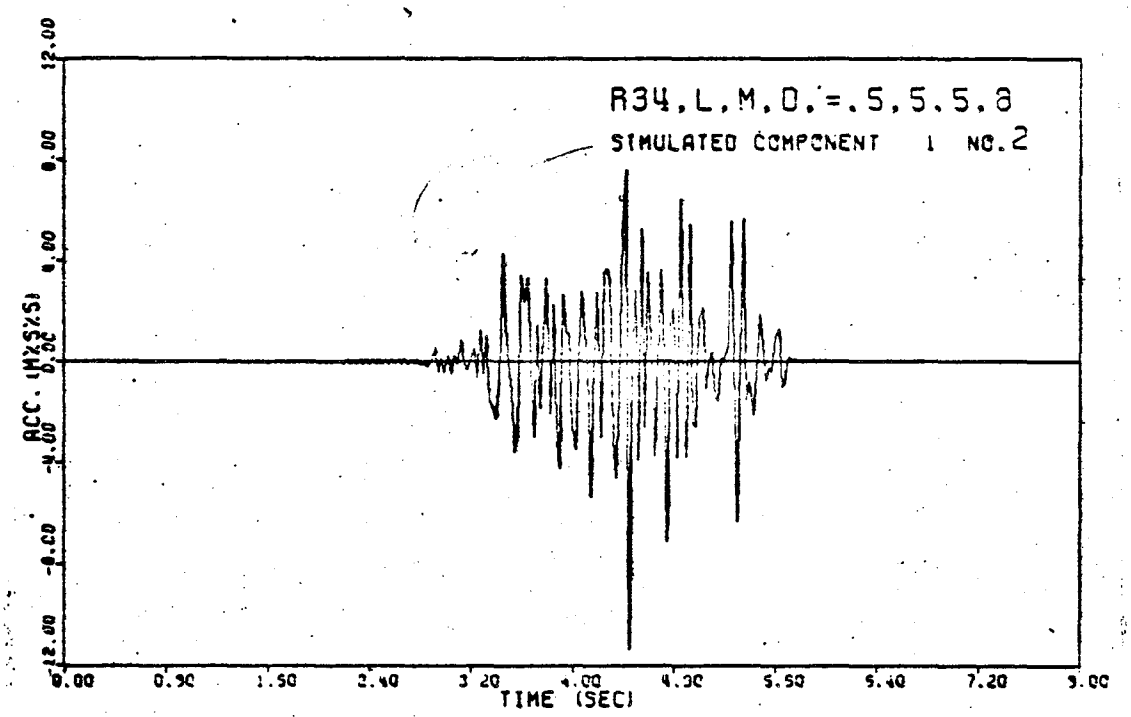

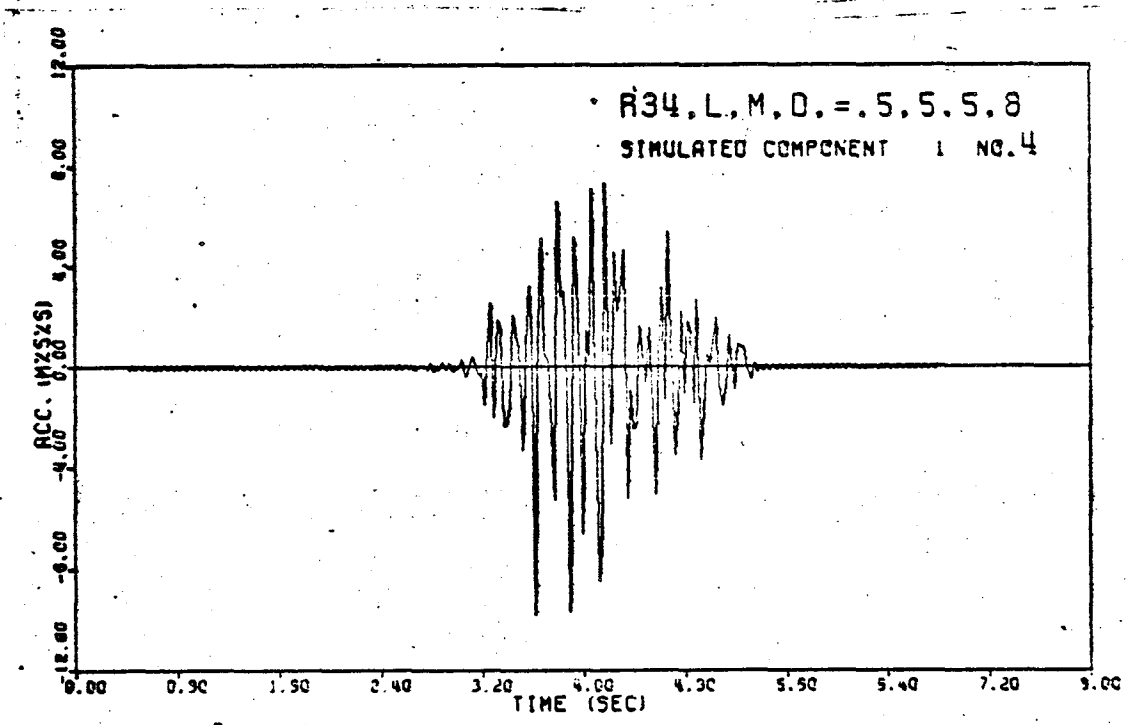

Figure 6.5
(con't.)

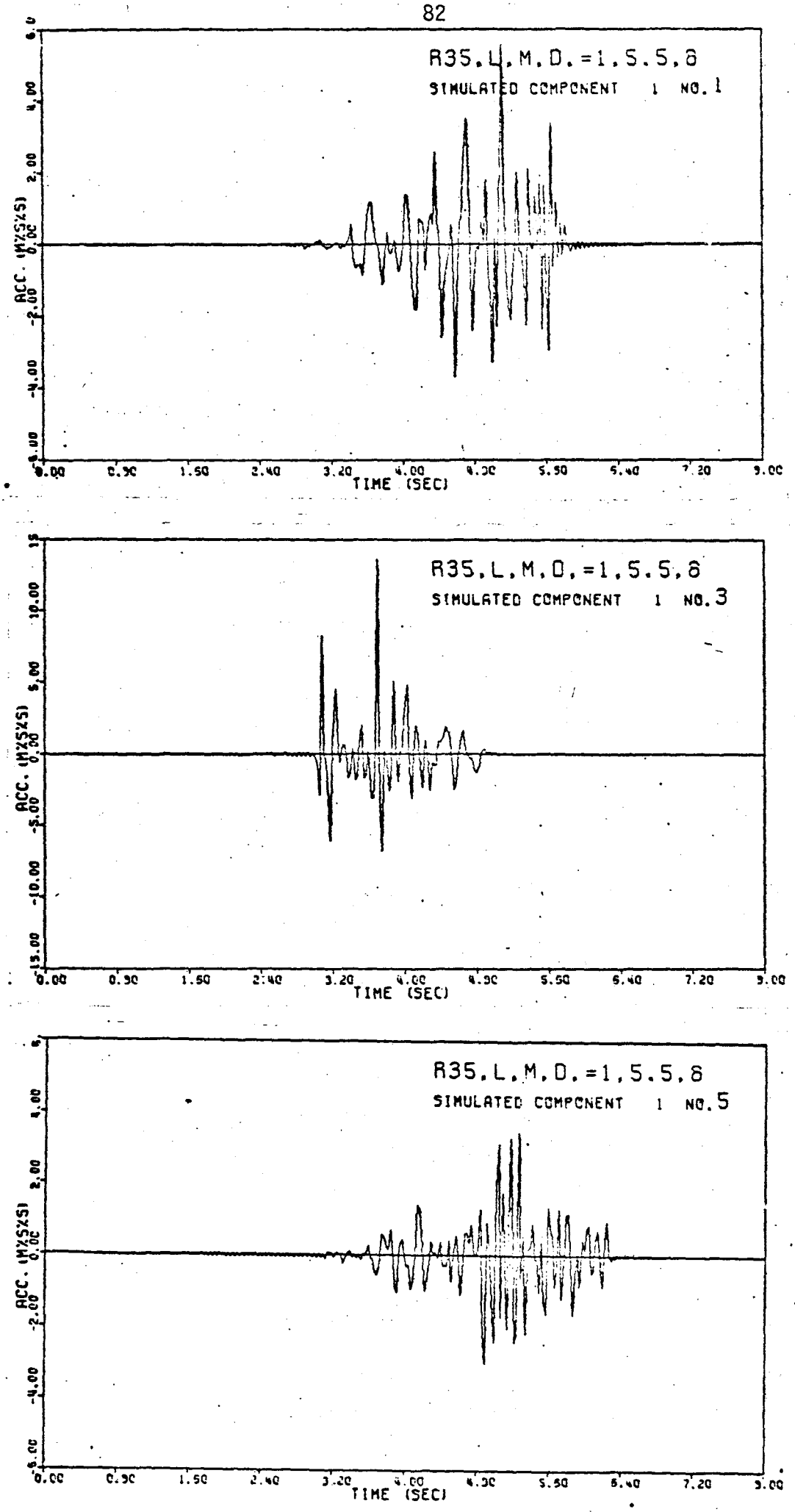
R35,L,M,D,=1,5.5,8
SIMULATED COMPONENT 1 NO.1
ACC. (M/S/S)
TIME (SEC)
R35,L,M,D,=1,5.5,8
SIMULATED COMPONENT 1 NO.3
ACC. (M/S/S)
TIME (SEC)
R35,L,M,D,=1,5.5,8
SIMULATED COMPONENT 1 NO.5
ACC. (M/S/S)
TIME (SEC)

Figure 6.6

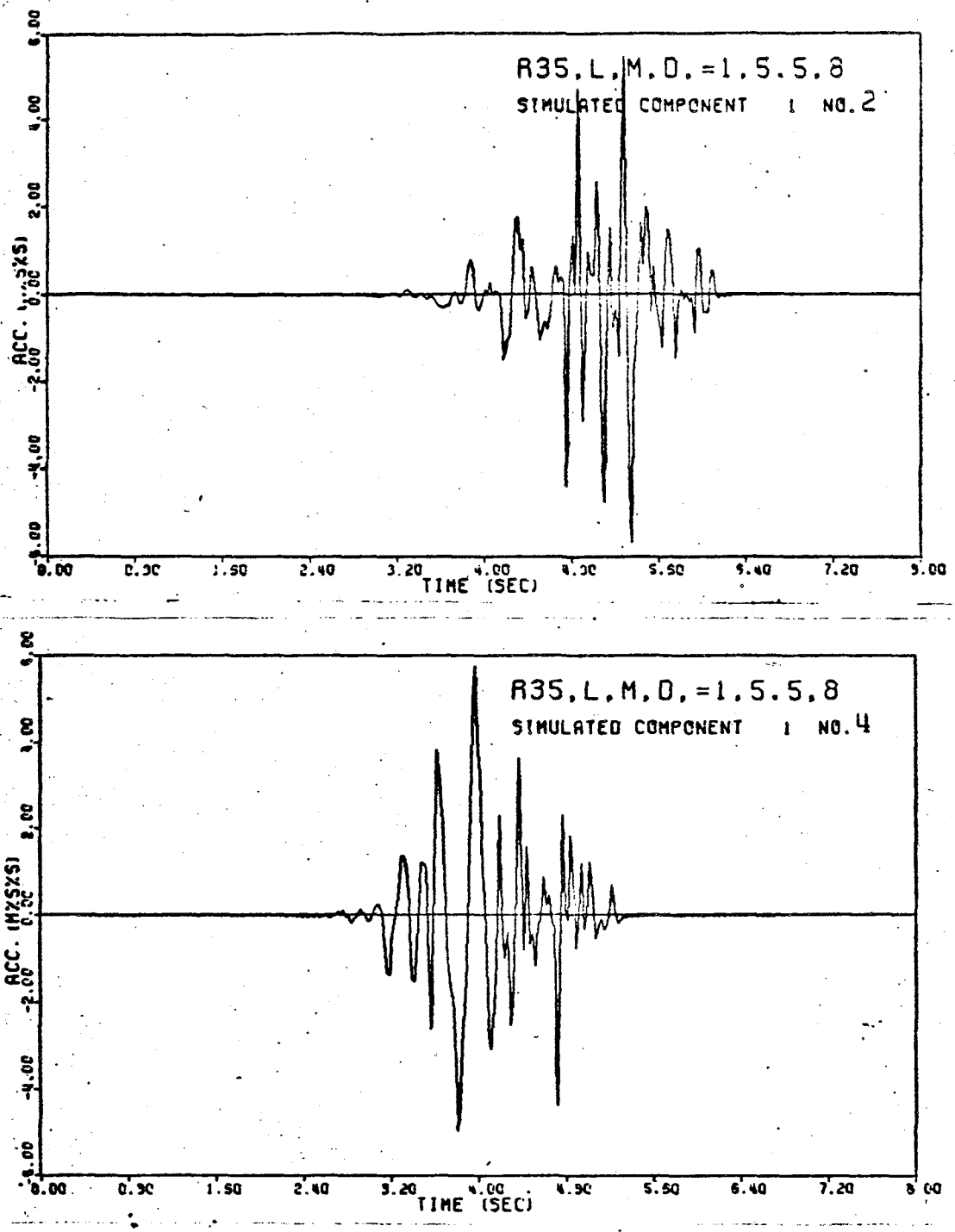

Figure 6.6

(con't.)

6.3 Applications

6.3.1 General

The applications considered at this point evolved from a variety of engineering problems for which classical techniques did not exist or were not satisfactory. Since any physical model of earthquake ground motion used as a generator of records for a particular earthquake would have to be calibrated, most problems considered here deal with qualitative (relative) analyses rather than quantitative.

6.3.2 Functional Form of Attenuation Laws

The very large dispersion in the recorded peak acceleration data has not to date permitted the identification of a complete functional form of the attenuation of peak or RMS accelerations. Using linear and non-linear least square optimization techniques, Askins & Cornell (1979) concluded that there was not statistical evidence, from the data, to adopt one form rather than any other among the "reasonable" contenders. As a result they recommended the simplest form. Since we cannot identify the best functional form yet, from empirical data we turn our attention towards getting artificial data from physical modeling.

The model developed here offers the possibility of studying in detail some of the physical aspects of earthquake record generation and will lead to a better understanding of the phenomenon of attenuation. The most important aspects to be analyzed are:

- Distance effects, with a distinction between the near, intermediate and far fields. Very little data exists in the near field, for instance, but there is ample data in the far field.

- Orientation of the fault. Orientation of the trace, as well as angle of dip of the fault plane.
- Location of the hypocenter.
- Rupture propagation in the rupture plane, including
- Average coherence length of the rupture process.
- Energy level (seismic moment, or magnitude) and,
- Fault dimension (length and width).

Some of the results of this analysis appear in the parametric study of the model presented in Section 6.2. The more complete results will be presented in the forthcoming report.

Because of the cost of numerical computation this analysis is performed in the frequency domain with calculation of the PSD and RMS acceleration values for an ensemble of earthquakes. By assuming that the strong motion part of a time history is a stationary process, the statistical characteristics of the peak acceleration can also be estimated. The study of the effect of variations in the above mentioned parameters is based on the RMS in most cases and on peak values estimated from RMS when necessary.

6.3.3 Analysis of Recording Networks Biases.

The nature and quality of the seismic records available depend primarily on the spatial distribution of the recording stations. To this add biases introduced by the technology of the recording devices, such as the operating range of frequencies or the dynamic range or the threshold triggering value of acceleration.

Our knowledge of the physical phenomenon, therefore, has been based on a filtered version (the filter data) of the ensemble of data actually produced (the true data). In an ongoing project the correlation between the distribution of earthquake magnitude on a given fault, spatial distribution of recording stations and the distribution of peak value of accelerations is studied. The effect of recorder-triggering threshold is also analyzed. The ultimate goal is to devise a methodology to determine a network-independent attenuation law.

This is important for engineering computations because it permits us to perform site dependent seismic hazard analysis with data borrowed from other locations rather than from the seismic zone associated with the site under consideration. (Especially when we realize that potential sites for critical facilities are not always located in the middle of an existing recording network with a lot of data!)

6.3.4 Spatial Statistics of Acceleration Records

In most dynamic analyses of structures submitted to seismic excitation a single input location is chosen. Generally all the points located at the foundation level are subject to that excitation. It has been recognized, however, that the changing characteristics of the input in space may be an important factor in stress concentration or other behavior such as rocking or torsional motion that is unpredictable with a single input. Although these "secondary" effects are believed to be negligible for most structures, it becomes increasingly important with the horizontal dimensions. Such is the case of bridges or very long buildings and other special facilities, such as a linear accelerators or lifelines.

The first step in dealing with this engineering problem is to evaluate the spatial correlation of the seismic records. This analysis will be performed in the frequency domain by computing the cross-spectral density function of each couple of ensemble of records at stations located on a grid centered on the site of interest. It will be performed for the horizontal components as well as for the vertical components of the motion. In addition, the correlation between horizontal and vertical components will be studied. Hence a better knowledge will be gained which will help selecting vertical components when needed in engineering analyses.

6.3.5 Quantitative Analyses

The most deterministic use of the model is envisioned in the reproduction of actual historic earthquakes for which acceleration records are available and all source parameters are reasonably known. The number of such cases is very limited, and if we consider the restrictions due to the model itself, it is even more limited. The Parkfield is a very good candidate for this type of calculation. Its rupture surface is known (Aki, 1979, Eaton & Al, 1970). The predicted motion may be compared with actual records, and the model may be calibrated by trial and error.

In other cases where time histories are requested at a given site for a set of hypothetical earthquakes, it may be possible to use the model developed here provided one can define the various parameters within reasonable bounds.

An extension of the above is the integrated methodology for computing pseudo-time-histories, as described in Savy (1978). In that particular case an ensemble of time histories is generated by simulation, the common characteristic of which is to possess a constant probability (Iso-return Period) Power Spectral Density. That is, where the value of each point of the P.S.D. has a given probability of being exceeded during a set period of time (life time).

Appendix 3.1

For a dislocation in the y-z plane (see Fig. 3.1) with slip in the y direction, the forces forming the double couple are in the y-x plane only, as shown in Fig. 3 of Maruyama (1963). The explicit form for the m-component of the displacement field in Q due to such dynamic forces with time dependence $\exp(i\omega t)$ at their origin is:

$$T_{yx}^{m}(\omega)e^{i\omega t}$$

and $T_{yx}^{m}(\omega)$ is given by Eq. 35:

$$\begin{aligned} T_{yx}^{m}(\omega) = \frac{i}{4\pi} \Bigg\{ & \alpha_1^2 h_1^{(2)}(\alpha_1 r) \left| \frac{-(\frac{2}{5})\mu}{\lambda+2\mu} (\delta_{my}\gamma_x + \delta_{xm}\gamma_y) \right| \\ & + \alpha_1^2 h_3^{(2)}(\alpha_1 r) \left| \frac{-(\frac{2}{5})\mu}{\gamma+2\mu} (\delta_{my}\gamma_x + \delta_{xm}\gamma_y) + \frac{2\mu}{\lambda+2\mu} \gamma_x\gamma_y\gamma_m \right| \\ & + \beta_1^2 h_1^{(2)}(\beta_1 r) \left| -\frac{3}{5}(\delta_{my}\gamma_x + \delta_{xm}\gamma_y) \right| \\ & + \beta_1^2 h_3^{(2)}(\beta_1 r) \left| \frac{2}{5}(\delta_{my}\gamma_x + \delta_{xm}\gamma_y) - 2\gamma_x\gamma_y\gamma_m \right| \Bigg\} \end{aligned} \qquad \text{(A3.1.1)}$$

where:

$$\alpha_1 = \frac{\omega}{\alpha}, \quad \beta_1 = \frac{\omega}{\beta},$$

α and β are the P and S wave velocities,

μ and λ are the Lame' constants,

δ_{ij} is the Kronecker delta:

$$\delta_{ij} = 1 \quad \text{if } i=j$$

$$= 0 \quad \text{if } i \neq j,$$

γ_i is the direction cosine of direction i, and the function $h_i^{(2)}(\rho)$ are the spherical Hankel functions of the second kind, given by:

$$h_1^{(2)}(\rho) = \left(-\frac{1}{\rho} + \frac{i}{\rho^2}\right) e^{-i\rho}$$

$$h_3^{(2)}(\rho) = \left(\frac{1}{\rho} - 6\frac{i}{\rho^2} - 15\frac{1}{\rho^3} + 15\frac{i}{\rho^4}\right) e^{-i\rho}.$$

If we limit the estimation of the h functions by neglecting the terms in $\frac{1}{r^3}$ and $\frac{1}{r^4}$ and replace ρ by $\frac{\omega r}{c}$ where c can be alternatively equal to α or β, it becomes:

$$\begin{cases} c_1^2 h_1^{(2)}(c_1 r) = \frac{\omega}{cr}\left(-1 + \frac{ic}{\omega r}\right) e^{\frac{-i\omega r}{c}} \\ c_1^2 h_3^{(2)}(c_1 r) = \frac{\omega}{cr}\left(1 - 6\frac{ic}{\omega r}\right) e^{\frac{-i\omega r}{c}} \end{cases} \qquad \text{(A3.1.2)}$$

$$\text{where } c_1 = \frac{\omega}{c}.$$

Separating $T_{yx}^{m}(\omega)$ into the sum of the P and S contributions,

$$T_{yx}^{m}(\omega) = \mathscr{P}_{yx}^{m}(\omega) + \mathscr{S}_{yx}^{m}(\omega),$$

and defining, Δ as $\Delta = \Delta_{yx}^{m} = \delta_{my}\gamma_x + \delta_{xm}\gamma_y$, and using Eq. A3.1.2 in A3.1.1,

gives the following:

$$\mathscr{P}^{m}_{yx}(\omega) = \frac{i\omega}{4\pi\alpha r} e^{-\frac{i\omega r}{\alpha}} \left\{ \frac{2\mu}{\lambda+2\mu} \frac{i\alpha}{\omega r}\Delta + \frac{2\mu}{\lambda+2\mu}\left(1-\frac{6i\alpha}{\omega r}\right)\gamma_x\gamma_y\gamma_m \right\}$$

$$\mathscr{S}^{m}_{yx}(\omega) = \frac{i\omega}{4\pi\beta r} e^{-\frac{i\omega r}{\beta}} \left\{ -\frac{3}{5}\Delta\left(-1+\frac{i\beta}{\omega r}\right) + \frac{2}{5}\Delta\left(1-\frac{6i\beta}{\omega r}\right) - 2\left(1-\frac{6i\beta}{\omega r}\right)\gamma_x\gamma_y\gamma_m \right\}$$

Recalling the relationships between velocities and Lame' constants,

$$\alpha^2 = \frac{\lambda+2\mu}{\rho}, \quad \beta^2 = \frac{\mu}{\rho},$$

leads to

$$\mathscr{P}^{m}_{yx}(\omega) = \frac{i\omega}{2\pi\alpha r} e^{\frac{-i\omega r}{\alpha}} \left(\frac{\beta}{\alpha}\right)^2 \left[\frac{i\alpha\Delta}{\omega r} + \left(1-\frac{6i\alpha}{\omega r}\right)\gamma_x\gamma_y\gamma_m\right]$$

$$\mathscr{S}^{m}_{yx}(\omega) = \frac{i\omega}{4\pi\beta r} e^{\frac{-i\omega r}{\beta}} \left[\Delta\left(1-\frac{3i\beta}{\omega r}\right) - 2\left(1-\frac{6i\beta}{\omega r}\right)\gamma_x\gamma_y\gamma_m\right]$$

For the three different m components, Δ takes the values shown in the following table:

m (direction)	δ (values of Kronecker δ)	Δ
x	$\delta_{xx}=1$, $\delta_{xy}=0$	γ_y
y	$\delta_{xy}=0$, $\delta_{yy}=1$	γ_x
z	$\delta_{zx}=\delta_{zy}=0$	0

Then in this x, y, z coordinate system, the vectors and are given by:

$$\mathscr{P}_{yx}(\omega) = \frac{i\omega}{2\pi\alpha r} e^{\frac{-i\omega r}{\alpha}} \left(\frac{\beta}{\alpha}\right)^2 \begin{vmatrix} \frac{i\alpha}{\omega r}\gamma_y + (1-\frac{6i\alpha}{\omega r})\gamma_x^2\gamma_y \\ \frac{i\alpha}{\omega r}\gamma_x + (1-\frac{6i\alpha}{\omega r})\gamma_x\gamma_y^2 \\ (1-\frac{6i\alpha}{\omega r})\gamma_x\gamma_y\gamma_z \end{vmatrix} \qquad \text{(A3.1.3)}$$

$$\mathscr{S}_{yx}(\omega) = \frac{i\omega}{4\pi\beta r} e^{\frac{-i\omega r}{\beta}} \begin{vmatrix} (1-\frac{3i\beta}{\omega r})\gamma_y - 2(1-\frac{6i\beta}{\omega r})\gamma_x^2\gamma_y \\ (1-\frac{3i\beta}{\omega r})\gamma_x - 2(1-\frac{6i\beta}{\omega r})\gamma_x\gamma_y^2 \\ -2(1-\frac{6i\beta}{\omega r})\gamma_x\gamma_y\gamma_z \end{vmatrix}$$

In order to facilitate the rest of the analysis, the above relationships are expressed in the spherical coordinate system (r,θ,ϕ) as shown in Figure 3.1.

The transformation matrix $\mathscr{T}$ is given by:

$$\mathscr{T} = \begin{vmatrix} \sin\theta\sin\phi & \sin\theta\cos\phi & \cos\theta \\ \cos\theta\sin\phi & \cos\theta\cos\phi & -\sin\theta \\ \cos\phi & -\sin\phi & 0 \end{vmatrix} \qquad \text{(A3.1.4)}$$

so that the direction cosines of the direction x, y, and z in this (r,θ,ϕ) system, become:

$$\begin{cases} \gamma_x = \sin\theta\sin\phi \\ \gamma_y = \sin\theta\cos\phi \\ \gamma_z = \cos\theta \end{cases}$$

After rearranging the trigonometric terms, $\mathscr{P}$ and $\mathscr{S}$ as expressed in the spherical system are:

$$\begin{cases} \mathscr{P}_{yx}(\omega) = \dfrac{i\omega e^{\frac{-i\omega r}{\alpha}}}{4\pi\alpha r}\left(\dfrac{\beta}{\alpha}\right)^2 \left\{\dfrac{2i\alpha}{\omega r}\begin{vmatrix} \sin^2\theta\sin2\phi \\ \dfrac{\sin2\theta\sin2\phi}{2} \\ \sin\theta\cos2\phi \end{vmatrix} + \left(1-\dfrac{6i\alpha}{\omega r}\right)\begin{vmatrix} \sin^2\theta\sin2\phi \\ 0 \\ 0 \end{vmatrix}\right. \\ \\ \mathscr{S}_{yx}(\omega) = \dfrac{i\omega e^{\frac{-i\omega r}{\beta}}}{4\pi\beta r}\left\{\left(1-\dfrac{3i\beta}{\omega r}\right)\begin{vmatrix} \sin^2\theta\sin2\phi \\ \dfrac{\sin2\theta\sin2\phi}{2} \\ \sin\theta\cos2\phi \end{vmatrix} - \left(1-\dfrac{6i\beta}{\omega r}\right)\begin{vmatrix} \sin^2\theta\sin2\phi \\ 0 \\ 0 \end{vmatrix}\right. \end{cases}$$

Let us define two vectors R^P and R^S in the following way:

$$R^P = \begin{vmatrix} \sin^2\theta\sin2\phi \\ 0 \\ 0 \end{vmatrix} \quad \text{and} \quad R^S = \begin{vmatrix} 0 \\ \frac{\sin2\theta\sin2\phi}{2} \\ \sin\theta\cos2\phi \end{vmatrix}$$

R^P is therefore in the radial direction $\vec{r}$, while R^S is parallel to the plane $(\vec{\theta},\vec{\phi})$, perpendicular to $\vec{r}$. $\mathscr{P}$ and $\mathscr{S}$ may be expressed as a linear combination of R^P and R^S, in the following manner:

$$\begin{cases} \mathscr{P}_{yx}(\omega) = \frac{i\omega}{4\pi\alpha r}\left(\frac{\beta}{\alpha}\right)^2 e^{\frac{-i\omega r}{\alpha}} \left\{R^P + \frac{2i\alpha}{\omega r}(R^S - 2R^P)\right\} \\ \mathscr{S}_{yx}(\omega) = \frac{i\omega}{4\pi\beta r} e^{\frac{-i\omega r}{\beta}} \left\{R^S - \frac{3i\beta}{\omega r}(R^S - R^P)\right\} \end{cases} \qquad \text{(A 3.1.5)}$$

Since $T_{yx}(\omega)$ is the sum of the above two expressions, it is clear that as the distance from the observer to the source increases, the correction terms to the first order approximation can be neglected and we are back to the first order solution presented by Mikumo (1969).

This correction will affect mostly the low frequency end of the spectrum, for medium distances (r), thus not affecting the peak acceleration that much, but for short distances this correction could become large. More specifically, if we consider r of the order of one wavelength, at 10Hz, and using the limiting value of $\frac{c}{\omega r} = \frac{1}{2}$ derived in Appendix A3.2, a simple calculation could show that the value of the correction is at

least three times the far field term for the P wave. For the S wave this ratio would be approximately two.

Appendix 3.2

Limits of validity of the second order approximation.

In a manner similar to the determination of the limits of validity of the Fraunhofer approximation, lets study the effect of the error in the source spectrum introduced by making the approximation.

Defining the source spectrum as:

$$\Omega(Q,\omega) = \int_{\Sigma} i\omega\overline{\Delta u}(\omega)[-C_1 h_1^{(2)}(\omega) + C_2 h_3^{(2)}(\omega)]d\Sigma \qquad \text{(A3.2.1)}$$

where: $h_1^{(2)}$ and $h_3^{(2)}$ are defined in A.3.1, C_1 and C_2 are geometry dependent constants, and $\overline{\Delta u}(\omega)$ is the Fourier transform of the dislocation function.

The error introduced in $\Omega(Q,\omega)$ will be significant if the error introduced in the polar angle of the complex number:

$$-C_1 h_1^{(2)}(\omega) + C_2 h_3^{(2)}(\omega)$$

is greater than $\pi/2$, and the error in its modulus is large. Since the coefficients C_1 and C_2 are of the same order, we can ignore them and only consider the complex number $h_1^{(2)}(\omega) + h_3^{(2)}(\omega)$. This in turn will only provide one order of magnitude of the range of validity of the approximation.

Let

$$-h_1^{(2)}(\omega) + h_3^{(2)}(\omega) = (A+\Delta A)e^{i(\theta+\Delta\theta)}\, e^{\frac{-i\omega r}{c}}$$

then, using the definition of $h(\omega)$, and ignoring the constants gives:

$$(A+\Delta A)e^{i(\theta+\Delta\theta)} = \left\{\left[1-\frac{ic}{\omega r}+1-\frac{6ic}{\omega r}\right] - \left[15\left(\frac{c}{\omega r}\right)^2\left(1+\frac{ic}{\omega r}\right)\right]\right\}$$

$$= \left\{\left(2-\frac{7ic}{\omega r}\right) - 15\left(\frac{c}{\omega r}\right)^2\left(1+\frac{ic}{\omega r}\right)\right\}$$

$$= \left[2-15\left(\frac{c}{\omega r}\right)^2\right] - \frac{ic}{\omega r}\left[7+15\left(\frac{c}{\omega r}\right)^2\right] \qquad \text{(A3.2.2)}$$

$$A + \Delta A = \left[(2-15\varepsilon^2)^2 + \varepsilon^2(7+15\varepsilon^2)^2\right]^{1/2}, \quad \varepsilon = \frac{c}{\omega r}$$

$$tg(\theta+\Delta\theta) = -\varepsilon\,\frac{7+15\varepsilon^2}{2-15\varepsilon^2}$$

Assuming that $\Delta\theta$ is small, a series development limited to the first order for the tangent is:

$$tg(\theta+\Delta\theta) = tg(\theta) + \Delta\theta\,\frac{1}{1+tg^2\theta}$$

$tg\theta$ is given by the value after neglecting the 3rd and 4th order terms in $(\frac{1}{r})$ that is:

$$tg\theta = -\frac{7\varepsilon}{2}, \quad \frac{1}{1+tg^2\theta} = \frac{4}{4+49\varepsilon^2}$$

so that $\Delta\theta$ is given by the following:

$$\Delta\theta = -\left\{\varepsilon\left(\frac{7+15\varepsilon^2}{2-15\varepsilon^2}\right) - \frac{7\varepsilon}{2}\right\}\left(\frac{4+49\varepsilon^2}{4}\right) = \frac{-135\varepsilon^3}{8}\left(\frac{4+49\varepsilon^2}{2-15\varepsilon^2}\right)$$

The assumption of a small $\Delta\theta$ implies that ε is also small and therefore $|\Delta\theta| \simeq \frac{135}{4}\varepsilon^3 \simeq 36\varepsilon^3$. The condition on the error in the angle θ then becomes:

$$36\varepsilon^3 < \frac{\pi}{2} \quad \text{or} \quad \varepsilon = \frac{c}{\omega r} < \sim\frac{1}{2} \tag{A3.2.3}$$

The relative error on the modulus A is: $\left|\frac{\Delta A}{A}\right| = \left|\frac{A+\Delta A}{A} - 1\right|$. A simple calculation of $\left|\frac{\Delta A}{A}\right|$ for values of $\varepsilon \leq \frac{1}{2}$ shows that it is always smaller than 40% and drops very fast to 10% approximately when ε=.4. This order of magnitude is consistent with the projected use of the model so that the limits of validity will be for:

$$\frac{c}{\omega r} \leq \frac{1}{2}$$

Appendix 3.3

Derivation of the second order finiteness condition.

Consider a dislocation surface with largest dimension L,

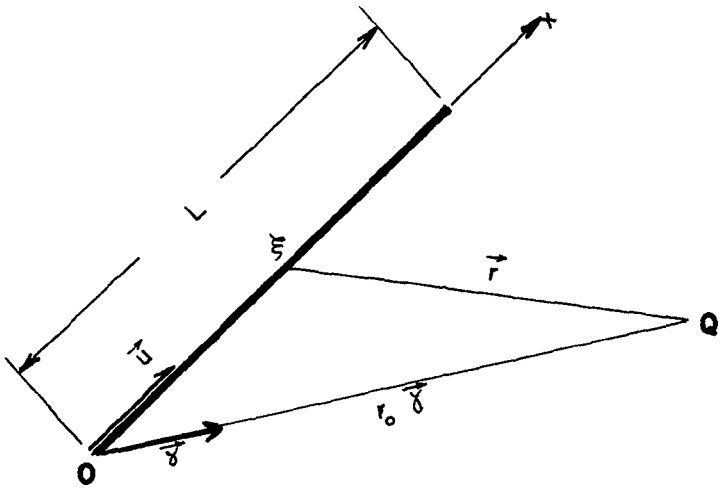

$\vec{U}$ = unit vector along Ox

$\vec{\gamma}$ = unit vector along OQ

Fig. A3.3.1

Assuming that the largest dimension is in the plane QOx, is shown in Fig. A3.3.1, the distance r between the observation point Q and the rupture point can be computed as follows.

$$\vec{r} = r_0\vec{\gamma} - \xi\vec{U}$$

$$r = |\vec{r}| = (\vec{r}\cdot\vec{r})^{1/2} = \left\{(r_0\vec{\gamma}-\xi\vec{U})\cdot(r_0\vec{\gamma}-\xi\vec{U})\right\}^{1/2}$$

$$= [r_0^2 - 2r_0\xi(\vec{\gamma}\cdot\vec{U}) + \xi^2]^{1/2}$$

And since $\vec{\gamma}\cdot\vec{U} = \cos\phi$, the distance r becomes:

$$r = r_0 \left[1 - 2\frac{\xi}{r_0}\cos\phi + \left(\frac{\xi}{r_0}\right)^2\right]^{1/2}$$

Assuming that $\frac{\xi}{r_0} << 1$ we can approximate r by a series expansion which we limit here to the third order for the purpose of estimating the first two terms of order higher than two which are neglected.

Let $\lambda = \frac{\xi}{r_0}$, the series expansion of r gives

$$r = r_0 \left\{1 + \frac{1}{2}(-2\lambda\cos\phi+\lambda^2) - \frac{1}{8}(-2\lambda\cos\phi+\lambda^2)^2 + \frac{1}{16}(-2\lambda\cos\phi)^3 + O(\lambda^4)\right\}$$

Collecting the terms in ascending order up to order 3:

$$r = r_0 \left\{1 - \lambda\cos\phi + \frac{1}{2}\lambda^2\sin^2\phi + \frac{1}{2}\lambda^3\cos\phi\sin^2\phi + O(\lambda^4)\right\}$$

The approximated r used here is then:

$$r \simeq r_0\left\{1 - \frac{\xi}{r_0}\cos\phi + \frac{1}{2}\left(\frac{\xi}{r_0}\sin\phi\right)^2\right\} \qquad \text{(A3.3.1)}$$

the first term neglected is therefore:

$$\Delta r = \frac{r_0}{2}\left(\frac{\xi}{r_0}\right)^3 \cos\phi\sin^2\phi$$

The wave form will be negligibly altered if the error Δr on r is smaller than a quarter wavelength of the wave considered. (Aki & Richards, 1980). Therefore if L is the largest dimension of the finite rupture this condition becomes:

$$\frac{r_0}{2}\left(\frac{L}{r_0}\right)^3 \cos\phi\sin^2\phi \leq \lambda(\omega) \text{ (wavelength at frequency } \omega) \qquad \text{(A3.3.2)}$$

Since $\lambda(\omega) = \frac{c}{f}$, and considering that the worst case occurs for the S waves (i.e., $c = \beta$) and for the maximum frequency f_{max}, the maximum length L_{max} then becomes:

$$L_{max}^{(2)} = \left\{\frac{\beta}{2f_{max}} \frac{r_0^2}{\cos\phi\sin^2\phi}\right\}^{1/3} \qquad \text{(A3.3.3)}$$

The corresponding 1st order approximation on the other hand would be valid for values of L less than $L_{max}^{(1)}$ given by:

$$L_{max}^{(1)} = \frac{1}{\sin\phi}\left\{\frac{\beta r_0}{2f_{max}}\right\}^{1/2} \qquad \text{(A.3.3.4)}$$

where f_{max} is the maximum frequency desired, in H_z.

As a comparison between L_{max} and L_{max}, the Fig. A3.3.2 shows that $L^{(2)}$ is always substantially larger than $L^{(1)}$, and blows up to infinity at $\Phi = 0$ and $\Phi = \frac{\pi}{2}$. By opposition, $L^{(1)}$ is minimum when $\Phi = \frac{\pi}{2}$. For instance, for r_0=8km, β=3.5km/s and f_{max}=20Hz, (values used for Fig. A3.2) the minimum values of $L_{max}^{(1)}$ and $L_{max}^{(2)}$ are:

$$\min(L_{max}^{(1)}) = .84 \text{ km} \quad \text{at } \Phi = \frac{\pi}{2}$$

$$\min(L_{max}^{(2)}) = 2.44 \text{ km} \quad \text{at } \Phi = 54$$

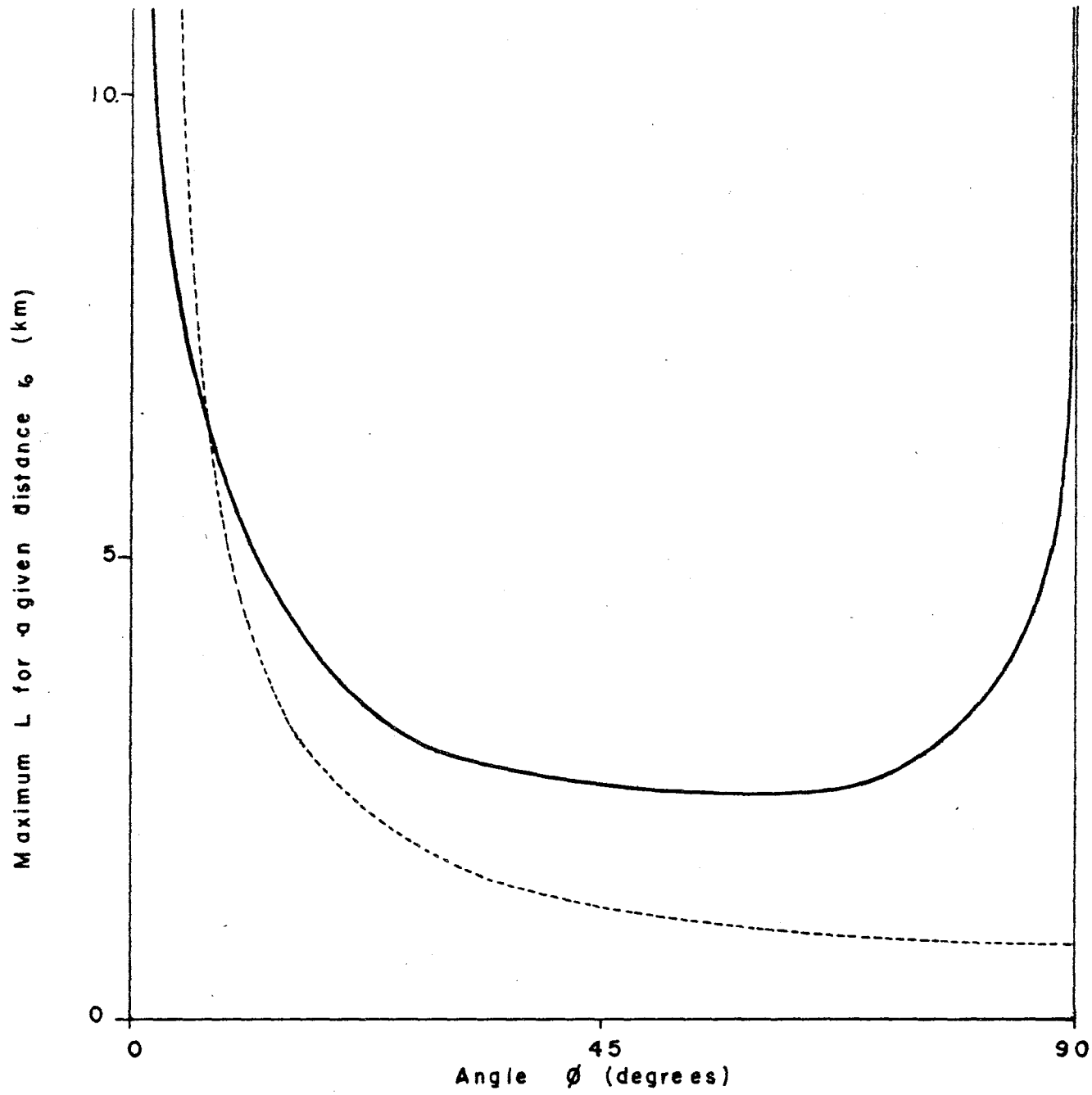

Figure A3.3.2 Comparison of 1st approximation (dashed line) vs. 2nd approximation, for $r_0 = 8$km, $\beta = 3.5$km/s and a maximum frequency of 20Hz.
The vertical axis gives the maximum allowable patch's length (in km) as a function of the angle ϕ.

The figure A3.3.3 shows the typical shape of the domain around a fault of length L where the approximation is not valid. Both first and second order approximation domains are shown. The minimum distance r_{min} (plotted on Fig. A3.3.3) at which the observation point Q must be for the approximation to be valid is easily found as:

$$\text{1st order:} \quad r_{min}^{(1)} = \frac{2f_{max}}{\beta} \sin^2\phi \; L^2$$

$$\text{2nd order:} \quad r_{min}^{(2)} = \left(\frac{2f_{max}}{\beta} \sin^2\phi\cos\phi\right)^{1/2} L^{3/2}$$

The values of r_{min} are tabulated in Table A3.1. A glance at Table A3.3.1 shows that for all practical purposes the 2nd order approximation is valid, but the 1st order approximation becomes fast invalid. The maximum value for r_{min} is obtained along the normal to the fault (ϕ=90º) with the first order approximation; and at ϕ=54.73º with the second order approximation. As soon as $L \geq 3$ km the observation point has to be in the range of 100 km far, for the approximation to br valid at all angles. For most cases the second order approximation will allow computing the motion without further subdivision of the rupture area.

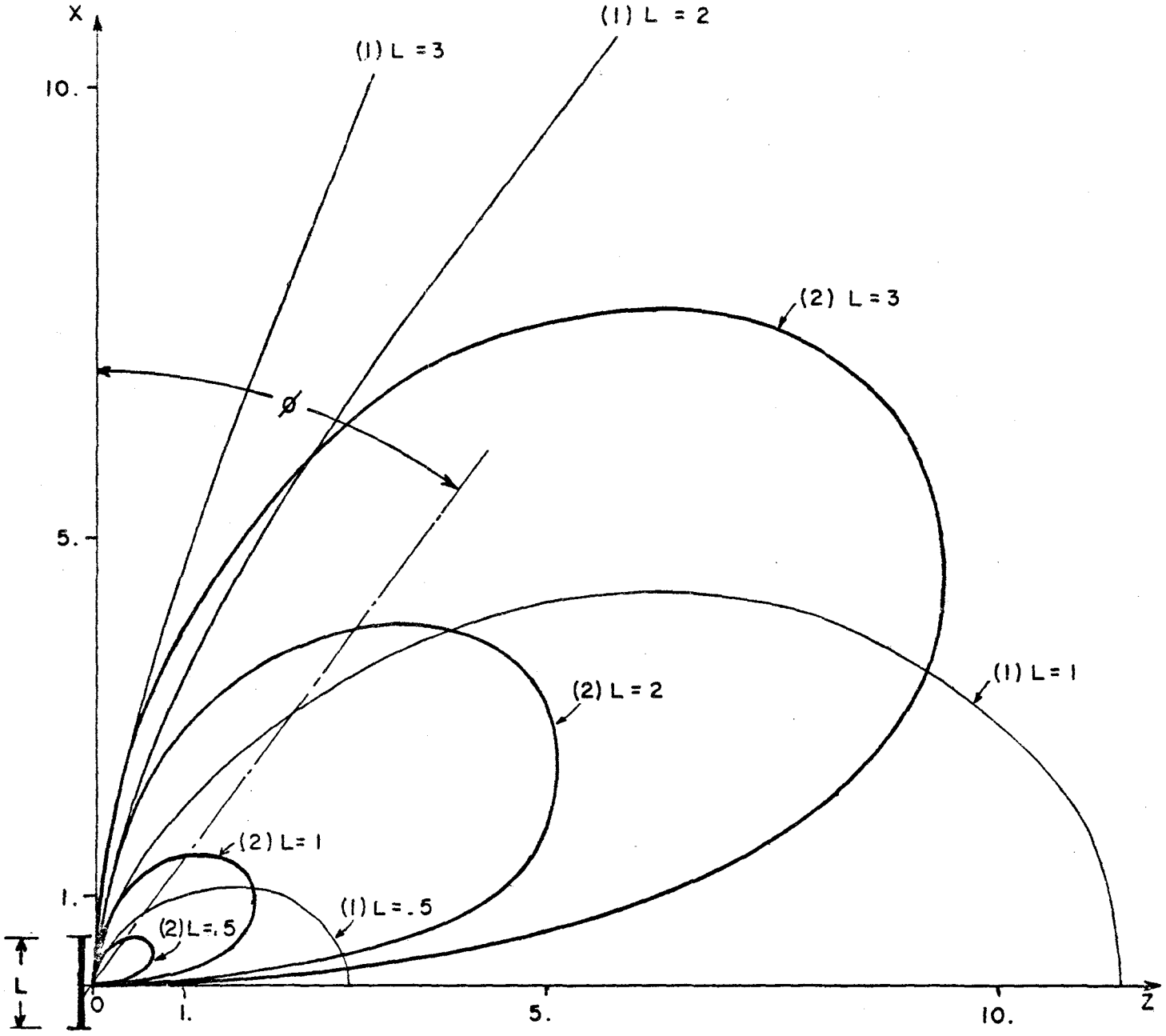

Figure A3.3.3 Domains of validity of the 1st order approximation (curves (1)) and 2nd order approximation (curves (2)). For a given length of the single element fault (patch) the approximation is valid if the site is outside the appropriate curve (the distance scale on Ox and Oz in km).

TABLE A3.3.1

Values of the minimum distance at which the finiteness condition is valid for 20 Hz maximum frequency.

Tabulation for 7 rupture area largest dimensions L and 2 computed values $r^{(1)}$ and $r^{(2)}$ for 1st and 2nd order approximation versus the angle ϕ.

L (km) / ϕ (deg.)	.5		1.		2.		3.		.5		10.		15.	
	(1)	(2)	(1)	(2)	(1)	(2)	(1)	(2)	(1)	(2)	(1)	(2)	(1)	(2)
0	0	0	0	0	0	0	0	0	0	0	0	0	0	0
11.25	.11	.23	.44	.65	1.74	1.85	3.91	3.39	10.9	7.30	44.0	20.7	98	38.0
22.5	.42	.44	1.67	1.24	6.70	3.52	15.1	6.46	42.0	13.9	167	39.3	376	72.0
33.75	.88	.61	3.53	1.71	14.1	4.84	31.7	8.90	88.0	19.1	353	54.0	—	99.0
39.23	—	.67	—	1.88	—	5.22	—	9.78	—	21.0	—	59.5	—	109
45	1.43	.71	5.71	2.01	22.9	5.69	51.4	10.4	143	22.5	571	64	—	117
54.73	—	.74	7.62	2.10	30.5	5.93	68.6	10.9	191	23.5	762	66	—	122
56.25	1.98	.74	7.90	2.10	31.6	5.93	71.0	10.9	198	23.4	—	66	—	122
63.43	—	.71	—	2.02	—	5.72	—	10.5	—	22.6	—	64	—	118
67.5	2.44	.68	9.75	1.93	39.0	5.48	88.0	10.0	244	21.6	—	61	—	112
78.75	2.75	.52	11.0	1.46	44.0	4.14	99.0	7.61	275	16.4	—	46	—	85.0
90	2.86	0	11.4	0	45.7	0	103	0	286	0	—	0	—	0

(1) for 1st order r_{min} values

(2) —— 2nd ——————————

all values of r in k.m.

Appendix 3.4

1. Dislocation along Oy and propagation along Oz.

The roles of ξ and η as expressed in Eq. 3.17 are exchanged so that performing the integrations and simplifying, the solution remains the same if the following alternate definitions are made:

$$T_W^c = -\frac{W}{2}\left(\frac{1}{v} - \frac{\cos\theta}{c}\right)$$

$$T_L^c = -\frac{L}{2}\frac{\sin\theta\cos\phi}{c} \qquad \text{(A3.4.1)}$$

$$K^c = -\frac{W}{2c}\frac{\cos\theta}{T_W^c}\left(1-\frac{e^{2i\omega T_W^c}}{J_1^c}\right) + \left(1-\frac{e^{-2i\omega T_L^c}}{J_2^c}\right)$$

2. Dip slip case.

The same steps as performed in A3.1 are performed here by replacing T_{yx}^m by T_{zx}^m. Then

$$\Delta_{zx}^m = \delta_{mz}\gamma_z + \delta_{xm}\gamma_z$$

so that Eq. A3.1.3 becomes

$$\left.\begin{aligned}\mathscr{P}_{zx}(\omega) &= \frac{i\omega}{4\pi\alpha r}\, e^{\frac{-i\omega r}{\alpha}}\left(\frac{\beta}{\alpha}\right)^2\left[\frac{2i\alpha}{\omega r}\begin{bmatrix}\gamma_z\\0\\\gamma_x\end{bmatrix} + 2\left(1-\frac{6i\alpha}{\omega r}\right)\gamma_x\gamma_z\begin{bmatrix}\gamma_x\\\gamma_y\\\gamma_z\end{bmatrix}\right]\\ \mathscr{S}_{zx}(\omega) &= \frac{i\omega}{4\pi\beta r}\, e^{\frac{-i\omega r}{\beta}}\left[\left(1-\frac{3i\beta}{\omega r}\right)\begin{bmatrix}\gamma_z\\0\\\gamma_x\end{bmatrix} - 2\left(1-\frac{6i\beta}{\omega r}\right)\gamma_x\gamma_z\begin{bmatrix}\gamma_x\\\gamma_y\\\gamma_z\end{bmatrix}\right]\end{aligned}\right\} \qquad \text{(A3.4.2)}$$

Transforming to spherical coordinates by using (A3.1.4) gives

$$\left.\begin{aligned}\mathscr{P}_{zx}(\omega) &= \frac{i\omega}{4\pi\alpha r}\left(\frac{\beta}{\alpha}\right)^2 e^{\frac{-i\omega r}{\alpha}}\left\{R^P + \frac{2i\alpha}{\omega r}[R^S - 2R^P]\right\}\\ \mathscr{S}_{zx}(\omega) &= \frac{i\omega}{4\pi\beta r} e^{\frac{-i\omega r}{\beta}}\left\{R^S - \frac{3i}{r}[R^S - R^P]\right\}\end{aligned}\right\}$$

that is, the same equation as for the strike slip case (Eq. A3.1.5), but where R^P and R^S are here:

$$R^P = \begin{bmatrix}\sin 2\theta\sin\phi\\ 0\\ 0\end{bmatrix} \qquad R^S = \begin{bmatrix}0\\ \cos 2\theta\sin\phi\\ \cos\theta\cos\phi\end{bmatrix}$$

By going through the same process as for the strike slip presented in Chapter III the final solution is the same as in Eq. 3.25, where the following terms are now defined by:

$$\begin{cases}\gamma_1 = \sin 2\theta\sin\phi\\ \gamma_2 = \cos 2\theta\sin\phi\\ \gamma_3 = \cos\theta\cos\phi\end{cases}$$

$$K^c = F_W^c\left(1 - \frac{e^{2i\omega T_W^c}}{J_1^c}\right) - F_L^c\left(1 - \frac{e^{-2i\omega T_L^c}}{\omega T_L^c}\right)$$

$$J_1^c = e^{i\omega T_W^c} \frac{\sin\omega T_W^c}{\omega T_W^c}$$

$$J_2^c = e^{-i\omega T_L^c} \frac{\sin\omega T_L^c}{\omega T_L^c}$$

(a) Propagation along Oz,

$$\begin{cases} T_W^c = \frac{-W}{2}\left(\frac{1}{v} - \frac{\cos\theta}{c}\right) , \quad F_W^c = \frac{-W}{2c}\frac{\cos\theta}{T_W^c} \\ T_L^c = \frac{-L}{2}\frac{\sin\theta\cos\phi}{c} , \quad F_L^c = -1 \end{cases}$$

(b) Propagation along Oy,

$$\begin{cases} T_W^c = \frac{W}{2}\frac{\cos\theta}{c} , \quad F_W^c = -1 \\ T_L^c = \frac{L}{2}\left(\frac{1}{v} \frac{\sin\theta\cos\phi}{c}\right) , \quad F_L^c = \frac{L\sin\theta\cos\phi}{2cT_L^c} \end{cases}$$

Appendix 4.1

DETERMINATION OF AN EQUIVALENT ARTIFICIAL EARTHQUAKE STRONG MOTION DURATION

A4.1.1 Introduction

The problem of determination of the duration of an earthquake record is a delicate one. There has been a variety of definitions depending on the intended use of the records. Engineers are more particularly interested in the strong motion part of earthquake records, and even so they propose several definitions. For instance, R. McGuire (1979) summarized four different techniques which can be used for the computation of the duration for engineering uses. These four techniques give different results, but it can be emphasized that they are not intended to be used in the same contexts.

The generation of Power Spectral Density functions (PSD) by our method, requires a knowledge of the strong motion duration without knowing the time history beforehand. In this case we want to simulate a large sample of records in order to compute the statistical characteristics of a type of earthquake at a given site. In order to avoid prohibitive computer costs we then limit ourselves to computation of F.A.S. for a limited number of frequency points (an order of magnitude smaller than the number of points required for time domain calculations). The P.S.D. is then computed by dividing the square of the FAS by the duration of the motion at the site. Such a technique implies that we are dealing with a stationary process--a wild departure from reality! (we mean here reality of our synthetic records).

In the technique used up until now in calculations (Savy, 1978), the time of a record was determined by the difference in time between the last arrival of an impulse at the site minus the first arrival. This obviously

did not account for the fact that a large earthquake record, for instance, may be made up of several strong motion parts with relative quietness in between this, impairing the PSD estimates (which imply a stationary process). In some of our previous calculations the estimate of duration was twice, and in some even more, the actual total strong motion duration which could be derermined visually from a plot of the time histories.

The method that we propose here must fulfill several conditions:

(i) not increase substantially the computation time,

and (ii) give an estimate of the total duration of the strong motion part of the record, that is the time duration during which part of the record can be considered as part of a same stationary strong motion process.

A4.1.2 Estimate of the Energy Time History

A.4.1.2.1 General Method

We first define a function proportional to the total energy radiated toward the observation point. A time history of this function is calculated in an approximate manner, independently of the calculations of FAS, and for a limited number of time points. The function is then scanned for its maximum, and the strong motion duration is defined as that portion of the time axis for which the energy function is above some fraction (to be determined by testing) of its maximum.

A.4.1.2.2 The Energy Proportional Time History

In this section we limit the derivations to the case of the energy of the S-wave generated by a patch small enough to use the far-field solution. The kinetic energy of a unit mass of ground at the observation point is proportional to the square of its velocity.

Let v(t) be the velocity at the site, the total energy received will be proportional to:

$$E \propto \int_0^\infty v^2(t)dt \qquad (A4.1.1)$$

and using Parseval's theorem it is also:

$$E \propto G = \int_0^\infty |V(\omega)|^2 \, d\omega \qquad (A4.1.2)$$

where: $V(\omega)$ is the Fourier transform of $v(t)$.

If we make the simplifying assumption that this energy is released by dislocation of the patch, in a stationary manner, the power input at the site from this given patch is therefore proportional to $\frac{E}{t}$; where t is the total rupture time of the patch. It is equal to the length of the patch divided by the rupture velocity (v_r).

$$P \propto \frac{E}{t} \qquad (A4.1.3)$$

$$t = \frac{\ell}{v_r} \qquad (A4.1.4)$$

P is proportional to the average power dissipated by the patch, at the site, and we can construct a curve proportional to the average power dissipated by superimposing the contribution of each patch as it is sketched in Figure A4.1.

The total strong motion duration may be determined as the sum of the time durations during which P is greater than a portion α of its maximum P_{max}. In such a method the discrete time definition does not have to be as fine as one needed for actual time history calculations. In practice we can decide to have ΔT as a fraction of the total anticipated maximum duration, and we can therefore choose the number of time points, say 40 for

instance. 40 seems adequate since it would give a ΔT = .1sec for a 4sec record, and ΔT = 1sec for a 40sec record. That is an accuracy of 2.5%. What we now need is a simple way of evaluating Eq. A4.1.2.

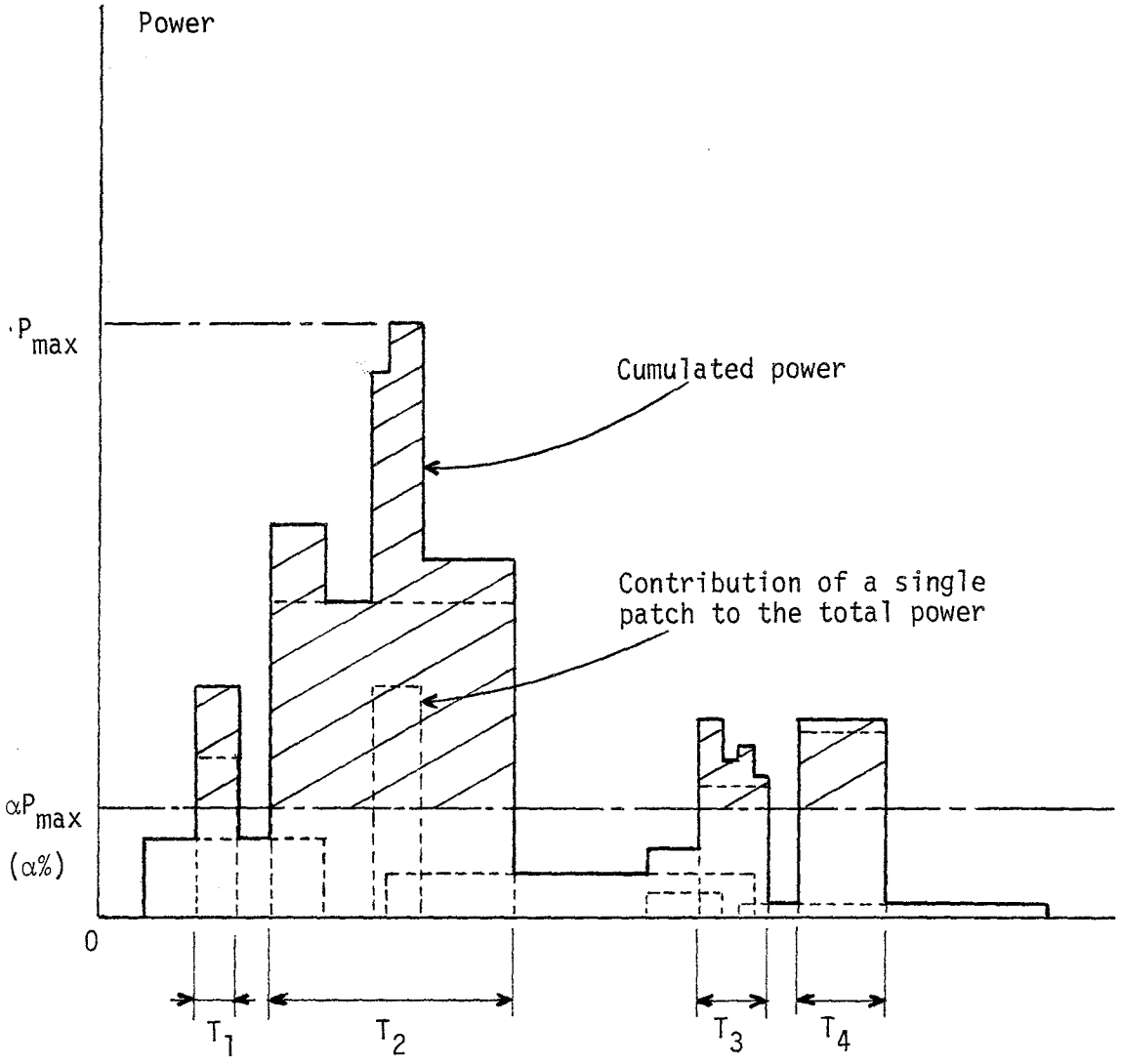

Total strong motion duration = $T_1 + T_2 + T_3 + T_4$

Figure A4.1.2 Average power spectral proportional function

A4.1.2.3 Total Energy Radiated Towards the Site by One Patch

The far field expression for the Fourier Transform of the velocity may be expressed by:

$$V(\omega) = \left(\frac{RM_0}{4\pi\rho\beta^3 r}\right)\left[\omega \frac{\sin\omega\frac{\tau}{2}}{\omega\frac{\tau}{2}} \frac{\sin\omega T_L}{\omega T_L} \frac{\sin\omega T_W}{\omega T_W} e^{-\frac{\omega r}{Q\beta}}\right] \qquad (A4.1.5)$$

(See Savy (1979) for definition of parameters).

If we only consider the part in the brackets, we notice that we have a product of 3 sinc functions. When we square a sinc function we know that most of the area under it is under the first lobe, so in order to calculate Eq. A4.1.2 we need only to integrate the part under the first lobe. Furthermore, in our case the product of the 3 sinc functions can be approximated by the one with the larger coefficient of ω, since we integrate only in the first lobe (see Figure A4.1.3).

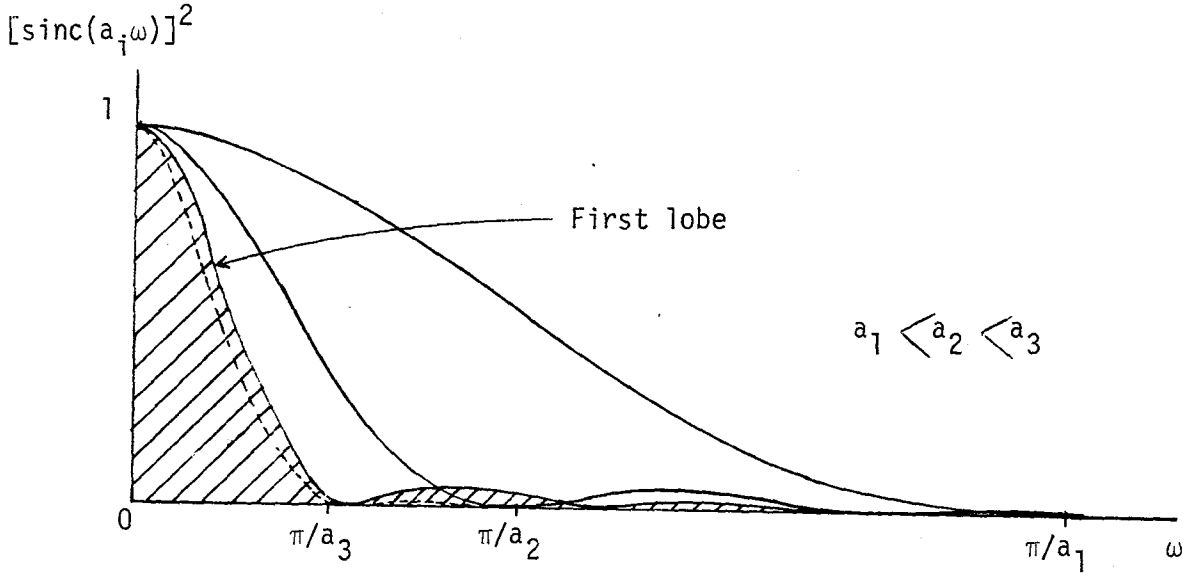

Figure A4.1.3 Representation of $(\sin^2 a\omega)$ where: $a_i = \frac{\tau}{2}, T_W, T_L$ for $T_L > T_W > \frac{\tau}{2}$. The product can be approximated by $\text{sinc}^2[\omega \max(a_i)]$.

We can rewrite $V(\omega)$ as:

$$V(\omega) \cong \frac{RM_0}{4\pi\rho\beta^3 r}\ y(\omega) = A\ y(\omega) \qquad \text{(A4.1.6)}$$

where:

$$y(\omega) = \frac{\sin a\omega}{a}\ e^{-b\omega} \qquad \text{(A4.1.7)}$$

$$\begin{cases} a = \max[\frac{\tau}{2},\ T_W,\ T_L] \\ b = \frac{r}{Q\beta} \end{cases}$$

Then Eq. A4.1.2 becomes:

$$G = \frac{A}{a^2}\int_0^\infty \sin^2 a\omega\ e^{-2b\omega}\ d\omega$$

$$= \frac{A}{a^2}\int_0^\infty (\frac{1-\cos 2a\omega}{2})\ e^{-2b\omega}\ d\omega$$

$$= \frac{A}{2a^2}\left\{\frac{e^{-2b\omega}}{2b}\Big|_\infty^0 - \int_0^\infty \cos 2a\omega\ e^{-2b\omega}\ d\omega\right\}$$

$$- \frac{A}{2a^2}\left\{\frac{1}{2b} - \int_0^\infty \cos 2a\omega\ e^{-2b\omega}\ d\omega\right\} \qquad \text{(A4.1.8)}$$

where:

$$A = \left(\frac{RM_0}{4\pi\rho\beta^3 r}\right)^2$$

Let:

$$t_1 = \cos 2a\omega\ e^{-2b\omega}$$

$$t_2 = \sin 2a\omega\ e^{-2b\omega}$$

$$T = t_1 + it_2 = e^{2ai\omega - 2b\omega} = e^{2(ai-b)\omega}$$

then:

$$\int_0^{\omega_2} T d\omega = \frac{1}{(2(ai-b)} \left(e^{2(ai-b)\omega_2} - 1\right)$$

$$= \frac{(ai+b)}{2(a^2+b^2)} \left[1-e^{-2b\omega_2}(\cos 2a\omega_2 + i\sin 2a\omega_2)\right]$$

$$\int_0^{\omega_2} \cos 2a\omega e^{-2b\omega} d\omega = \mathscr{R}\left[\int_0^{\omega_2} T d\right]$$

$$= \frac{1}{2(a^2+b^2)} \left[b - e^{-2b\omega_2} b\cos 2a\omega_2 + ae^{-2b\omega_2} \sin 2a\omega_2\right]$$

$$= \frac{b+e^{-2b\omega_2}(a\sin 2a\omega_2 - b\cos 2a\omega_2)}{2(a^2+b^2)}$$

where: ω_2 is the maximum frequency for which the FT of $V(\omega)$ is calculated. Then it becomes finally:

$$G = \frac{A}{4a^2}\left\{\frac{1}{b} - \frac{b+(a\sin 2a\omega_2 - b\cos 2a\omega_2)e^{-2b\omega_2}}{a^2+b^2}\right\} \qquad (A4.1.9)$$

if the quality factor Q is large or if we are dealing with large values of b (r small). G simplifies to:

$$G = \frac{A}{4(a^2+b^2)b} \qquad (4.1.10)$$

Appendix 5.1

The choice of n as being that value of the parameter for which the most probable value of the largest patch length is equal to the observed value is compared with the value obtained from a maximum likelihood technique and also by assuming that the observed value is closest to the mean.

(i) Mean of the largest value and standard deviation

Let Y be the random variable "largest value of ℓ on the fault with n patches," and normalize the total length of the fault to 1. The mean value of Y is a function of n, say $\mu_Y(n)$

$$E[Y|N] = \mu_Y(n) = \int_0^1 y\, f_{Y|N}(y|n)dy \qquad \text{(A5.1.1)}$$

integrating by parts:

$$= 1 - \int_0^1 F_{Y|N}(y|n)dy$$

where: $F_{Y|N}(y|n) = \left\{1 - (1-y)^{n-1}\right\}^n$ is the CDF of Y.

Similarly we can compute $E[Y^2|N]$. The variance is then given by

$$VAR[Y|N] = E[Y^2|N] - \left\{E[Y|N]\right\}^2 \qquad \text{(A5.1.2)}$$

It comes:

$$\begin{cases} \mu_Y(n) = 1 - Z_1(n) \\ \sigma_Y(n) = \left\{2(Z_1(n)-Z_2(n)) - Z_1^2(n)\right\} \end{cases} \qquad \text{(A5.1.3)}$$

where:

$$Z_1(n) = \int_0^1 (1-z^{n-1})^n \, dz$$

$$Z_2(n) = \int_0^1 (1-z)(1-z^{n-1})^n \, dz$$

Expanding the terms to the power n and integrating term by term finally gives:

$$\begin{cases} Z_1(n) = n! \sum_{i=0}^{n} \dfrac{(-1)^i}{i!(n-i)![1+i(n-1)]} \\ Z_2(n) = Z_1(n) - n! \sum_{k=0}^{n} \dfrac{(-1)^k}{k!(n-k)![2+k(n-1)]} \end{cases} \qquad \text{(A5.1.4)}$$

(ii) Maximum likelihood estimator of n

We have only one data point, so that the likelihood function is proportional to the probability density function. Maximizing that function for the parameter n is achieved by maximizing its logarithm.

$$f_{Y|n}(y|n) = n(n-1)(1-y)^{n-2}\left\{1 - (1-y)^{n-1}\right\}^{n-1} \qquad \text{(A5.1.5)}$$

$$L(n) = \text{Log}\, n + \text{Log}\, n\text{-}1 + (n-2)\text{Log}(1-y) + (n-1)\text{Log}[1 - (1-y)^{n-1}] \qquad \text{(A5.1.6)}$$

The value of n which makes L(n) maximum is solution of:

$$\frac{d\,L(n)}{dn} = 0 \qquad \text{(A5.1.7)}$$

that is:

$$0 = \frac{1}{n} + \frac{1}{n-1} + \text{Log}(1-y) + \text{Log}[1-(1-y)^{n-1}] - \frac{(n-1)(1-y)^{n-1}\text{Log}(1-y)}{1-(1-y)^{n-1}} \quad \text{(A .1.8)}$$

Table A5.1.1 gives the most probable value $\ell(\overset{*}{n})$, the mean value $\mu_Y(n)$ and the maximum likelihood largest length $\ell_L(n)$ as obtained from Eq. 5.13, A5.1.3, and A5.1.6, respectively. The two last columns give also the standard deviation (Eq. A4.1.3) and the coefficient of variation.

Conversely in Table A2 an observed value of the largest value is assumed as .04, .06, .08, .1, .2,..., .9 and the corresponding n and average patch length $\overline{\ell}$ are computed assuming as above that: first the observed value is the most probable one, second, it is the average, and last n maximizes the likelihood.

Except for small values of n, that is except for the cases when the largest patch length is within .6 to 1 the three methods give similar results. But the coefficient of variation (COV) (see Table A5.1.1), being of the order of 25 to 35%, the uncertainty on the estimate of n will be large enough so that any of the three techniques makes as much sense as the other 2. Therefore in the computations we chose the first method, since it is numerically the simplest, where n is estimated as that value where the mode of the distribution of ℓ_{max} is equal to the observed largest value.

TABLE 5.1.1

n	$\ell^*(n)$	$\mu_\gamma(n)$	$\ell_L(n)$	$\sigma_\gamma(n)$	COV %
2	1.000	.667	.813	.256	38.4
3	.553	.543	.632	.200	36.8
4	.433	.462	.523	.161	34.8
5	.370	.412	.448	.154	37.4
6	.327	.371	.395	.135	36.4
7	.296	.338	.355	.122	36.1
8	.271	.319	.323	.110	34.5
10	.235	.271	.276	.093	34.3
12	.209	.241	.242	.080	33.2
15	.180	.208	.208	.068	32.7
20	.148	.171	.167	.058	33.9
30	.112	.127	.123	.037	29.1
40	.091	.103	.099	.028	27.7
50	.077	.087	.083	.023	26.6
60	.067	.076	.072	.020	25.8
70	.060	.068	.064	.017	25.1
80	.054	.061	.058	.015	24.5
90	.049	.055	.053	.013	24.0
100	.046	.051	.048	.012	23.5

TABLE A5.1.2

Observed Largest	Most Probable		Average		Max. Likelihood	
ℓ	n	$\overline{\ell}$	n	$\overline{\ell}$	n	$\overline{\ell}$
.02	280	.0036	~300	.0033	293	.0034
.04	118	.0085	135	.0074	126	.0079
.06	69.9	.014	81	.012	76	.013
.08	47.5	.021	56	.018	53	.019
.1	35.0	.029	42	.024	39	.025
.2	12.8	.078	15.9	.063	15.6	.064
.3	6.90	.146	8.5	.117	8.9	.112
.4	4.50	.224	5.3	.190	5.9	.169
.5	3.40	.299	3.5	.285	4.3	.234
.6	2.80	.361	2.54	.394	3.3	.308
.7	2.44	.409			2.6	.390
.8	2.24	.446			2.06	.486
.9	2.10	.475			1.66	.603

Appendix 5.2

Covariance of the Patches' Lengths

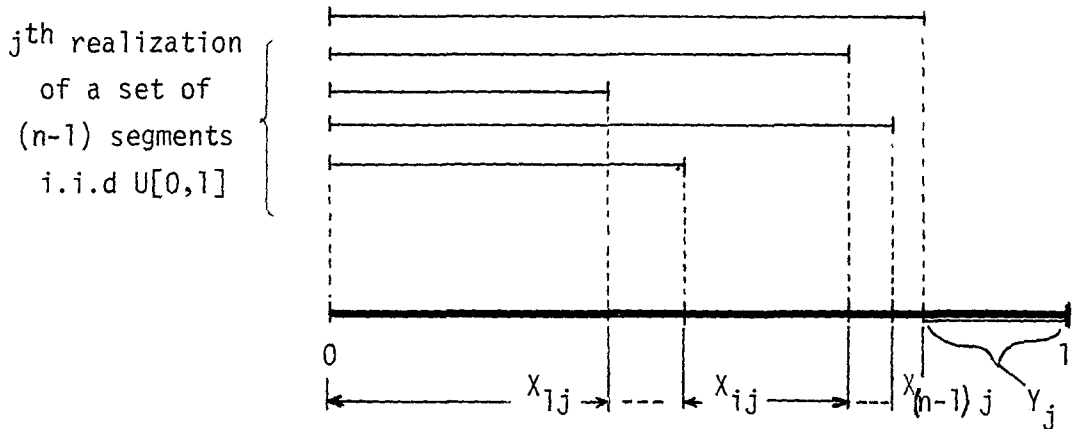

Consider a segment of unit length divided in n segments obtained by ranking n-1 independent segments of uniform distribution on [0, 1]. Consider two random variables, X_i and Y, such that

$$X = \sum_{i=1}^{n-1} X_i \text{ , where } X_i \text{ is the } i^{th} \text{ segment}$$

$$Y = n^{th} \text{ segment}$$

thus: $X + Y = 1$

If we fix Y=y, the distribution of the Z_i's becomes the distribution of n-1 segments on a (1-y) length segment:

$$\left.\begin{aligned} f_{X_i|Y}(x|y) &= \frac{(n-2)}{(1-y)}\left(1-\frac{x}{1-y}\right)^{n-3} \\ \text{and} \qquad f_Y(y) &= (n-1)(1-y)^{n-2} \end{aligned}\right\} \qquad \text{(A5.2.1)}$$

The joint distribution of X_i and Y becomes:

$$\left.\begin{aligned} f_{X_i,Y}(x, y) &= f_{X_i|Y}(x|y) \cdot f_Y(y) \\ &= (n-1)(n-2)(1-y-x)^{n-3} \end{aligned}\right\} \qquad \text{(A5.2.2)}$$

$$\text{for} \begin{cases} y \leq 1 \\ x \leq 1-y \\ 0 \leq 1-y-x \leq 1 \end{cases}$$

The expected value of X_iY is computed as:

$$E[X_iY] = \int_0^1 \int_0^{1-y} x\,y\,f_{X,Y}(x, y)dxdy$$

$$= \int_0^1 \int_0^{1-y} (n-1)(n-2)xy(1-y-x)^{n-3}\,dxdy$$

$$= (n-1)(n-2) \int_0^1 ydy \int_0^{1-y} x[(1-y)-x]^{n-3}\,dx = (n-1)(n-2) \int_0^1 ydy\, I(y)$$

where:

$$I(y) = \int_0^{1-y} [(1-y)-u]u^{n-3}\,du = (1-y) \int_0^{1-y} u^{n-3}\,du - \int_0^{1-y} u^{n-2}\,du$$

$$= \frac{(1-y)^{n-1}}{(n-1)(n-2)}$$

then:

$$E[X_iY] = \int_0^1 y(1-y)^{n-1}\,dy = \frac{1}{n(n+1)}$$

The covariance between X_i and Y is given by:

$$COV[X_iY] = E[X_iY] - E[X_i] \cdot E[Y]$$

Since the X_i's and Y have the same density function and their mean is $E[X_i] = E[Y] = \frac{1}{n}$; the covariance of X_iY is obtained as:

$$COV[X_iY] = \frac{1}{n(n+1)} - \frac{1}{n} \cdot \frac{1}{n}$$

$$= \frac{-1}{n^2(n+1)}$$

By reason of symmetry this is also true for any two segments X_i and X_j, where i = 1 to n, including Y.

$$COV[X_iX_j] = \frac{-1}{n^2(n+1)} \quad \text{for } i \neq j \qquad \text{(A5.2.3)}$$

The correlation between any two segments is then:

$$\rho(X_iX_j) = \frac{COV[X_iX_j]}{\sigma_\ell^2} = -\frac{1}{n-1}$$

For a segment of total length L we have:

$$COV(X_iX_j) = \frac{-L^2}{n^2(n+1)} \qquad i \neq j \qquad \text{(A5.2.4)}$$

REFERENCES

Aki, K., "Scaling Law of Seismic Spectrum," Journal of Geophysical Research, Vol. 72, No. 4, pp. 1217-1231, February 1967.

Aki, K., "Seismic Displacement Near a Fault," Journal of Geophysical Research, Vol. 73, No. 16, pp. 5359-5376, August 1968.

Aki, K., "Scaling of Earthquake Source Time Function," Geophysical J.R. Astr. Soc., 31, pp. 3-25, 1972.

Aki, K., "Characterization of Barriers on an Earthquake Fault," Journal of Geophysical Research, Vol. 84, No. B11, pp. 6140-6148, October 10, 1979.

Aki, K., Bouchon, M., Chouet, B. and Das, Shamita, "Quantitative Prediction of Strong Motion for a Potential Earthquake Fault," to be published in Analidi Geofisica.

Aki, K. and Richards, P.G., "Quantitative Seismology: Theory and Methods," Volumes I and II, Freeman and Company, 1980.

Anderson, J.G., "Motions Near a Shallow Rupturing Fault: Evaluation of Effects due to the Free Surface," Geophys. J.R. Astr. Soc., 46, pp. 575-593, 1976.

Andrews, D.J., "A Stochastic Fault Model 1. Static Case," Journal of Geophysical Research, Vol. 85, No. B7, pp. 3867-3877, July 10, 1980.

Aptikayev, F.F., "The Bearing of the Duration of Seismic Oscillations on Instrumental Evaluation of Seismic Intensity," in The Seismic Scale and Seismic Intensity Measurement Methods, Moscow, pp. 234-239, 1975 (in Russian).

Askins, R. and Cornell, C.A., "SHA-Based Attenuation Model Parameter Estimation," Proceedings of the U.S. National Earthquake Engineering Conference, Stanford, California, August 1979.

Bendat, J.S. and Piersol, A.G., "Random Data: Analysis and Measurement Procedures," Wiley Interscience, 1971.

Boatwright, J. and Boore, D., "A Simplification in the Calculation of Motions near a Propagating Dislocation," Bulletin of the Seismological Society of America, Vol. 65, No. 1, pp. 133-138, February 1975.

Bolt, B.A., "Duration of Strong Ground Motion," Proceedings 5th World Conference on Earthquake Engineering, Rome, pp. 1304-1313, 1973.

Bonilla, M.G., "Historic Surface Faulting--Map Patterns, Relation to Subsurface Faulting, and Relation to Pre-existing Faults," USGS Open File Report 79-1239, pp. 36-65, 1979.

Boore, D.M. and Joyner, W.B., "The Influence of Rupture Inchoherence on Seismic Directivity," Bulletin of the Seismological Society of America, Vol. 68, No. 2, pp. 283-300, April 1978.

Bouchon, M. and Aki, K., "Discrete Wave-Number Representation of a Seismic-Source Wave Field," Bulletin of the Seismological Society of America, Vol. 67, No. 2, pp. 259-277, April 1977.

Brune, J.N., "Tectonic Stress and the Spectra of Seismic Shear Waves from Earthquakes," Journal of the Geophysical Research, Vol. 75, No. 26, pp. 4997-5009, September 10, 1970.

Das, S. and Aki, K., "Fault Planes with Barriers: A Versatile Earthquake Model," Journal of the Geophysical Research, Vol. 82, pp. 5648-5670, 1977.

Eaton, J.P., O'Neill, M.E., and Murdock, J.N., "Aftershocks of the 1966 Parkfield-Cholame, California Earthquake: A Detailed Study," Bulletin of the Seismological Society of America, Vol. 60, pp. 1151-1197, 1970.

Esteva, L. and Rosenblueth, E., "Espectros de Tremblores a Distancias Moderadas y Grandes," Socieidad Mexicana de Engenieria Sismica Boletin, Vol. 2, No. 1, pp. 1-18, 1964.

Geller, R.J., "Scaling Relations for Earthquake Source Parameters and Magnitudes," Bulletin of the Seismological Society of America, Vol. 66, No. 5, pp. 1501-1523, October 1976.

Haskell, N.A., "Total Energy and Energy Spectral Density of Elastic Wave Radiation from Propagating Faults, (Part I)," Bulletin of the Seismological Society of America, Vol. 34, No. 6, pp. 1811-1841, December 1964.

Haskell, N.A., "Total Energy and Energy Spectral Density of Elastic Wave Radiation from Propagating Faults, (Part II)," Bulletin of the Seismological Society of America, Vol. 56, No. 1, pp. 125-140, February 1966.

Hays, W.W., "A Note on the Duration of Earthquake and Nuclear-Explosion Ground Motion," Bulletin of the Seismological Society of America, Vol. 65, No. 4, pp. 875-883, 1975.

Heaton, T.H., "Generalized Ray Models of Strong Ground Motion," Ph.D. Thesis, California Institute of Technology, Pasadena, California, September 1978.

Housner, G.W., "Intensity of Earthquake Ground Shaking Near the Causative Fault," Proceedings of the 3rd World Conference on Earthquake Engineering, Auckland, Vol. 1, pp. III-94 to III-109, 1965.

Husid, R., "Gravity Effects on the Earthquake Response of Yielding Structures," Report of Earthquake Engineering, Research Laboratory, California Institute of Technology, Padadena, California, 1967.

Kameda, H. and Ang, H.S., "Simulation of Strong Earthquake Motions for Inelastic Structural Response," Proceedings of the 6th World Conference on Earthquake Engineering, New Delhi, pp. II-149 to II-154, 1977.

Kanamori, H. and Anderson, D.L., "Theoretical Basis of Some Empirical Relations in Seismology," Bulletin of the Seismological Society of America, Vol. 65, No. 5, pp. 1073-1095, October 1975.

Keilis-Borok, V., "An Estimation of the Displacement in an Earthquake Source and of Source Dimensions," Ann. Geofis, Rome, 12, pp. 205-214, 1959.

Kendall, M.G. and Moran, P.A.P., "Geometrical Probability," Griffin's Statistical Monograph and Courses, Number 10, 1970.

Kjartansson, E., "Constant Q-Wave Propagation and Attenuation," Journal of Geophysical Research, Vol. 84, No. B9, pp. 4737-4748 August 10, 1979.

Love, A.E.H., "A Treatise on the Mathematical Theory of Elasticity," 4th Edition, Dover Publications, 1944.

Maruyama, T., "On the Force Equivalents of Dynamical Elastic Dislocations with Reference to the Earthquake Mechanism," Bulletin of the Earthquake Research Institute, Tokyo, Vol. 41, pp. 467-486, 1969.

Mikumo, T., "Long Period P-Wave Forms and the Source Mechanism of Intermediate Earthquakes," Journal of Phys. of the Earth, Vol. 17, No. 2, pp. 169-192, 1969.

McCann, M.S. and Shah, H.C., "Determining Strong Motion Duration of Earthquakes," Bulletin of the Seismological Society of America, Vol. 69, No. 4, pp. 1253-1265, 1979.

McGarr, A. and Pollard, D., Gay, N.C., Ortlepp, W.D., "Observations and Analyses of Structures in Exhumed Mine-Induced Faults," USGS Open-File Report 79-1239, 1979.

Nakano, H., "Notes on the Nature of the Forces which give Way to the Earthquake Motions," Seismol. Bull. Centr. Met. Obs., Japan, 1, pp. 92-120, 1923.

Papageorgiou, A., Ongoing research on source parameters estimation. Personal Communication. 1980.

Perez, V., "Time Dependent Spectral Analysis of Thirty-One Strong Motion Earthquake Records," U.S. Geological Survey, Open-File Report, 33p., November 1974.

Savy, J., "Determination of Seismic Risk Parameters: A Stochastic Approach," The John A. Blume Research Institute, Stanford, Report No. 34, 1978.

Shakal, A.F., "Analysis and Modelling of the Effects of the Source and Medium on Strong Motion," Ph.D. Thesis, MIT, October 1979.

Sieh, K.E., "A Study of Holocene Displacement History Along the South-Central Reach of the San Andreas Fault," Ph.D. Dissertation, Stanford University, Stanford, California, 1977.

Sieh, K.E., "Slip Along the San Andreas Fault Associated with the Great 1857 Earthquake," BSSA, Vol. 68, No. 5, pp. 1421-1448, 1978.

Tchalenko, J.S. and Berberian, M., "Dasht-e-Bayāz Fault, Iran: Earthquake and Earlier Related Structures in Bedrock," Bulletin of the Geological Society of America, Vol. 86, pp. 703-709, 1975.

Trifunac, M.D. and Brady, A.G., "A Study on the Duration of Strong Ground Motion," Bulletin of the Seismological Society of America, Vol. 65, No. 3, pp. 581-626, June 1975.

Trifunac, M.D. and Westermo, B., "A Note on the Correlation of Frequency-Dependent Duration of Strong Earthquake Ground Motion with the Modified Mercalli Intensity and the Geologic Conditions at the Recording Stations," Bulletin of the Seismological Society of America, Vol. 67, No. 3, pp. 917-927, 1977.

Vanmarcke, E.H. and Lai, S.P., "Strong Motion Duration of Earthquakes," MIT Department of Civil Engineering, Report R77-16, 32 pages, 1977.

Wallace, R.E., "Notes on Stream Channels Offset by the San Andreas Fault, Southern Coast Ranges, California," Proceedings of the Conference on Geologic Problems of the San Andreas Fault System, Stanford University, Publ. Univ. Ser. Geol. Sci., 11, pp. 6-21, 1968.

Wallace, R.E., "Surface Fracture Patterns Along the San Andreas Fault," Proceedings of the Conference on Tectonic Problems of the S.A. Fault System, Stanford University, Publ. Geol. Sci., ed. Kovach, R.L. and Nur, A., Vol. XIII, pp. 248-250, 1973.